Oxygen Variability and Eddy-driven Meridional Oxygen Supply in the Tropical North East Atlantic Oxygen Minimum Zone

A diagnosing Study based on
Shipboard and Moored Observations

Dissertation
ZUR ERLANGUNG DES DOKTORGRADES
DER MATHEMATISCH - NATURWISSENSCHAFTLICHEN FAKULTÄT
DER CHRISTIAN-ALBRECHTS-UNIVERSITÄT ZU KIEL

VORGELEGT VON
JOHANNES HAHN
KIEL, 2013

GEOMAR
Helmholtz-Zentrum für Ozeanforschung Kiel

Referent:	Prof. Dr. Peter Brandt
Korreferent:	Prof. Dr. Richard J. Greatbatch
Tag der mündlichen Prüfung:	29.05.2013
Zum Druck genehmigt:	29.05.2013

gez. _____

Prof. Dr. Wolfgang J. Duschl, Dekan

Abstract

The distribution of the mean oceanic oxygen concentration results from a balance between ventilation and consumption and, in particular, reveals extended oxygen minimum zones (OMZ) in the eastern tropical Pacific and Atlantic at intermediate depth ($300\,\mathrm{m}$ - $700\,\mathrm{m}$). It has been recently shown that OMZs expand in size and are subject to a significant oxygen decrease, where the OMZ in the Tropical North East Atlantic (TNEA) holds the most significant and largest oxygen trend.

This study analyzes hydrographic and velocity data from shipboard and moored observations which were acquired along the 23°W section cutting meridionally through the TNEA OMZ, in order to (i) quantify regional differences in the oxygen variability, (ii) identify the role of two mixing processes (mesoscale stirring and diapycnal mixing) in the production of oxygen variance based on the extended Osborn-Cox model and (iii) estimate the role of mesoscale eddies in the meridional ventilation of the TNEA OMZ.

Enhanced oxygen variability is found at the boundaries of the OMZ which is predominantly generated by mesoscale stirring along isopycnals and diapycnal mixing across isopycnals. South of the OMZ core (which is located at about 11°N), mesoscale stirring dominates the generation of oxygen variance, whereas above the OMZ core within the deep oxycline (located at about $300\,\mathrm{m}$ depth) both processes, mesoscale stirring and diapycnal mixing, are found to be of similar importance.

Meridional eddy fluxes of oxygen are estimated by using (i) a diffusive flux parameterization based on a lateral eddy diffusion coefficient and the mean isopycnal oxygen gradient, and (ii) a correlation method based on velocity and oxygen time series from moored observations. At the mooring positions 5°N, 23°W and 8°N, 23°W, the results of both methods are in good agreement in the depth range of the OMZ core, yielding a northward oxygen flux from the well-ventilated equatorial region toward the OMZ core.

The divergence of the meridional oxygen flux, as obtained from the diffusive flux parameterization, yields an eddy-driven meridional oxygen supply from the south into the OMZ of about $2.4\,\mu\mathrm{mol\,kg^{-1}\,yr^{-1}}$ at its core depth. Above the OMZ core, mesoscale eddies act to redistribute low-oxygen and high-oxygen waters associated with latitudinally alternating westward and eastward currents. Locally, absolute values of the eddy-driven meridional oxygen supply are greater than $10\,\mu\mathrm{mol\,kg^{-1}\,yr^{-1}}$ which is likely balanced by mean zonal advection.

Combining the above results with recent studies about oxygen consumption, diapycnal oxygen supply and oxygen tendency, a refined oxygen budget for the TNEA OMZ is derived. The eddy-driven meridional oxygen supply accounts for more than 50% of the supply required to balance the estimated oxygen consumption. The oxygen tendency in the TNEA OMZ, as given by the multidecadal oxygen decline, is at maximum slightly above the OMZ core and represents a substantial imbalance of the oxygen budget reaching up to 20% of the magnitude of the eddy-driven oxygen supply.

Oxygen data from moored observations was acquired with optode oxygen sensors. To achieve a high quality of these measurements, an in situ calibration procedure is proposed which yields an average measurement error of $4.6\,\mu\mathrm{mol\,kg^{-1}}$ with 95% confidence (evaluated for water masses in the upper $1000\,\mathrm{m}$ of the Tropical Atlantic in combination with onboard lab calibrations against zero oxygen). On the one hand, this calibration procedure yields calibration errors that are worse by roughly a factor of 2 in comparison to sophisticated laboratory calibrations, but on the other hand this simple method is not affected by severe sensor drifts that are frequently observed at some time before or after the field deployment. In case of profiling systems (shown here for a CTD/O_2 cast), a time constant correction improves the quality of the measured oxygen profile which is of particular interest for the application in gliders or floats.

Zusammenfassung

Die charakteristische Sauerstoffverteilung im Ozean resultiert aus einem Gleichgewicht zwischen Ventilation und Sauerstoffzehrung, was die Ausbildung von Sauerstoffminimumzonen (SMZ) auf intermediärer Tiefe ($300\,\mathrm{m}$ - $700\,\mathrm{m}$) im Tropischen Ost-Pazifik und Tropischen Ost-Atlantik zur Folge hat. Neue Studien belegen, dass sich SMZs sowohl in ihrer Größe ausdehnen als auch einer signifikanten Verringerung ihrer Sauerstoffkonzentration unterworfen sind, wobei die Sauerstoffminimumzone im Tropischen Nord-Ost Atlantik (TNOA) hierbei den stärksten Trend aufweist.

In dieser Arbeit werden hydrographische Daten sowie Geschwindigkeitsmessungen aus Schiffs- und Verankerungsbeobachtungen analysiert, die entlang des 23°W Schnittes durch die SMZ des TNOA aufgezeichnet wurden. Ziel der Arbeit ist (i) die Quantifizierung regionaler Unterschiede der Sauerstoffvariabilität, (ii) die Identifikation von zwei Vermischungsprozessen (mesoskalige Verwirbelung und diapyknische Vermischung) in deren Einfluss auf die Erzeugung von Sauerstoffvarianz mit Hilfe des erweiterten Osborn-Cox-Modells und (iii) die Abschätzung des Beitrags mesoskaliger Wirbel zur meridionalen Ventilation der SMZ im TNOA.

Es zeigt sich eine erhöhte Sauerstoffvariabilität an den Rändern der SMZ, welche in erster Linie durch mesoskalige Verwirbelung des mittleren Sauerstoffgradienten entlang von Isopyknen sowie durch diapyknische Vermischung des mittleren Sauerstoffgradienten über Isopyknen hinweg erzeugt wird. Südlich des Kerns der SMZ (welcher bei 11°N gelegen ist) wird der Hauptteil der Sauerstoffvarianz durch mesoskalige Verwirbelung erzeugt, wohingegen am oberen Rand der SMZ (welcher durch die tiefe Oxykline auf etwa $300\,\mathrm{m}$ gegeben ist) beide Prozesse eine adäquate Bedeutung in der Erzeugung von Sauerstoffvarianz aufweisen.

Die Abschätzung des wirbelgetriebenen meridionalen Sauerstoffflusses erfolgt durch

(i) eine Diffusions-Parametrisierung, die über einen lateralen Austauschkoeffizienten und den mittleren isopyknischen Sauerstoffgradienten definiert ist und (ii) Korrelation von Geschwindigkeits- und Sauerstoffzeitserien aus Verankerungsbeobachtungen. Der Vergleich beider Methoden an den Verankerungspositionen 5°N, 23°W und 8°N, 23°W zeigt eine gute Übereinstimmung der berechneten Sauerstoffflüsse auf Tiefe des SMZ-Kerns. Hierbei wird ein nordwärts gerichteter Sauerstofffluss vom gut ventilierten äquatorialen Regime hin zum Kern der SMZ beobachtet. Aus der Divergenz des meridionalen Sauerstoffflusses, die sich mittels Diffusions-Parametrisierung bestimmen lässt, ergibt sich die meridionale Sauerstoffversorgung der SMZ durch mesoskalige Wirbel (auf der Tiefe des SMZ-Kerns) zu etwa $2.4\,\mu\mathrm{mol\,kg^{-1}\,yr^{-1}}$. Oberhalb des SMZ-Kerns führen mesoskalige Wirbel zu einer Umverteilung von sauerstoffarmem und sauerstoffreichem Wasser, welches von westwärtigen bzw. ostwärtigen Strömen transportiert wird. Dies führt lokal zu wirbelgetriebenen meridionalen Sauerstoffflüssen mit einem Absolutbetrag von etwa $10\,\mu\mathrm{mol\,kg^{-1}\,yr^{-1}}$, welche sehr wahrscheinlich durch die Zonalströmungen bilanziert werden.

Auf Basis obiger Resultate und in Kombination mit den Ergebnissen anderer kürzlich veröffentlichter Studien über Sauerstoffzehrung, diapyknische Sauerstoffversorung bzw. den langjährigen Sauerstofftrend wird ein detaillierteres Sauerstoffbudget für die SMZ des TNOA abgeleitet. Es zeigt sich, dass mesoskalige Wirbel zu einer Sauerstoffversorgung der SMZ führen, die über 50% der Sauerstoffzehrung bilanziert. Prinzipiell bedeutet der substantielle Sauerstofftrend der SMZ ein unausgeglichenes Sauerstoffbudget, was betragsmäßig bis zu 20% der wirbelgetriebenen meridionalen Sauerstoffversorgung entspricht.

Sauerstoffmessungen aus Verankerungsbeobachtungen wurden mittels Optoden aufgezeichnet. Um eine gute Genauigkeit der Messungen zu gewährleisten, wird eine Methode zur in situ Kalibration vorgeschlagen, womit sich ein mittlerer Kalibrationsfehler von $4.6\,\mu\mathrm{mol\,kg^{-1}}$ (95% Konfidenz) ergibt (basierend auf Kalibrierungen in Wasser aus den oberen $1000\,\mathrm{m}$ des Tropischen Atlantiks in Kombination mit Labor-Kalibrierungen an Bord gegen Wasser mit 0% Sauerstoffsättigung). Einerseits zeigt die Methode einen etwa Faktor 2 größeren Fehler im Vergleich zu einer vollständigen Laborkalibration. Der entscheidende Vorteil ist jedoch deren simple Anwendung sowie die Vermeidung des Einflusses einer starken Sensordrift auf die Kalibration. Im Fall von profilierenden Systemen (hier am Beispiel eines CTD/O_2 -Profils gezeigt) verbessert eine Zeitkonstantenkorrektur die Qualität des gemessenen Sauerstoffprofils, was insbesondere für die Anwendung in Glidern oder Floats von Interesse ist.

Contents

The following manuscript has been submitted as part of this monograph:

[1] **J. Hahn**, P. Brandt, R. J. Greatbatch, G. Krahmann and A. Körtzinger: Oxygen Variance and Meridional Oxygen Supply in the Tropical North East Atlantic Oxygen Minimum Zone. *submitted to Climate Dynamics*.

J. Hahn conducted the data processing and analysis, developed and applied the methodology, and wrote the manuscript. The co-authors contributed to the scientific content of the manuscript with designing the experiments at sea, data calibration, discussions of the results, and comments on the manuscript.

J. Hahn contributed as a co-author to the following publications:

[2] P. Brandt, R. J. Greatbatch, M. Claus, S.-H. Didwischus, V. Hormann, A. Funk, **J. Hahn**, G. Krahmann, J. Fischer and A. Körtzinger: Ventilation of the equatorial Atlantic by the equatorial deep jets. *Journal of Geophysical Research - Oceans*, **117** (2012).

J. Hahn contributed with data processing (calibration of optodes), discussions of the results and comments on the manuscript.

[3] J. Karstensen, B. Fiedler, P. Brandt, R. Zantopp, **J. Hahn**, F. Schütte, A. Körtzinger, G. Fischer, M. Visbeck, O. Melicio and D. R. Wallace: Dead-zone eddies in the tropical eastern North Atlantic Ocean. *under revision in Nature*.

J. Hahn contributed with data processing (calibration of optodes), discussions of the results and comments on the manuscript.

CHAPTER 1

Introduction

1.1 Oxygen minimum zones in the tropical oceans

The first *Meteor* expedition into the Atlantic Ocean was carried out between 1925 - 1927 with the main goal of investigating the large scale circulation of the Atlantic[1]. During the three years of expedition, oceanographic, chemical and biological parameters were surveyed and are summarized in *'Wissenschaftliche Ergebnisse der Deutschen Atlantischen Expedition auf dem Forschungs- und Vermessungsschiff "Meteor" 1925-1927'* [*Defant*, 1939]. One key parameter for the characterization of the large scale ocean circulation was considered to be the oceanic oxygen distribution, since it sheds light on well-ventilated and weakly ventilated regimes of the ocean. A detailed description and discussion of the oxygen distribution in the Atlantic Ocean obtained from this expedition is given in *Wattenberg* [1939]. The analysis showed that a distinct oxygen minimum exists at intermediate depth predominantly extending in the Tropical East Atlantic north and south of the equator. As an example, the oxygen distribution at a depth of $600\,\mathrm{m}$, as obtained from *Wattenberg* [1939][2], is shown in Figure 1.1a.

It is remarkable that simply based on hydrographic parameters (temperature, salinity and oxygen) obtained during the first *Meteor* expedition, *Wüst* [1936] derived a generally still accurate picture of the large scale circulation. On the one hand, he described the well-ventilated western boundary and on the other hand, he found weakly ventilated regimes in the eastern Atlantic. He already concluded that the latter regimes are supplied from

[1] A brief overview is given e.g. in the book from *Jakobi et al.* [2011].

[2] The common unit for the oxygen concentration used at that time was $\mathrm{cm^3\,l^{-1}}$ ($=\mathrm{ml\,l^{-1}}$). Nowadays, it is expressed in $\mu\mathrm{mol\,l^{-1}}$ ($1\,\mathrm{ml\,l^{-1}} \mathrel{\widehat{=}} 44.615\,\mu\mathrm{mol\,l^{-1}}$, or referring to the in situ density: $\mu\mathrm{mol\,kg^{-1}}$) using the standard molar volume for ideal gases [*Grasshoff et al.*, 1999].

(a)

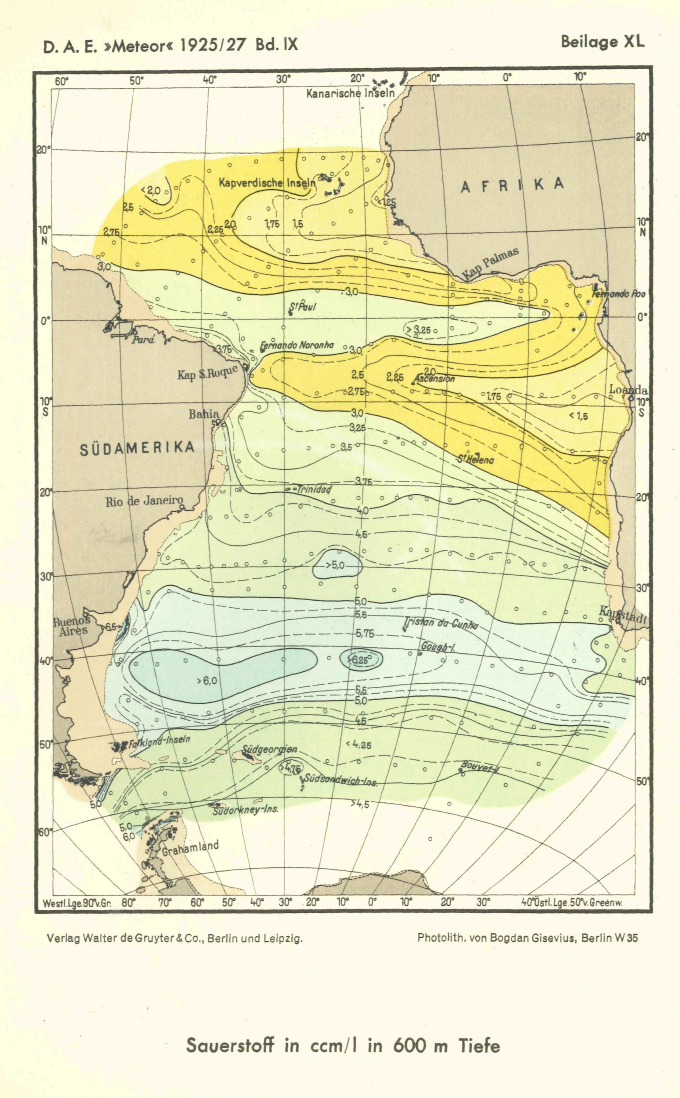

(b)

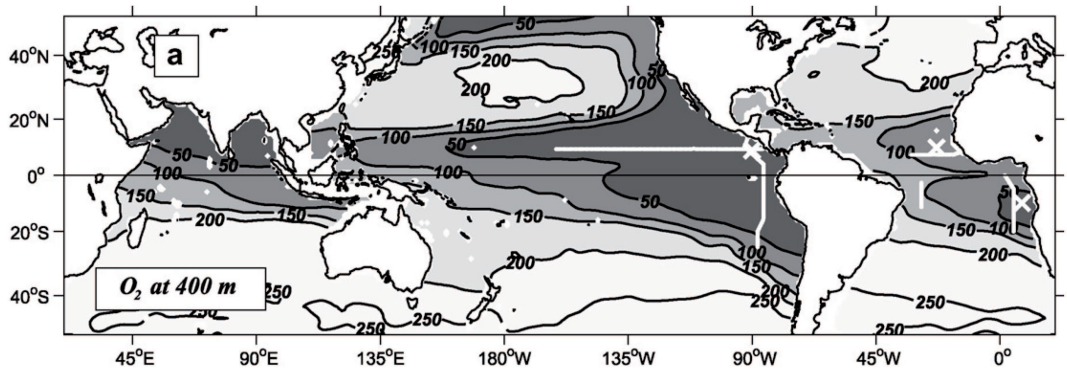

Figure 1.1. (a) Oxygen distribution (in units of $\mathrm{cm}^3\,\mathrm{l}^{-1}$) in the Atlantic Ocean at $600\,\mathrm{m}$ depth obtained during the first *Meteor* 1925 - 1927 (after *Wattenberg* [1939]). (b) Global distribution of the annual mean dissolved oxygen (in units of $\mu\mathrm{mol}\,\mathrm{kg}^{-1}$) between 50°S and 50°N at $400\,\mathrm{m}$ depth (after *Karstensen et al.* [2008]). Note that the oxygen concentration in (a) and (b) is given in different units and at slightly different depths.

the west by zonal pathways, but additionally suggested lateral and vertical turbulent processes as possible mechanisms for their ventilation. Within the framework of theoretical investigations [*Sverdrup*, 1938] as well as on the basis of observed chemical and biological properties [*Wattenberg*, 1939], a qualitative analysis was carried out in order to understand and describe the existence of the oxygen minimum in the Atlantic Ocean at intermediate depth. However, a complex interplay was suspected between physical ventilation and biogeochemical consumption forming the oceanic oxygen distribution. Hence, oceanographers, marine biologists and chemists were far beyond a quantitative analysis of these processes at that time.

Over the past century, physical oceanographers have used great efforts to provide a hydrographic data set of the ocean with a high spatial coverage which culminated in the World Ocean Circulation Experiment (WOCE, 1990-1998), [*Gouretski and Koltermann*, 2004]. Based on this data set, a global distribution of the oceanic dissolved oxygen was obtained, revealing that oxygen minimum zones (OMZ) extend at intermediate depth in all three ocean basins (e.g. *Karstensen et al.* [2008]). Figure 1.1b shows the global oxygen distribution between 50°S and 50°N at a depth of $400\,\mathrm{m}$ (after *Karstensen et al.* [2008]) which is considered the average core depth of the OMZs. The figure shows that OMZs are located at the eastern boundaries of the tropical oceans, such as in the Tropical North and South East Atlantic, Tropical North and South East Pacific as well as in the Northern Indian Ocean. The OMZs in the Tropical North and South East Pacific are suboxic regimes ($< 4.5\,\mu\mathrm{mol\,kg^{-1}}$) holding oxygen concentrations of below $1\,\mu\mathrm{mol\,kg^{-1}}$, whereas the Tropical North and South East Atlantic are hypoxic[3] regimes (below $\sim 80\,\mu\mathrm{mol\,kg^{-1}}$), where oxygen concentrations of below $40\,\mu\mathrm{mol\,kg^{-1}}$ [*Stramma et al.*, 2009] and at about $17\,\mu\mathrm{mol\,kg^{-1}}$ [*Karstensen et al.*, 2008] are observed, respectively. On the basis of observational and model data, *Karstensen et al.* [2008] could refine the historical approaches and describe the low oxygen concentration in the OMZs as a combination of weak mean ventilation and enhanced biogeochemical oxygen consumption.

Recent studies pointed out that the OMZs of the tropical oceans change in size and oxygen inventory. *Stramma et al.* [2008b] report an expansion of all OMZs, of which those in the Tropical North and South Atlantic show the strongest and most significant oxygen decrease, with $0.34 \pm 0.13\,\mu\mathrm{mol\,kg^{-1}\,yr^{-1}}$ and $0.17 \pm 0.11\,\mu\mathrm{mol\,kg^{-1}\,yr^{-1}}$, respectively, over the last decades. Although a model study by *Keeling et al.* [2010] predicts a decline in the global ocean oxygen inventory of 1% - 7% due to anthropogenic forcing which goes along with an expansion of the OMZs, other studies show that ocean circulation models are generally not yet capable of reproducing the mean shape [*Meissner et al.*, 2005; *Oschlies et al.*, 2008] and the observed trends [*Stramma et al.*, 2012] of the OMZs. A general misrepresentation of the mean and variable current system at intermediate depth in ocean

[3]The hypoxic threshold is defined as the critical oxygen concentration of which macroorganisms are stressed or even die. A uniform threshold cannot be quantified, since it strongly depends on the considered species [*Stramma et al.*, 2008b].

circulation models is an obvious reason for the failure of those models to correctly represent the observed mean oxygen distribution [*Ascani et al.*, 2010; *Brandt et al.*, 2012]. In order to explain long-term changes in the oxygen distribution of OMZs, different mechanisms were suggested involving changes in the ventilation and consumption [*Bopp et al.*, 2002; *Brandt et al.*, 2010; *Matear and Hirst*, 2003; *Oschlies et al.*, 2008].

Even though the OMZ in the Tropical North East Atlantic (TNEA) holds comparatively high oxygen concentrations, it is subject to the strongest oxygen decrease of all OMZs. It is of major interest to diagnose possible changes in the ventilation and biogeochemical processes which contribute to oxygen supply or oxygen consumption and eventually result in the observed oxygen trend. In this context, the question arises whether the oxygen in the TNEA OMZ will further decrease and whether this OMZ might turn into a suboxic regime as it is already the case for the OMZs in the Tropical East Pacific.

In the following two sections, a general overview about the mean flow field, the mean oxygen distribution and the ventilation pathways in the Tropical Atlantic will be given.

1.2 Mean circulation in the Tropical Atlantic

In this section, the mean upper-layer circulation in the Tropical Atlantic is introduced and and will be used in the following section 1.3 to describe its impact on the mean oxygen distribution in the Tropical Atlantic and the existence of the TNEA OMZ.

The circulation system in the Tropical Atlantic is a very complex regime due to the superposition of different physical mechanisms as the wind-driven forcing, the Meridional Overturning Circulation (thermohaline forcing) and the Subtropical-Tropical Cells. The main currents of the Tropical and Subtropical Atlantic are shown in Figure 1.2a (after *Brandt et al.* [2010]). (i) In the Subtropical North Atlantic, the North Equatorial Current (NEC) represents the southern flank of the subtropical gyre circulation. (ii) The interior Tropical Atlantic is characterized by meridionally alternating zonal currents, of which the most important surface and thermocline currents are: the northern and central branch of the South Equatorial Current (nSEC, cSEC) at 2°N and 4°S, respectively, the North Equatorial Countercurrent (NECC) at 5°N and its northern branch (nNECC) at 9°N, the Equatorial Undercurrent (EUC) at the equator as well as the North and South Equatorial Undercurrent (NEUC, SEUC) at 5°N and 5°S, respectively. Below the thermocline, generally weaker currents are found that are part of the equatorial intermediate current system [*Ascani et al.*, 2010; *Brandt et al.*, 2012] including the Equatorial Intermediate Current (EIC) at the equator as well as the Northern and Southern Intermediate Countercurrent (NICC, SICC) at about 2°N and 2°S, respectively. A meridional section of the mean zonal velocity shown in Figure 1.2b representing the mean zonal currents between 6°S and 14°N along 23°W. (iii) At the western boundary of the Tropical Atlantic, the North Brazil Current

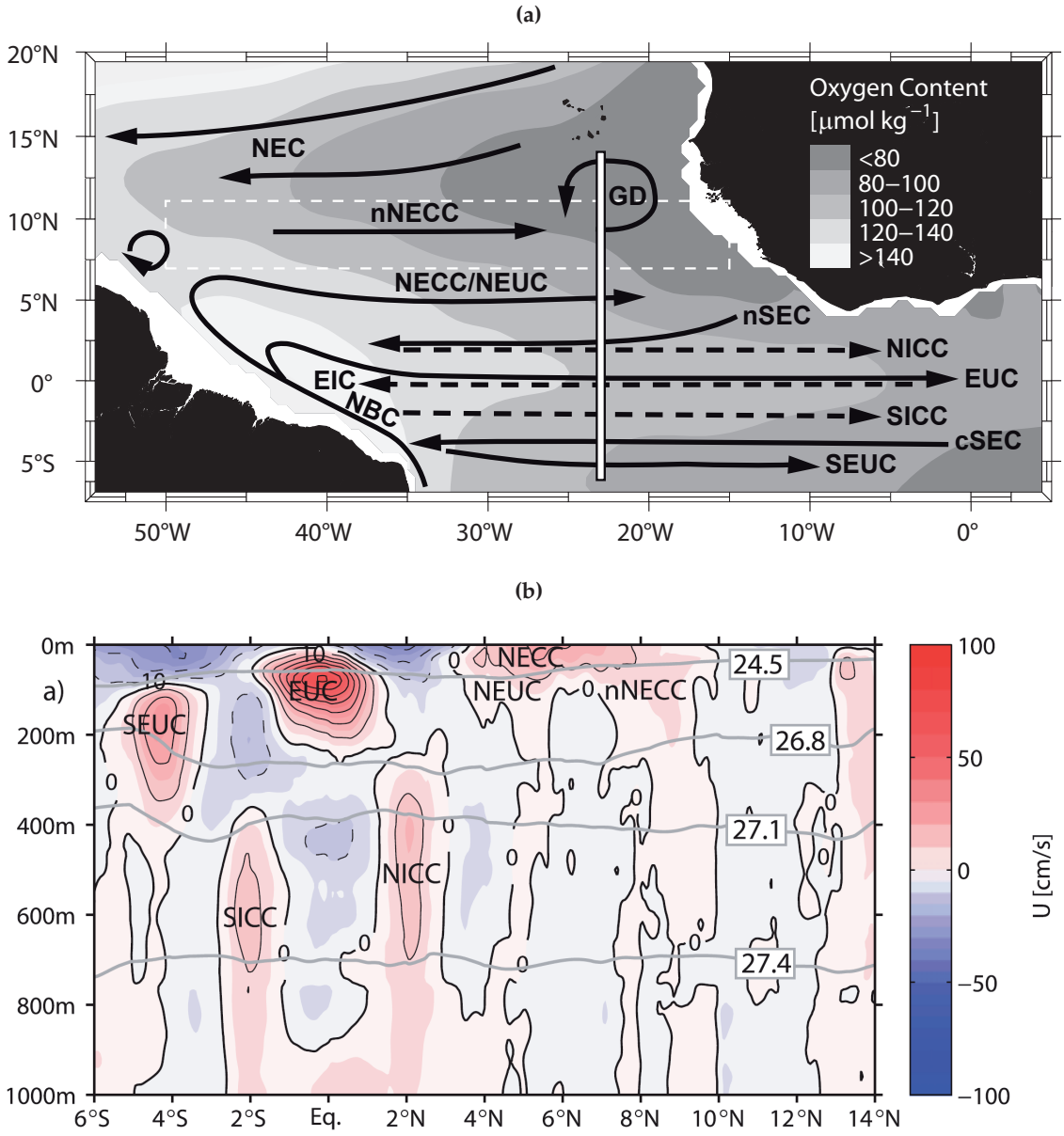

Figure 1.2. (a) Oxygen distribution (gray shading) in the Tropical Atlantic at 300 m - 500 m. Superimposed are the mean surface (solid lines) and subsurface (dashed lines) currents. White bar marks the 23°W section that is shown for the mean zonal velocity in (b). (b) Meridional section of the mean zonal velocity in the upper 1000 m between 6°S and 14°N along 23°W. ((a) and (b) from *Brandt et al.* [2010]).

(NBC) forms an alongshore current directed toward the Northwest. On the one hand, it is part of the Meridional Overturning Circulation [*Schott et al.*, 2003] directly supplying the Caribbean Sea along the western boundary pathway, and on the other hand it feeds the equatorial current system by retroflecting into the EUC, the NECC and nNECC [*Schott et al.*, 1998; *Stramma and Schott*, 1999].

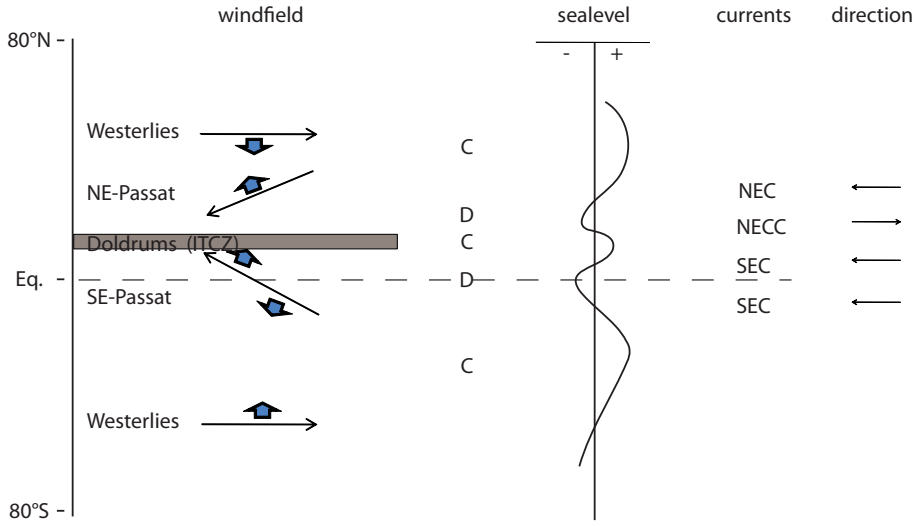

Figure 1.3. Schematic of the wind-driven surface circulation in the Tropical Atlantic. The left panel shows the large scale windfield indicated by the black arrows. The resulting Ekman transport is indicated by blue arrows. It induces convergences (C) and divergences (D) that lead to a displacement of the mean sealevel as shown in the middle panel. The resulting surface zonal currents that adjust to the sealevel are shown in the right panel (after *Hummels* [2012]).

Most of the surface currents are wind-driven features, such as the NEC, nNECC, NECC/NEUC, EUC and the SEUC (cf. Figure 1.3, after *Hummels* [2012]). The mean large scale windfield induces Ekman divergences and convergences in meridional direction which lead to a displacement of the sealevel. Geostrophically balanced zonal currents adjust to this displacement, resulting in the observed circulation pattern. Although wind-driven, these currents reach down to intermediate depths ($\sim 400\,\mathrm{m}$) as shown in Figure 1.2b. The wind-driven currents are generally subject to a seasonal variability due to the seasonal migration of the Intertropical Convergence Zone (ITCZ). So, in the central Tropical Atlantic the NECC/NEUC and the nNECC exhibit an annual cycle with a distinct maximum eastward velocity in boreal summer [*Garzoli and Katz*, 1983].

Luyten et al. [1983] described the pathway of the NEC with the ventilated thermocline theory. They could explain the shadow zone southeast of the subtropical gyre circulation which is not ventilated by the mean circulation at all. Direct (interior) pathways between the Subtropical North Atlantic and the equatorial Atlantic are strongly suppressed due to a potential vorticity barrier at the archipelago of the Cape Verde Islands at about 17°N [*Zhang et al.*, 2003; *Schott et al.*, 2004]. Consequently, the ventilation of the equatorial Atlantic from the North is rather weak and mainly occurs via the western boundary. Hence, central water masses in the equatorial Atlantic as well as in the shadow zone in the Tropical North East Atlantic consist to a large fraction of South Atlantic Water [*Kirchner et al.*, 2009].

1.3 Oxygen minimum zone in the Tropical North East Atlantic and its supplying pathways

It was already described by *Wyrtki* [1962] that the oceanic oxygen distribution is determined by the mean circulation. The comparison of the mean current field (as described in the previous section) and the mean horizontal oxygen distribution ($300\,\mathrm{m}$ - $500\,\mathrm{m}$) in Figure 1.2a reveal that the Tropical East Atlantic is a low oxygen regime, whereas the Tropical West Atlantic is well-ventilated by strong boundary currents. As a consequence of the weak mean circulation and the biogeochemical consumption, the TNEA OMZ is located in the weakly-ventilated shadow zone of the subtropical gyre circulation. It extends at intermediate depths from $300\,\mathrm{m}$ - $700\,\mathrm{m}$ with a core depth of about $450\,\mathrm{m}$ and a meridional core position at about 11°N, where oxygen concentrations below $40\,\mu\mathrm{mol\,kg^{-1}}$ are frequently observed [*Stramma et al.*, 2009].

In the north, the TNEA OMZ is bordered by the NEC, while in the south, a pronounced equatorial oxygen maximum limits the extension of the OMZ. This maximum is generated by the ventilation due to strong mean and variable zonal currents, where an eastward (westward) flow advects oxygen-rich (oxygen-poor) waters from (toward) the well-ventilated western boundary [*Brandt et al.*, 2008, 2012]. In particular, *Brandt et al.* [2012] conducted a quantitative analysis of the equatorial oxygen variability. They found that the oxygen concentration along the equator is subject to a strong interannual variability at intermediate depths ($300\,\mathrm{m}$) which is caused by deep equatorial zonal jets on an interannual time scale of $4.5\,\mathrm{yr}$. These deep jets lead to a net eastward flux of oxygen and thus to a ventilation of the equatorial East Atlantic.

North of the equatorial oxygen maximum in the latitude range of the OMZ, two eastward current bands contribute to the ventilation of the upper OMZ from the West [*Stramma et al.*, 2005]. At 4°N - 6°N, the NECC/NEUC band acts as a major source for oxygen-rich South Atlantic Central Water. The nNECC at 8°N - 10°N advects oxygen-rich South Atlantic Central Water including an admixture of North Atlantic Central Water [*Stramma et al.*, 2005; *Kirchner et al.*, 2009]. Below, in the depth range from $300\,\mathrm{m}$ to $600\,\mathrm{m}$, the oxygen supply due to mean eastward currents is still present but much weaker. By analyzing hydrographic and current data, *Brandt et al.* [2010] propose that a weakening of the deeper-reaching flow of the nNECC over the past decades forced a deoxygenation in the upper part of the OMZ. Although the existence of a seasonal cycle could not be proven, *Stramma et al.* [2008a] report a strong oxygen supply in the upper $300\,\mathrm{m}$ at least during boreal summer by both current bands which might be related to the seasonal variability of the NECC and the nNECC [*Garzoli and Katz*, 1983].

At the lateral boundary of an OMZ (or a shadow zone in general), isopycnal eddy fluxes across the boundary play a significant role for the ventilation of the OMZ [*Luyten*

et al., 1983]. For the equatorial Atlantic, *Brandt et al.* [2008] argued that meridional eddy fluxes balance zonal advection within an eastward flowing jet along the equator, thus contributing to the ventilation of the off-equatorial regions. *Brandt et al.* [2010] further followed this hypothesis for an idealized mean zonal current system (including the nNECC band as well as the westward flow north and south of it). They find that in the upper part of the OMZ the diffusive lateral oxygen supply due to eddy fluxes is roughly of the same order of magnitude as the advective oxygen supply due to the mean zonal current system. In particular, the region between the equator and the southern boundary of the OMZ at roughly 5°N is characterized by strong intraseasonal variability associated with Tropical Instability Waves (TIW) [*von Schuckmann et al.*, 2008] that have been observed in a period band between $25\,\mathrm{d}$ - $50\,\mathrm{d}$ [*Athie and Marin*, 2008] and might contribute to the meridional ventilation of the OMZ.

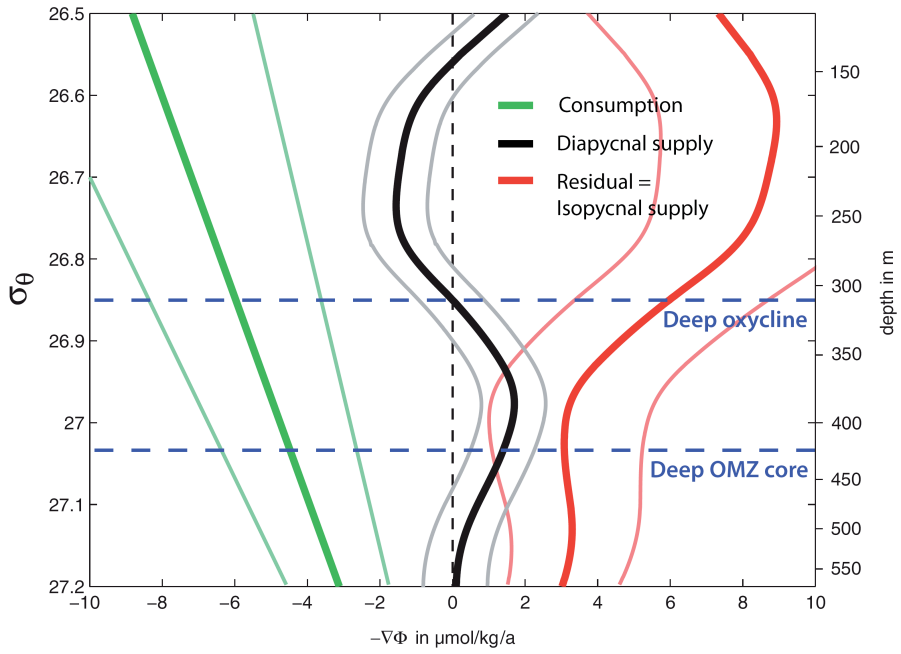

Figure 1.4. Oxygen consumption (green thick line), diapycnal oxygen supply (black thick line) and residual isopycnal oxygen supply (red thick line) in the Tropical North East Atlantic oxygen minimum zone. Thin lines mark the error estimates based on 95% confidence (after *Fischer et al.* [2012]).

Apart from the lateral (isopycnal) oxygen supply, *Fischer et al.* [2012] analyzed diapycnal mixing as a further mechanism for the ventilation of the TNEA OMZ. They estimate the mean oxygen supply due to diapycnal mixing in a depth range between $120\,\mathrm{m}$ and $570\,\mathrm{m}$ (Figure 1.4) and obtain a maximum oxygen supply of about $1.7\,\mu\mathrm{mol\,kg^{-1}\,yr^{-1}}$ at about $390\,\mathrm{m}$ depth slightly above the core of the OMZ. This value represents a contribution of about one third to the total oxygen supply required to balance the mean oxygen consumption as estimated by *Karstensen et al.* [2008]. Based on their results, *Fischer et al.*

[2012] define the isopycnal oxygen supply - either by diffusive or advective fluxes[4] - in a residual term by assuming a balance between consumption and supply and derive a first estimate of the oxygen budget in the TNEA OMZ (Figure 1.4). However, the isopycnal oxygen supply has not been estimated in an observational study so far. A quantitative determination of this term would refine the oxygen budget in the TNEA OMZ.

1.4 The aim of this study

As was shown earlier (section 1.2 and 1.3), a detailed picture of the mean upper-layer circulation and the resulting mean oxygen distribution in the Tropical Atlantic has been established during recent years which was mainly done in the framework of the collaborative research centre *"Climate-Biogeochemistry Interactions in the Tropical Ocean"* (2008-2015)[5]. Moreover, several studies have contributed to a better comprehension of the oxygen variability in the Tropical Atlantic, e.g. *Brandt et al.* [2012] propose a reasonable mechanism responsible for the equatorial oxygen variability at intermediate depths. However, a general picture of the oxygen variability in the Tropical Atlantic (as it exists for the mean oxygen distribution) is still missing.

In this study, a quantitative analysis of the oxygen variability in the Tropical Atlantic along 23°W is conducted. Local maxima of oxygen variability will be characterized and attributed to variance generating processes, where the TNEA OMZ is of particular interest. It is thought that oxygen variability is enhanced at the boundaries of the OMZ caused either by mesoscale stirring or diapycnal mixing of the mean oxygen gradient along or across isopycnal surfaces. By applying the extended Osborn-Cox model [*Ferrari and Polzin*, 2005], the respective role of these two processes in the production of oxygen variance will be identified.

Fischer et al. [2012] quantify the oxygen supply in the TNEA OMZ due to diapycnal mixing. An observation-based quantification of the isopycnal oxygen supply, comprising the supply due to mean currents as well as mesoscale eddies, is still required. Within this study, the meridional oxygen supply due to eddy fluxes is estimated and its contribution to the ventilation of the TNEA OMZ is quantified. Meridional eddy fluxes of oxygen are estimated by using (i) a flux gradient parameterization based on a lateral eddy diffusion coefficient and the mean isopycnal oxygen gradient and (ii) a correlation method based on velocity and oxygen mooring time series. Based on the flux gradient parameterization, the eddy-driven meridional oxygen supply is estimated and regional differences are characterized. Eventually, a refined picture of the oxygen budget in the TNEA OMZ will be derived.

[4] Based on their length and time scales, one distinguishes between lateral fluxes due to mesoscale eddies (diffusive flux) and due to mean currents (advective flux).

[5] www.sfb754.de

The analysis of the extended Osborn-Cox model and the estimate of the meridional eddy-driven oxygen flux and oxygen supply are based on a lateral eddy diffusion coefficient that is applied within a flux gradient parameterization. Using hydrographic and velocity data, two approaches (parameterization using (i) the mixing length theory and (ii) the Rhines scale) will be applied and combined to derive a mean depth profile of the lateral eddy diffusivity for the Tropical North East Atlantic.

Hydrographic and velocity data used in this study were obtained from repeat ship sections as well as moored observations carried out in the Tropical Atlantic along 23°W. The processing of CTD/O_2 data from shipboard observations follows standard procedures that ensure high quality data. In contrast, the oxygen measurements from moored observations are obtained with optode oxygen sensors which need to be calibrated to guarantee reliable operation. An in situ calibration procedure is derived to provide a method for the calibration during a research cruise. The calibration error for these oxygen sensors will be derived. Time constants of these sensors are estimated and a general method for the time constant correction is applied to improve the quality of oxygen measurements in profiling systems.

This research study is structured as follows: In chapter 2, an overview of the data is given that is used within this study. Chapter 3 describes the in situ calibration procedure for the optode oxygen sensors deployed for moored observations that are used within this study. The quantitative determination of the oxygen variability in the Tropical Atlantic is presented in chapter 4. In chapter 5, a mean depth profile of the eddy diffusivity in the Tropical Atlantic is described which is applied in the subsequent chapters for further analysis. While chapter 6 describes the diagnosis of the variance generating processes to identify the quantified oxygen variability (from chapter 4), chapter 7 evaluates the meridional oxygen flux and oxygen supply as well as time scales of the meridional oxygen flux. Additionally, a refined oxygen budget for the TNEA OMZ is derived at the end of this chapter. Eventually, chapter 8 summarizes and discusses the main results of this study. An outlook on future approaches is given in chapter 9.

CHAPTER 2

Data used within this study

2.1 Hydrographic and velocity data obtained from ship sections along 23°W

Within this study, velocity and hydrographic data along the 23°W section are used that were obtained during several research cruises in the Tropical Atlantic carried out between 1999 - 2011 (cf. Table A.1 for details). Velocity data were acquired with vessel-mounted and lowered ADCPs (vm-ADCP/l-ADCP); hydrographic data with a CTD/O_2 probe. Data records were taken into account from 22°W to 24°W and 6°S to 14°N (cf. Figure 2.1 for the characteristic meridional section). The narrow zonal extent that was chosen here is necessary to accurately estimate the local variability of hydrographic properties along 23°W as a function of latitude (cf. section 4.1).

Measurement errors for velocity and hydrographic data are the same as described in *Brandt et al.* [2010], who analyzed a similar data set that was based on ship sections taken between 22°W and 29°W in the period 1999 - 2008. For a single research cruise, the accuracy of $1\,\mathrm{h}$ averaged velocity data from vm-ADCP and single velocity profiles from l-ADCP was better than $2\,\mathrm{cm\,s^{-1}}$ - $4\,\mathrm{cm\,s^{-1}}$ and $5\,\mathrm{cm\,s^{-1}}$, respectively. By averaging all individual velocity sections, the mean velocity was estimated with an average standard error of $1.8\,\mathrm{cm\,s^{-1}}$ for the meridional range between 6°S and 14°N and the depth range $100\,\mathrm{m}$ - $1000\,\mathrm{m}$. The accuracy of hydrographic data was better than $0.001°\mathrm{C}$, 0.002 and $2\,\mu\mathrm{mol\,kg^{-1}}$ for temperature, salinity and dissolved oxygen, respectively.

In order to determine a velocity section along 23°W, the ADCP data were processed as described in *Brandt et al.* [2010], i.e. vm-ADCP/l-ADCP data were merged and meridional sections were determined on a regular grid (vertical resolution: $dz = 10\,\mathrm{m}$; merid-

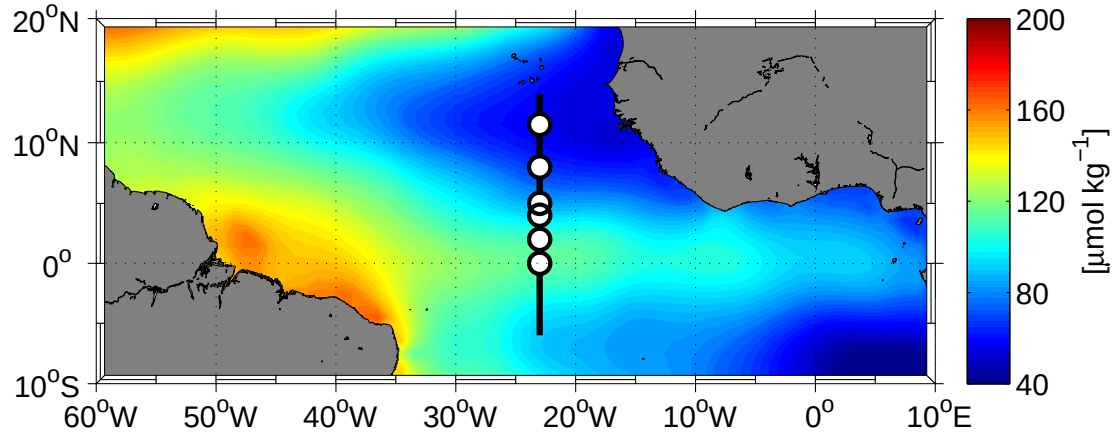

Figure 2.1. Locations of hydrographic and velocity measurements (cf. Appendix A for details) obtained (i) during repeat ship sections along 23°W between 6°S and 14°N (black line) and (ii) with moored observations (locations marked by white dots) at the equator, 2°N, 4°N, 5°N, 8°N and 11.5°N along 23°W. Underlaid is the oxygen distribution at 400 m depth as given by the World Ocean Atlas 2009 (WOA09, see section 2.3).

ional resolution $d\phi = 0.05°$) for each single ship section. Based on all meridional sections, the mean and the variability (standard deviation) of zonal and meridional velocity ($\bar{u}$,$\bar{v}$,σ_u,σ_v) was calculated for a depth range and a meridional range of 100 m - 1000 m and 6°S - 14°N, respectively. Henceforth, this section is referred to as the 23°W velocity section. The average standard error of the mean velocity was estimated to be 2.1 cm s^{-1} and 1.6 cm s^{-1} for the equatorial regime 6°S - 4°N and for the meridional range 4°N - 14°N, respectively.

2.2 Mooring data along 23°W

Along the 23°W meridian, hydrographic measurements were obtained with moorings located at the equator, 2°N, 4°N, 5°N, 8°N and 11.5°N (cf. Figure 2.1 and Table A.2 for details). The moorings at 4°N and 11.5°N were maintained in the framework of the international project PIRATA (*Prediction and Research Moored Array in the Atlantic*[6], *Bourles et al.* [2008]) and oxygen sensors (*AADI Aanderaa* optodes of model types 3830) were deployed at depths of 300 m and 500 m. For all other moorings[7], oxygen sensors (*AADI Aanderaa* optodes of model types 3830 and 4330) and CTD sensors (*Sea-Bird* microcats) were deployed together and were attached next to each other on the mooring cable to allow the interpolation of the measured oxygen on density surfaces. Overall, oxygen time series were recorded at the equator and 2°N at depths of 300 m and 500 m. At 5°N and 8°N, oxygen time series were obtained at depths from 100 m to 800 m with eight evenly

[6]Former: *Pilot Research Moored Array in the Tropical Atlantic*.
[7]Maintained within the collaborative research centre *SFB754* (www.sfb754.de).

distributed optode/microcat combinations per mooring (cf. Table A.3 for details). The sampling rate for all instruments was set to 2 h or better. During the mooring period March 2008 - Oct. 2009, the two optodes in the equatorial mooring only performed for about two weeks due to a too high power consumption. During the mooring period May 2011 - Oct. 2012, one optode (200 m) of the 5°N mooring only measured for about four months and the logger electronics of another optode (700 m) was missing at recovery most likely due to a pressure housing failure. All other optodes performed properly over their whole mooring period. Two microcats failed completely and three microcats developed corrupt conductivity cells, so only a fraction of the salinity data could be used for further processing. In case of missing microcat data, the optode temperature was used and salinity was estimated by applying a mean θ-S relation (θ being the potential temperature) obtained from water mass properties at nearby CTD measurements.

Most of the optodes were calibrated immediately before and after the mooring deployment[8] using the in situ calibration procedure which is proposed in section 3.4. In summary this is: the optode was attached to the CTD rosette and calibrated against oxygen measurements of a *Sea-Bird* CTD/SBE43 Clark electrode [*Carlson*, 2002] (which itself was regularly calibrated against Winkler titrated water samples onboard) during a regular CTD/O_2 cast. Additionally, onboard lab calibrations were performed by submerging every optode into a sodium sulfite solution containing zero oxygen. Based on all in situ and lab reference calibration points, one comprehensive calibration (hypercast calibration) was conducted. From the misfit against CTD/O_2 and lab calibration points, the root mean square error of the optode oxygen sensors was estimated in the range from $1.5\,\mu\mathrm{mol\,kg^{-1}}$ - $4.5\,\mu\mathrm{mol\,kg^{-1}}$ (average error $< 3\,\mu\mathrm{mol\,kg^{-1}}$, cf. sections 3.4 - 3.6 with respect to the error estimates).

Sea-Bird microcats were calibrated before and after the mooring deployment by attaching them to the CTD rosette. Temperature, conductivity and pressure sensors were linearly calibrated against temperature, conductivity and pressure, respectively, of the *Sea-Bird* CTD sensor. Only data from selected several minute long stops were used for the calibration in order to allow the relatively slow sensors to equilibrate. *Sea-Bird* microcats showed average calibration errors for temperature, salinity and pressure (if available) of $T \approx 0.012\,^\circ\mathrm{C}$, $S \approx 0.025$ and $p \approx 4\,\mathrm{dbar}$. The pressure sensors of some microcats showed a strong non-linear behavior near the surface resulting in an increased calibration error of up to $p \approx 9\,\mathrm{dbar}$.

Horizontal velocity was measured at the equatorial mooring as well as at 5°N, 23°W and 8°N, 23°W during different mooring periods (cf. Table A.4 for details) with downward or upward facing 75-kHz Longranger ADCPs. The sampling period and bin length was set to 2 h and 16 m, respectively. The minimum measurement range for the 5°N and 8°N mooring was from 100 m to 750 m so that depths of almost all optodes were covered.

[8] For logistic reasons, this could not be fulfilled for optodes from *PIRATA* moorings.

For the equatorial mooring, velocity data was used at depths of the oxygen sensors ($300\,\mathrm{m}$ and $500\,\mathrm{m}$). An ensemble number of 20 pings was chosen which resulted in a standard error of $1.7\,\mathrm{cm\,s^{-1}}$ for a single velocity data point. Following the manufacturer's compass accuracy of about 2° a velocity error of <4% of the absolute measured velocity was inferred.

2.3 Climatological data - World Ocean Atlas 2009

Most of the considered shipboard CTD/O_2 surveys followed the 23°W section (cf. Table A.1). These observations do not provide sufficient information on the hydrographic properties in zonal direction. For this purpose, climatological data from the World Ocean Atlas 2009 (WOA09, available at `http://www.nodc.noaa.gov/OC5/WOA09/pr_woa09.html`, described in *Locarnini et al.* [2010], *Antonov et al.* [2010], *Garcia et al.* [2010]) was used and mean salinity and oxygen distributions were calculated on potential density surfaces for the Tropical Atlantic.

CHAPTER 3

In situ calibration and time constant correction of optode oxygen sensors

In this chapter, a procedure for the in situ calibration of *AADI*[9] optode oxygen sensors is proposed, applied and discussed in detail. Common methods for the measurement of dissolved oxygen are introduced in section 3.1. Section 3.2 and 3.3 describe the optical measurement principle and current approaches for the calibration of optodes. The in situ calibration procedure is introduced in section 3.4 and applied in section 3.5 and 3.6. A calibration error is derived. Eventually, section 3.7 discusses the application of optodes in profiling systems (here: the example of a CTD/O_2 cast is used) - the optode time constant is estimated, a time constant correction is applied and its effect on the recorded oxygen profile is discussed.

3.1 Principle methods to determine dissolved oxygen in the ocean

More than a century ago, *Winkler* [1888] developed a simple and precise wet-chemical method to determine dissolved oxygen in water. Apart from few modifications [*Dickson*, 1995], the Winkler method has remained rather unchanged until today and is still the most accurate procedure for the determination of dissolved oxygen which makes it the standard reference method for the calibration of oxygen sensors. Despite this fact, a disadvantage of the Winkler method is the time-consuming procedure for a single point measurement. Thus, oceanographers nowadays use Clark sensors [*Clark et al.*, 1953] based on an electrochemical measurement principle to record continuous vertical profiles of dis-

[9] *Aanderaa Data Instruments* (`http://www.aadi.no`)

solved oxygen in the ocean's water column which is possible due to the small response time of these sensors. However, electrochemical sensors are prone to high drifts on time scales of months [*Carlson*, 2002] and need to be frequently calibrated.

Long-term oxygen measurements in the ocean - as conducted with moorings, floats and gliders on time scales of months and years - require a long-term stability of the used oxygen sensor. In the last two decades, the optical measurement of dissolved oxygen has experienced tremendous progress and has become an appropriate sensor technology for long-term measurements of dissolved oxygen in the ocean. The principle of this optical measurement will be introduced in the next section.

3.2 Optical measurement of dissolved oxygen

The underlying physical principle for the optical measurement of dissolved oxygen is the dynamic luminescence quenching [*Sinaasappel and Ince*, 1996; *Demas et al.*, 1999]. Luminescent molecules (luminophores) absorb light and subsequently emit this energy again partly in a nonradiative and a radiative (luminescence) decay. The emitted light is shifted to longer wavelengths compared to the absorbed light (Stokes shift). Both the lifetime (decay time) and intensity of the luminescence can be reduced by so-called quencher molecules. This is expressed by the Stern-Volmer equation which relates the amount of the quencher (considered here as the partial pressure pQ which is proportional to the quencher concentration $c(Q)$) to the lifetime or the intensity of the luminescence process in the luminophore:

$$\frac{I_0}{I} = \frac{\tau_0}{\tau} = 1 + K_{SV}(T) \cdot pQ. \tag{3.1}$$

τ_0 and τ (I_0 and I) define the decay time (the intensity) in absence and in presence of the quencher Q, respectively. $K_{SV}(T)$ is the Stern-Volmer coefficient (which is a function of temperature [*Sinaasappel and Ince*, 1996]) reflecting the quenching efficiency of the quencher molecules. In their studies *Sinaasappel and Ince* [1996] and *Demas et al.* [1999] discuss oxygen as an effective quencher and thus argue for an oxygen sensor based on luminescence-quenching.

Since 2002, *Aanderaa Data Instruments* (*AADI*, `http://www.aadi.no`) commercially distributes optical oxygen sensors, so-called optodes which are available for the application in oceanographic environments. The operating mode of an *AADI* optode is shown schematically in Figure 3.1. The luminophore in the sensor foil[10] is exposed to blue light emitted from a LED. After a decay time τ which varies with the partial pressure of oxygen in the sensing foil as given by (3.1), the luminophore emits red light with a longer

[10] A platinum porphyrine complex is used in *AADI* optodes that is embedded in a polymer layer; cf. manufacturer's manual [*AADI*, 2007].

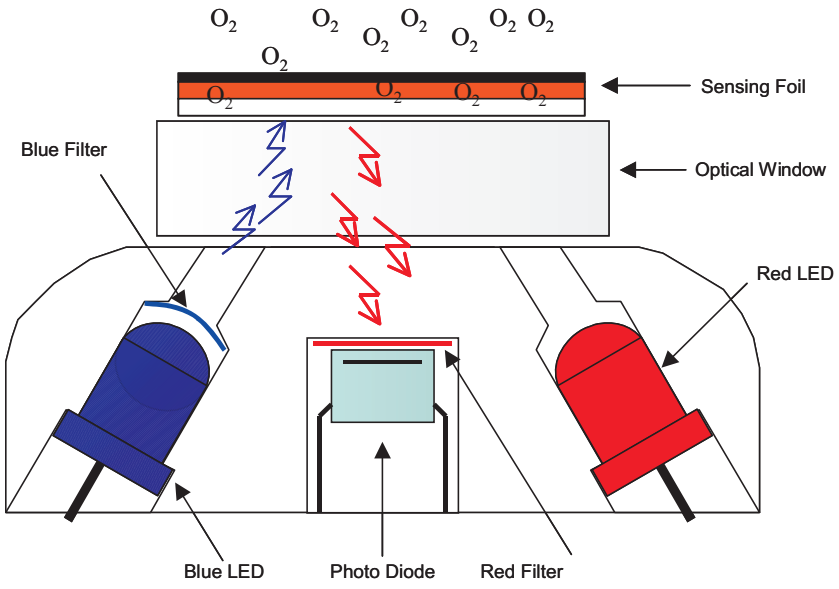

Figure 3.1. Schematic description of the operating mode of an optode (after *AADI* [*AADI*, 2007]). The luminophore in the sensing foil is excited with blue light of a LED and subsequently emits red light which is detected by a photo diode. The lifetime of the light-induced excited state of the luminophore molecules is dependent on the oxygen concentration in the sensing foil. Higher oxygen concentration results in a shorter lifetime following the Stern-Volmer equation (3.1).

wavelength detected by a photo diode. The phase shift P_b between the absorbed blue light and the emitted red light is a measure for the amount of oxygen in the sensing foil. New model types of *AADI* optodes use an additional red LED to determine a reference phase shift P_r and actually use the difference $P = P_b - P_r$ (without a reference LED, the reference phase shift is set to $P_r = 0$) for further processing of the measurement signal. However, the physical principle remains the same in both cases. In the following, reference is made only to the phase shift P as the raw measurement signal of the optode.

The applicability of *AADI* optodes for aquatic systems has been proved in several studies. *Körtzinger et al.* [2005] and *Tengberg et al.* [2006] show the long-term stability (up to 20 months) based on field experiments with profiling floats. However, they also point out the high response time due to diffusion of oxygen molecules into the sensor foil which limits the accuracy for a profiling system, particularly in regions with strong vertical oxygen gradients.[11] *Tengberg et al.* [2006] further attributed the optodes good accuracy ($2.1 \pm 5.1\,\mu\mathrm{mol\,l^{-1}}$, estimated from repeat measurements of a CTD-mounted optode against Winkler oxygen), limited cross-sensitivity as well as a lack of pressure hysteresis. Hence, optodes are a suitable alternative for oceanographic applications.

[11] Shorter response times can be achieved by using a fast response sensor foil (missing optical isolation of the foil), but this is at the cost of the sensor's noise and long-term stability, making the optode less suitable for long-term measurements [*Körtzinger et al.*, 2005].

3.3 Current approaches for the calibration of optodes

In principle, the phase shift P between the absorbed blue light and the emitted red light[12] of the luminophore is used as the physical measure for the amount of oxygen in the sensor foil and thus in the optode's environment. For the processing of the phase shift, *AADI* applies a polynomial with 20 calibration coefficients describing the dependence on temperature and phase shift up to the 4th order (cf. *AADI* [2007] and *AADI* [2009]). Even though a good accuracy is achieved, this is a rather heuristic approach to describe the characteristics of the optode sensor foil. A physically more intuitive description was proposed by *Uchida et al.* [2008] inspired by the Stern-Volmer relation (3.1). By analyzing both approaches, they find a systematic mismatch of oxygen data for *AADI*'s heuristic model, whereas *Uchida et al.* [2008]'s Stern-Volmer inspired model is more reasonable showing a comparable accuracy and a more homogeneous mismatch of the oxygen data.

Bittig et al. [2012] follow *Uchida et al.* [2008]'s model with a slight change. Whereas *Uchida et al.* [2008] directly calibrate against the concentration of dissolved oxygen in the surrounding fluid, *Bittig et al.* [2012] argue for a relation between the measured phase shift in the optode and the partial pressure of oxygen, since the oxygen solubility is different for both the carrier and the surrounding medium. The functional model for the foil characteristics after *Bittig et al.* [2012] is

$$\frac{P_0}{P'} = 1 + K_{SV} \cdot pO_2 \tag{3.2}$$

$$K_{SV} = c_0 + c_1 \cdot T + c_2 \cdot T^2 \tag{3.3}$$

$$P_0 = c_3 + c_4 \cdot T \tag{3.4}$$

$$P' = c_5 + c_6 \cdot P \tag{3.5}$$

$$pO_2 = \frac{c(O_2)}{\alpha(O_2, T)} \tag{3.6}$$

Equation (3.2) is the slightly changed Stern-Volmer equation (cf. (3.1)) with P_0 and P' denoting the phase shifts in the absence and in the presence of oxygen, pO_2 is the partial pressure of oxygen and K_{SV} is the Stern-Volmer coefficient as a function of temperature T given by (3.3). In fact, P_0 and P' are the corrected phase shifts given by (3.4) and (3.5) with the measured raw phase shift signal P of the optode. The partial pressure of oxygen is converted to the absolute oxygen concentration $c(O_2)$ following (3.6), with $\alpha(O_2, T)$ being the oxygen solubility according to Henry's law. (3.2) - (3.6) can be combined to one equation which relates the oxygen concentration to both the raw phase shift of the

[12] As in the previous section, it shall be noted again that new *AADI* model types carry an additional red LED for reference phase measurements, whereas the phase shift is calculated by $P = P_b - P_r$.

optode and the water temperature[13]:

$$c(O_2) = \alpha(O_2, T)\left(\frac{c_3 + c_4 \cdot T}{c_5 + c_6 \cdot P} - 1\right) \cdot \frac{1}{c_0 + c_1 \cdot T + c_2 \cdot T^2} \tag{3.7}$$

The oxygen concentration $c(O_2)$ can be considered as a function of the two-dimensional phase space[14] (P,T). In fact, $c(O_2)$ represents the oxygen concentration in freshwater at atmospheric pressure. A pressure correction has to be applied to $c(O_2)$ as described in the *AADI* manual [*AADI*, 2007]. Finally, the salinity correction for dissolved oxygen in seawater [*Garcia and Gordon*, 1992] is applied on the pressure corrected $c(O_2)$.

Bittig et al. [2012] conducted a sophisticated sensor performance analysis based on laboratory calibrations using (3.7) which were done prior to and after field experiments. On the one hand, the in situ measurement error based on the post deployment laboratory calibration was found to be smaller than $2\,\mu\mathrm{mol\,l^{-1}}$ indicating a small sensor drift. On the other hand, the authors found large drifts for some sensors when analyzing in situ measurements based on the pre deployment lab calibration. However, other sensors showed no severe drifts at all. Frequent sensor drifts were also found by *Uchida et al.* [2008] when comparing the sensor performance between different research cruises. Causes for such sensor drifts still remain unclear, but are suspected to be in the irreversible conditioning of the luminescent membrane either when exposed to high pressure or with time in case of brand-new sensors [*Bittig et al.*, 2012], or by simply mounting and demounting the optode for a measurement application [*Uchida et al.*, 2008].

Even though a long-term stability *during* field deployments could be attested to optodes [*Körtzinger et al.*, 2005; *Tengberg et al.*, 2006], the potential sensor drift *between* deployments makes a frequently repeated calibration necessary to understand this phenomenon. In principle, a calibration immediately prior to and after the field experiment would be best to avoid the effect of a sudden sensor drift which would diminish the quality of the calibration. Sophisticated laboratory calibrations are not practicable during a research cruise and thus do not fulfill the requirements for such a calibration procedure.

A suitable alternative is the onboard optode calibration during regular CTD/O_2 casts against Winkler samples [*Uchida et al.*, 2008]. Unfortunately, a complete calibration on the basis of a functional model as given in (3.7) is only applicable for a well chosen set of reference samples spanning a proper range in the two-dimensional phase space (P,T). This approach is often risky, since reference points for calibration are dependent on the local water mass properties and thus cover a particular path in the phase space (cf. section 3.5) providing only a very limited number of degrees of freedom. Using a tremendous number of CTD/O_2 casts as preformed by *Uchida et al.* [2008] extends the range of the regional

[13] Here, the system 'optode - surrounding water' is considered to be at equilibrium, so that the water temperature equals the temperature of the sensor foil.

[14] Here, the phase space is understood as the two-dimensional space spanned by the optode raw phase shift signal P (corresponding to the dissolved oxygen) and temperature T (cf. *Bittig et al.* [2012]).

water mass properties in the phase space which minimizes the degree of an extrapolation error of the field measurements from the calibration reference points. However, a large number of CTD/O_2 casts is very time consuming and cost-intensive and thus not reasonable only for the interest of calibration. Moreover, for a stand-alone measurement in the field (be it in a mooring, on floats or gliders), the optode has to be quickly ready for use during a research cruise without any time consuming calibration. A reliable in situ calibration procedure has to be designed, so that a limited number of reference points is sufficient to get a calibration of high quality which will be explained in the next sections.

3.4 Optode in situ calibration procedure

The requirements for an appropriate calibration procedure as discussed in section 3.3 are:

- applicable during a research cruise immediately prior to or after a field experiment
- little time consumption
- maximizing the accessible number of degrees of freedom

The following approach is suggested:

1. The functional model (3.7) is used to prescribe the general characteristics of the optode sensor foil. For this purpose, the calibration coefficients c_0 to c_6 are determined based on the reference points of an earlier laboratory calibration (either the manufacturer's calibration or an individual calibration as described in *Bittig et al.* [2012])[15]. Further, it is assumed that a drift of the optode sensor foil since the last laboratory calibration did not change the principle foil characteristics given by (3.7), but can be described by a linear correction of the raw phase shift P with respect to the raw phase shift itself and the temperature:

$$P_c = b_1 + b_2 \cdot P + b_3 \cdot T \tag{3.8}$$

The phase shift P' in (3.5) is then replaced by

$$\begin{aligned} P'_c &= c_5 + c_6 \cdot P_c \\ &= c_5 + c_6 \cdot (b_1 + b_2 \cdot P + b_3 \cdot T) \end{aligned} \tag{3.9}$$

[15] In this study, exclusively the manufacturer's initial laboratory calibration (conducted for every batch of sensor foils) is used to determine the coefficients c_0 to c_6.

Corresponding to (3.7) the oxygen concentration in surface freshwater[16] is now

$$c(O_2) = \alpha(O_2, T)\left(\frac{c_3 + c_4 \cdot T}{c_5 + c_6 \cdot (b_1 + b_2 \cdot P + b_3 \cdot T)} - 1\right) \cdot \frac{1}{c_0 + c_1 \cdot T + c_2 \cdot T^2} \tag{3.10}$$

Using (3.10), the optode oxygen sensor can be calibrated in both dimensions of the phase space (P, T) applying the three calibration coefficients b_1, b_2 and b_3.

2. The optode oxygen sensor is calibrated before and after the field deployment during regular CTD/O_2 casts. Henceforth, these CTD/O_2 casts are called the pre and post deployment calibration casts. For this purpose, the optode is attached to the CTD rosette and calibration points are collected against reference oxygen measurements of a CTD Clark electrode[17] which itself is calibrated against Winkler titrated water samples. Reference points for calibration are chosen at calibration stops[18] during the CTD/O_2 cast, conducted at depths with a weak vertical oxygen gradient and minimum break time of $2\,\mathrm{min}$ to ensure an equilibrated oxygen sensor[19].

3. In general, the full oxygen range (0% - 100% oxygen saturation) is generally not covered with a CTD/O_2 cast, but depend on the local water mass characteristics. In order to increase the degrees of freedom for the calibration, an onboard lab calibration was performed by submerging the optode into a sodium sulfite solution ($5\,\mathrm{g}$ Na_2SO_3 per $500\,\mathrm{ml}$ water as recommended by the manufacturer) containing zero oxygen at two different temperatures ($\sim 5\,^\circ\mathrm{C}$ and $\sim 20\,^\circ\mathrm{C}$) to ensure that the central temperature range[20] at zero oxygen is covered within the calibration.

4. All reference points from the pre and post deployment calibration casts as well as the pre and post deployment lab calibrations are used together to evaluate the calibration coefficients b_1, b_2 and b_3 based on (3.10)[21]. In the following, this kind of calibration is called *hypercast calibration*. The error (in the phase space) for the field observations during the deployment can be calculated from the misfit $\Delta O_2^{opt-ctd}(P,T)$ against the reference points and the root mean square error of the CTD Clark sensor against all Winkler samples conducted during the cruise (RMSE($\Delta O_2^{ctd-Winkler}$)), i.e. $\Delta O_2^{opt}(P,T) = \sqrt{(\Delta O_2^{opt-ctd}(P,T))^2 + (\mathrm{RMSE}(O_2^{ctd-Winkler}))^2}$.

[16] As mentioned in section 3.3, the pressure correction for the optode sensor foil and the salinity correction for dissolved oxygen in seawater have to be applied afterward to get the in situ oxygen concentration.
[17] In general, this is a *Sea-Bird* 43 Clark electrode [*Carlson*, 2002].
[18] If no stops are performed, locations with a weak vertical oxygen gradient are chosen. A time lag correction has to be applied to minimize the systematic error due to the high optode response time (cf. section 3.7).
[19] Time constants of optode oxygen sensors are at about $15\,\mathrm{s}$ - $20\,\mathrm{s}$ with 63% adjustment (cf. section 3.7).
[20] Generally, the temperature range should be adapted to the field conditions.
[21] Remember the pressure correction for *AADI* optodes [*AADI*, 2007] (a correction factor of $0.04/1000\,\mathrm{dbar}$ is used) as well as the salinity correction for dissolved oxygen in seawater [*Garcia and Gordon*, 1992].

A schematic description of the calibration procedure is shown in Figure 3.2.

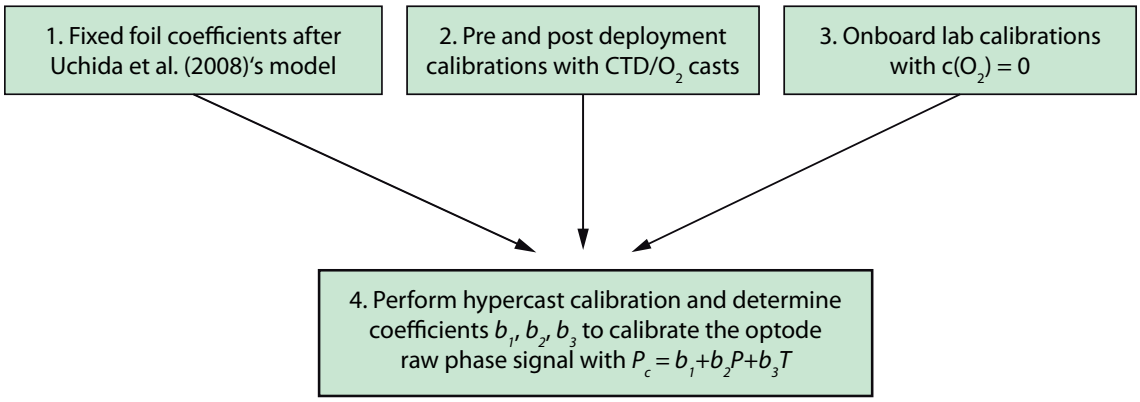

Figure 3.2. Schematic description of the optode calibration procedure. In step 1, the general characteristics of the sensor foil are defined. In steps 2 and 3, the reference samples for calibration are collected. Information obtained from steps 1 - 3 are used together in step 4 for the evaluation of one final hypercast calibration (see text for details).

3.5 Application of the optode in situ calibration procedure

The application of the optode in situ calibration procedure as described in the previous section will be presented in the following. For the analysis, 34 different *AADI* optodes (both model types 3830 and 4330) were used. The optode sensor foil coefficients c_0 to c_6 of every optode were evaluated after (3.7) using a least squares fit against the reference points from the manufacturer's initial laboratory calibration which was carried out for each specific set of sensor foils directly after fabrication (step 1). All analyzed optodes were deployed in the Tropical Atlantic in the upper $800\,\mathrm{m}$ during a mooring period with a duration of about 1.5 years[22]. The optodes were calibrated before and after a deployment period against reference points from regular CTD/O_2 casts (step 2) carried out in the Tropical Atlantic along 23°W (with an average depth of $1000\,\mathrm{m}$) as well as against zero oxygen content during onboard lab calibrations (step 3). Based on all reference measurements, one final hypercast calibration was conducted (step 4).

Since the number of reference samples from the onboard lab calibration was smaller than the number of reference samples from the in situ calibration, the calibration points at zero oxygen were weighted together with 20%, whereas all in situ calibration points together were weighted with 80% within the hypercast calibration. 7 optodes were deployed during two adjacent mooring periods (including also a calibration between both periods) and 27 optodes were deployed during one mooring period. Hence, overall 41

[22] In principle, the optodes used for this analysis are those that were deployed in the moorings in the Tropical Atlantic (cf. Table A.2).

hypercast calibrations based on 34 different optodes were used in the following analysis.

As an example, Figure 3.3 shows the calibration of an optode against pre deployment (3.3a) and post deployment (3.3b) calibration points as well as against all reference points (hypercast calibration, 3.3c) from both pre and post deployment calibration. Here, oxygen is referenced to a surface freshwater concentration following (3.10) which describes an oxygen hypersurface in the two-dimensional phase space (P, T). The least square fitted hypersurfaces as well as the reference points from pre deployment, post deployment and hypercast calibration are shown in the left panels of 3.3a, 3.3b and 3.3c, respectively. In the pre deployment calibration, only one reference measurement against water containing zero oxygen was carried out at room temperature, whereas two reference measurements against zero oxygen were performed in the post deployment calibration (two different temperatures).

Basically, a calibration error $\Delta O_2^{opt-ctd} = optode - reference$ for the optode oxygen sensor can be derived based on the misfit against the reference samples (see right panels of 3.3a and 3.3b) from the individual pre and post deployment calibrations. This misfit represents the mismatch of the functional model (3.10) used to describe the sensor characteristics. An error due to a potential sensor drift during the mooring period cannot be revealed by this approach. The hypercast calibration as shown in Figure 3.3c includes this potential error when fitting against the reference samples from both pre and post deployment calibrations. Here, the degrees of freedom are increased due to the increased number of calibration points. The optode oxygen error is more reasonable comprising now the mismatch of the functional model as well as potential sensor drifts. In this particular case, no evident drift of the oxygen sensor was observed when comparing the reference samples prior to and after the mooring period (Figure 3.3c). The root mean square error (RMSE) of the oxygen misfits from the hypercast calibration (given in the right panel) is comparable to the field misfits based on laboratory calibrations [*Bittig et al.*, 2012]. Hence, the calibration error is mainly due to the mismatch of the functional model[23].

The optode oxygen error in Figure 3.3 is expressed in the two-dimensional phase space as a function of the optode raw phase shift P and the temperature T. It is more reasonable to consider the error as a function of oxygen concentration and temperature, since the raw phase shift P is a sensor specific value, whereas the oxygen concentration is - of course - independent from the sensor specifications. Since the error of the in situ oxygen concentration is of main interest, henceforth the error is referred to the oxygen concentration in units of $[O_2] = \mu\mathrm{mol\,kg^{-1}}$ (implying the pressure correction for *AADI* optodes [*AADI*, 2007] with a correction factor of $0.04/1000\,\mathrm{dbar}$ as well as the salinity correction for dissolved oxygen in seawater [*Garcia and Gordon*, 1992]). The consideration of the

[23] Here, also the error of the reference calibration points possibly contributes to the mismatch. The misfit of the CTD Clark sensor to Winkler samples is in general between $1\,\mu\mathrm{mol\,kg^{-1}} - 2\,\mu\mathrm{mol\,kg^{-1}}$.

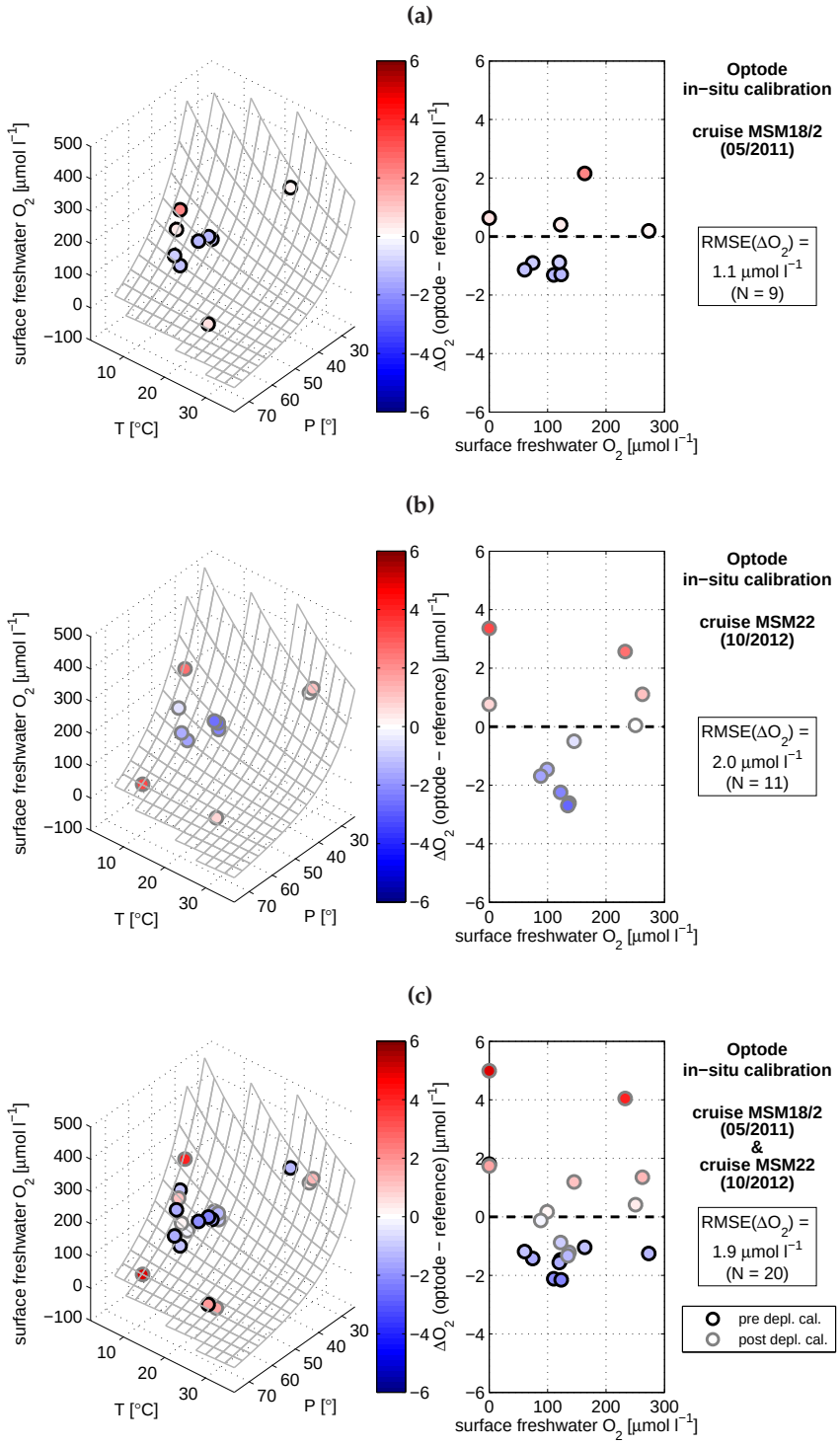

Figure 3.3. In situ calibration of an optode (model type 3830) based on reference samples from CTD/O_2 calibration casts and onboard lab calibrations. (a) Pre deployment calibration. (b) Post deployment calibration. (c) Hypercast (combined pre and post deployment) calibration. Left and right panel in (a), (b), (c) show the fitted hypersurface after (3.7) and the misfit of the optode oxygen against CTD/O_2 reference samples, respectively. Colored dots mark the difference between optode oxygen and CTD/O_2 reference.

oxygen error as a function of oxygen concentration and temperature further allows a comparison of the calibration errors from different optode oxygen sensors.

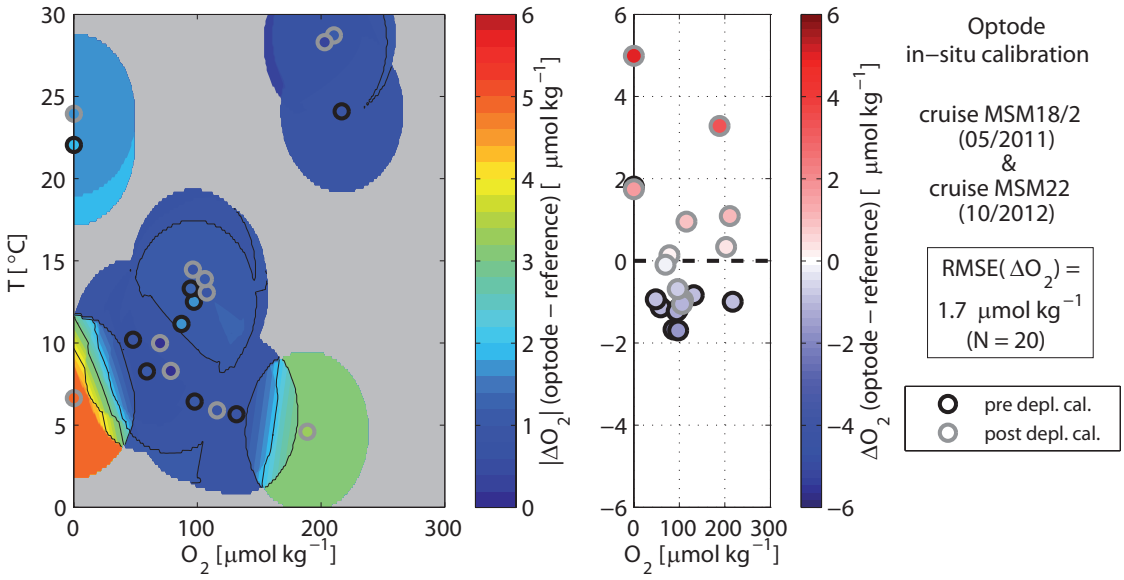

Figure 3.4. Estimate of the optode oxygen error ($\Delta O_2 = optode - reference$) referred to the in situ oxygen concentration from the hypercast calibration shown in Figure 3.3. The left panel shows the oxygen error in the two-dimensional phase space (O_2, T). Colored dots mark the oxygen error at the reference points (gray/black edge color represents pre/post deployment calibration points). Colored contours show the Gaussian weighted oxygen error calculated using (3.11). The right panel shows the oxygen error at the reference points as a function of oxygen concentration.

The oxygen error for the optode, calibrated in Figure 3.3, is given as a function of the in situ oxygen concentration and temperature in Figure 3.4. The left panel shows the absolute value $|\Delta O_2|$ from the hypercast calibration in the phase space (O_2,T). Based on the misfits at the reference points, a two-dimensional Gaussian interpolation scheme was used to estimate regimes for the magnitude of the oxygen error which is given by

$$\Delta O_2^w(O_2, T) = \frac{\sum_k w_k \Delta O_{2k}(O_{2k}, T_k)}{\sum_k w_k} \tag{3.11}$$

where $\Delta O_{2k}(O_{2k}, T_k)$ are the misfits against the reference points and w_k are the weighting factors based on a two-dimensional (O_2,T) Gaussian distribution with influence and cutoff radii of oxygen (O_{2i}, O_{2c}) and temperature (T_i, T_c), respectively. Values for these radii were chosen such that a rather isotropic dependence on O_2 and T was given in the phase space ($O_{2i} = 25\,\mu\mathrm{mol\,kg^{-1}}$, $O_{2c} = 50\,\mu\mathrm{mol\,kg^{-1}}$, $T_i = 2.5\,^\circ\mathrm{C}$, $T_c = 5\,^\circ\mathrm{C}$)[24]. Of course, distinct minima of the oxygen error were found at $O_2 - T$ properties, where most of the reference samples were taken, i.e. at about $50\,\mu\mathrm{mol\,kg^{-1}}$ - $150\,\mu\mathrm{mol\,kg^{-1}}$ and

[24] Strictly speaking, decorrelation scales in the two-dimensional phase space had to be estimated to define these influence and cutoff radii.

5 °C - 15 °C. For this special optode, low oxygen errors were also found for high oxygen concentrations and high temperatures as well as zero oxygen concentrations and high temperatures. Large errors were found for both zero oxygen and high oxygen at low temperatures, indicating that the foil characteristics are not well described by the functional model (3.10) for these phase space properties.

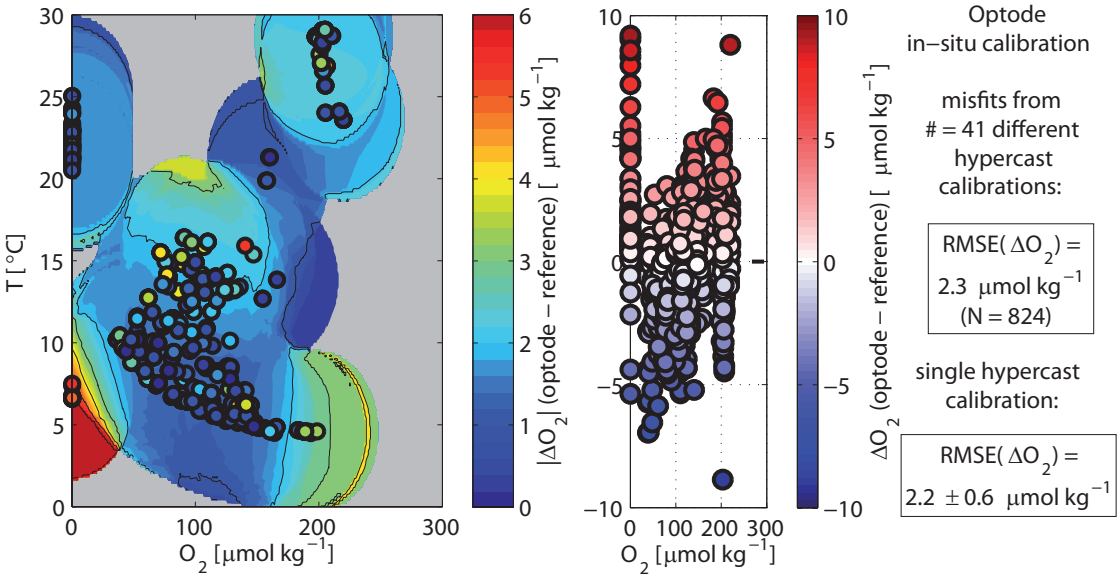

Figure 3.5. Average optode oxygen error estimated for 34 different optodes (41 individual hypercast calibrations). Left and right panel show the same parameters as in Figure 3.4, but no differentiation between pre and post deployment calibration points is made.

The optode oxygen error was determined for every individual optode hypercast calibration as described above. A composition of the oxygen misfits from all calibrations is shown in Figure 3.5. Since all in situ calibrations were conducted roughly in the upper $1000\,\mathrm{m}$ in the Tropical Atlantic along 23°W, the characteristic scatter of the regional $O_2 - T$ properties is obvious in the phase space (left panel of Figure 3.5) between about $40\,\mu\mathrm{mol\,kg^{-1}} - 220\,\mu\mathrm{mol\,kg^{-1}}$. The reference points from onboard lab calibrations against zero oxygen are concentrated at two different temperatures in the phase space. The distribution of the oxygen error in the phase space is comparable to the example error estimate shown in Figure 3.4, where a large misfit is found at low temperatures and zero oxygen as well as at low temperatures and high oxygen. Based on all calibration points, a root mean square error of $\mathrm{RMSE}(\Delta O_2) = 2.3\,\mu\mathrm{mol\,kg^{-1}}$ was calculated. This error varies for individual optodes within one standard deviation of $0.6\,\mu\mathrm{mol\,kg^{-1}}$. Assuming a normal distribution, the average error of an optode is $4.6 \pm 1.2\,\mu\mathrm{mol\,kg^{-1}}$ with 95% confidence (double the standard deviation)[25].

[25] Of course, this estimate is only valid for the analyzed O_2-T properties in the phase space. When applying extrapolation in the phase space, the calibration error can increase.

Although the estimated in situ calibration error is larger than the calibration error of a laboratory calibration, the error is substantially smaller than the error due to a drift of the oxygen sensor (cf. *Bittig et al.* [2012]). In comparison to the laboratory calibration, the larger in situ calibration error can result from the higher uncertainty of in situ oxygen reference measurements used for the calibration. Moreover, a slight change of the principle sensor foil characteristics might have occurred since the initial manufacturer's laboratory calibration which cannot be corrected completely by a linear fit of the raw phase shift P as in (3.8). Nevertheless, the magnitude of this error suggests that the general characteristics of the optode sensor foil are still valid. Severe sensor drifts were not observed when comparing the pre and post deployment calibrations. Therefore, the in situ calibration procedure proposed here is a reasonable approach to calibrate optodes with a small number of reference points. The calibration is valid for field applications close to the reference calibration points, whereas an extrapolation to other field properties can lead to an increased error.

The distribution of the optode oxygen error in the phase space certainly depends on the weight of every individual calibration point. In general, all reference samples at zero oxygen were weighted together with 20%, whereas all other calibration points were uniformly weighted all together with 80% within the hypercast calibration. Figure 3.6a and 3.6b show the cases of a 10% and a 30% weight of the zero oxygen calibration points, respectively. In particular, a higher weight of the zero oxygen calibration points is applied, if extremely low oxygen concentrations were observed during a field deployment which evidently reduces the calibration error for these measurements. This is a reasonable approach, because the reference samples from the onboard lab calibration were chemically forced to zero oxygen and thus provide a high accuracy.

3.6 Calibration of optode oxygen time series

In the previous section, the optode calibration procedure was applied to estimate the calibration coefficients b_1, b_2 and b_3 as well as the optode calibration error from pre and post deployment calibration casts. In this section, the application of the calibration coefficients and the estimated error on an in situ oxygen time series shall be shown using a moored optode as an example. Basically, the calibration is straight forward by applying (3.10) to the time series of the raw phase shift P. The temperature time series is either taken from the optode temperature sensor or from another temperature sensor attached right next to the optode (e.g. a *Sea-Bird* microcat). Subsequently, salinity [*Garcia and Gordon*, 1992] and pressure correction [*AADI*, 2007] are applied. If no time series of salinity exists, it is approached by considering the local $\theta - S$ (θ being the potential temperature) water mass characteristics obtained from nearby CTD measurements.

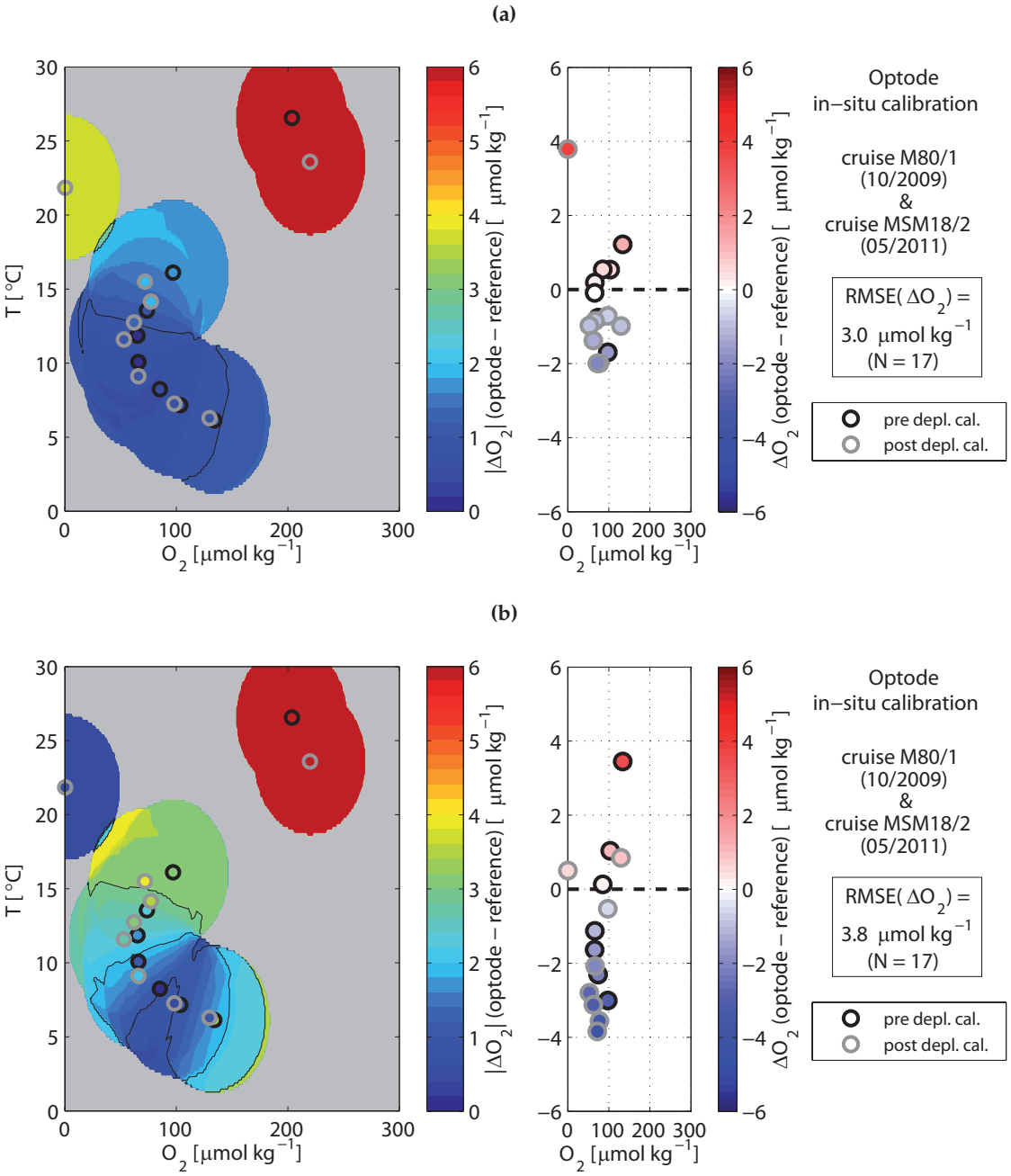

Figure 3.6. Optode oxygen error for different weights of the reference calibration point at zero oxygen. Same parameters are shown as in Figure 3.4. (a) 10% weight of the zero oxygen calibration point. (b) 30% weight of the zero oxygen calibration point.

Figure 3.7 shows the calibrated oxygen and its error from an optode moored in the CVOO mooring (17.6°N, 24.25°W) north east of the Cape Verde Islands. The left panel depicts the error estimate of the calibrated oxygen as a function of the calibrated oxygen itself and temperature. This error estimate relies on the misfit of the optode oxygen against the reference calibration points from the pre and post deployment calibrations. Influence and cutoff radii for oxygen and temperature in the two dimensional phase space were used as defined in section 3.5 ($O_{2i} = 25\,\mu\text{mol kg}^{-1}$, $O_{2c} = 50\,\mu\text{mol kg}^{-1}$, $T_i = 2.5\,^{\circ}\text{C}$,

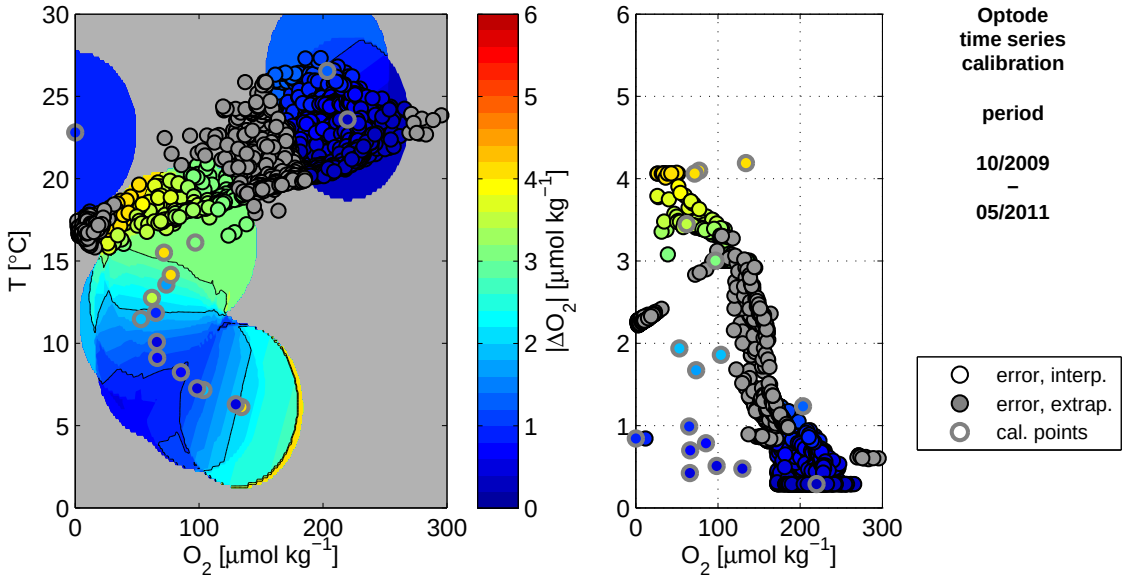

Figure 3.7. Oxygen time series calibration of an optode recovered from a mooring deployment (moored in the CVOO mooring off the Cape Verde Islands). The left panel shows the absolute calibration error as a function of the oxygen concentration and temperature. The right panel shows the absolute oxygen error as a function of the oxygen concentration (cf. also with Figure 3.4). Colored circles with gray contour mark the calibration points from the pre and post deployment calibrations. The underlying colored contours in the left panel show the Gaussian weighted absolute oxygen error calculated using (3.11) based on the calibration points. Colored circles with black contour represent the calibrated field measurements close to the calibration points in the phase space. Gray circles with black contour indicate calibrated field measurements extrapolated from the calibration points.

$T_c = 5\,^\circ\mathrm{C}$). The optode was moored at a depth of $54\,\mathrm{m}$ and was exposed to oxygen concentrations from about $0\,\mu\mathrm{mol\,kg^{-1}}$ up to the saturation concentration throughout the mooring period[26]. Here, the onboard lab calibration against zero oxygen content was essential to get a satisfactory estimate of the low oxygen concentrations measured by the optode. Unfortunately, only one onboard lab calibration against zero oxygen was conducted (at room temperature), so that a slight extrapolation of the calibration was necessary. In case of measurement points that were off the reference calibration points (from the pre and post deployment calibration) in the phase space, the calibration error was estimated as a best guess by increasing the cutoff and influence radii of the reference calibration points[27].

[26] In the Tropical Atlantic, such low oxygen concentrations, suggesting a hypoxic regime, had never been observed before. However, this phenomenon is not further considered here, but is investigated in a study by *Karstensen et al.* [2013] (*under revision*).

[27] Strictly speaking, a sensitivity analysis (e.g. using the bootstrapping method) should be performed to characterize the robustness of the calibration, particularly for an extrapolation of the calibration.

3.7 Application in profiling systems - time constant correction

3.7.1 Motivation for the time constant correction

The optode oxygen sensor is subject to physical inertia which is mainly caused by the slow diffusion of oxygen into the sensing foil. Thus, the sensor responds to temporal changes of dissolved oxygen with a certain time lag. Whereas in an equilibrated state a good accuracy is achieved as shown in section 3.5, a large bias between the measured and the true oxygen concentration can occur within profiling applications such as CTD/O_2 casts, in gliders or floats. As an example, Figure 3.8 shows the first $5\,\mathrm{min}$ of an oxygen profile recorded during a CTD/O_2 cast (profiling speed $1\,\mathrm{m\,s^{-1}}$) with both a CTD Clark sensor and a CTD-mounted optode. In comparison to the fast response time of the Clark sensor, the optode oxygen signal is strongly time lagged and smoothed. This becomes particularly obvious when profiling through large oxygen gradients as between $1.5 - 2.5\,\mathrm{min}$.

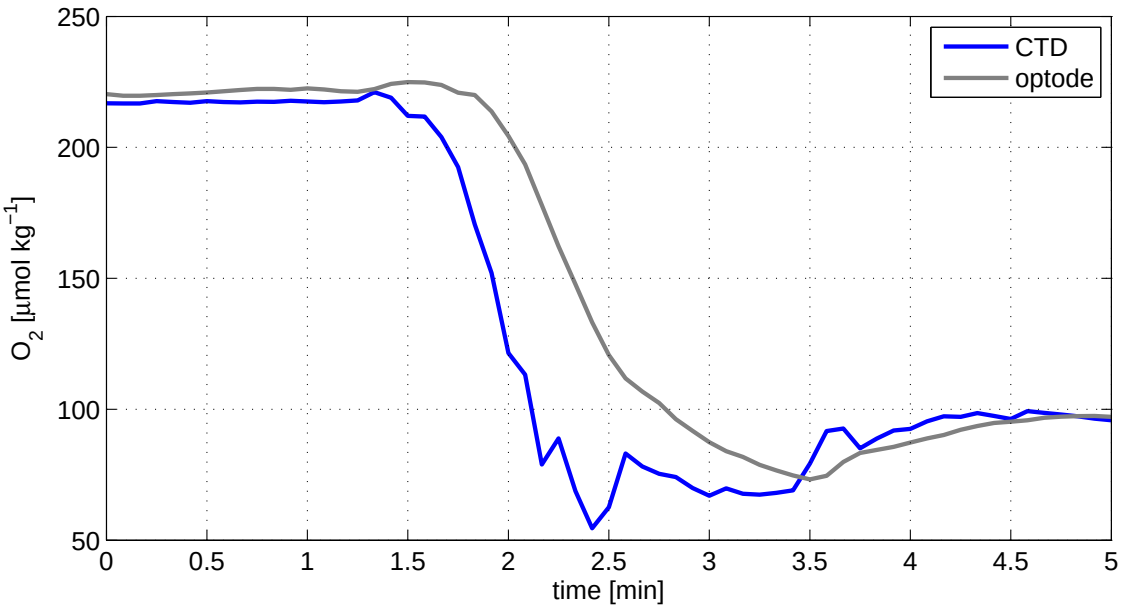

Figure 3.8. First $5\,\mathrm{min}$ of a CTD/O_2 profile combined with the oxygen profile of an optode which was attached to the CTD rosette. Strong oxygen gradients, as seen between $1.5 - 2.5\,\mathrm{min}$ lead to a large time lag of the optode signal due to the high sensor time constant.

The response function of a sensor (here of the optode) can be generally described with an exponential behaviour. Mathematically, the response of the optode to temporal changes of oxygen is expressed by a convolution of the true oxygen signal $O_2(t)$ with the response function of the optode, defined as $h = \mathrm{e}^{-\frac{t}{\tau}}$. Here, τ is the time constant of

the optode oxygen sensor which defines the time, of which a 63% adjustment to the true oxygen concentration is achieved. A mathematical overview about the response function of a sensor is given in Appendix B. For discrete sampling, the response of an optode to temporal changes of the dissolved oxygen is given by

$$O_2^{opt}(t_0) = O_2(t_0) \cdot (1 - \mathrm{e}^{-\frac{\triangle t}{\tau}}) + O_2^{opt}(t_0 - \Delta t) \cdot \mathrm{e}^{-\frac{\triangle t}{\tau}} \tag{3.12}$$

where $O_2^{opt}(t_0)$ is the optode oxygen signal and $O_2(t_0)$ is the true oxygen concentration at the time point t_0. Δt is the sampling time of the optode, i.e. $O_2^{opt}(t_0 - \Delta t)$ is the optode oxygen signal at the previous time step. The recursive expression of O_2^{opt} in (3.12) is a simple model to describe the time response of the optode, but requires an accurate initial value of the optode oxygen signal in a steady state. Reversed, (3.12) can be used to approach the true oxygen signal $O_2(t)$ by deconvoluting the optode oxygen signal $O_2^{opt}(t)$.

The approach to correct sensor signals attributed with time constant τ is already know and was e.g. applied and validated for radiosonde humidity measurements in the atmosphere [*Miloshevich et al.*, 2004]. *Fiedler et al.* [2013] used the correction given in (3.12) to post-process pCO_2 sensor data from profiling floats. Nevertheless, no comparison of optode oxygen sensors to reference measurements was done so far in order to validate the approach in (3.12) for optodes in oceanic applications. In the following section, a procedure is presented to estimate the time constant τ of an optode from in situ measurements against a CTD Clark sensor. The estimated time constant will be used to deconvolute the optode oxygen signal and try to mimic the reference CTD oxygen profile.

3.7.2 Estimate of the optode time constant and application of the time constant correction

In this section, the convolution of the optode signal as given in (3.12) is used to estimate the time constant τ of the optode oxygen sensor. With this time constant at hand, the optode oxygen signal O_2^{opt} is corrected using (3.12) to mimic the true oxygen profile which is assumed to be well defined by the CTD oxygen profile.

The basic idea for the estimate of the optode time constant is to model the optode oxygen profile with a convoluted reference CTD oxygen profile using (3.12) with a defined time constant. Out of a specific range of time constants, a best approximation for the optode oxygen profile is determined which provides the time constant of the optode. In principle, this could be achieved by finding the minimum root mean square error of the convoluted reference CTD oxygen profile against the optode oxygen profile. However, several effects can lead to a bias of the estimated time constant, e.g. the optode sensor noise, oxygen variability on short time and length scales, an inaccurate time shift

between both sensor signals[28], or the calibration error of the optode oxygen sensor. To separate these effects for the time constant estimate, the Fourier spectra of the signals are considered in a certain period band instead of using the signals itself.

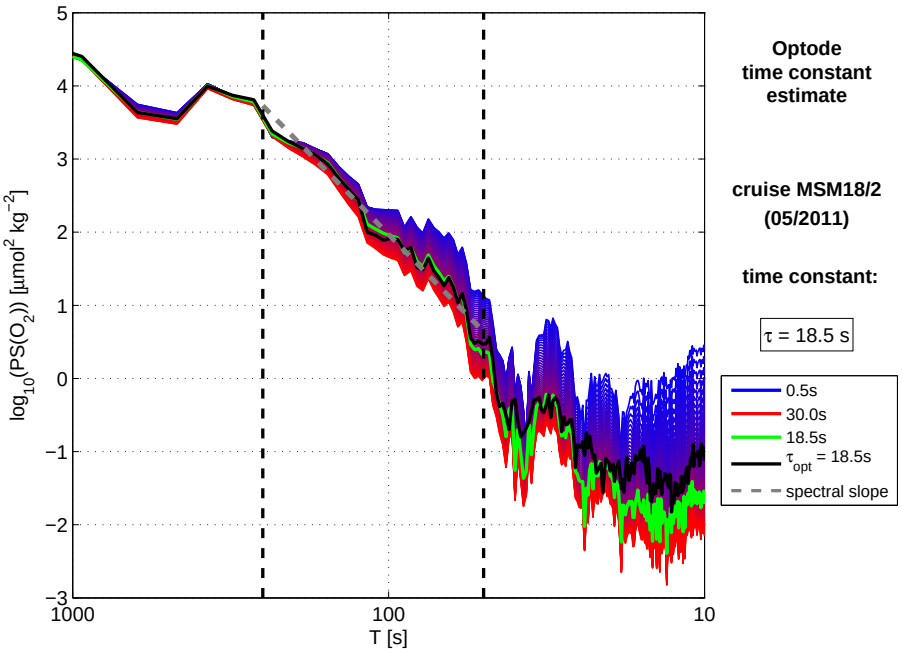

Figure 3.9. In situ estimate of the optode time constant using spectral analysis. Bluish to reddish colors show the power spectrum of the CTD oxygen profile that was convoluted with various time constants between 0.5 s - 30 s. In black, the power spectrum of the optode oxygen profile is shown. Gray dashed line marks the spectral slope of the optode oxygen power spectrum. The power spectrum of the convoluted CTD oxygen profile (with time constant τ) that fits best to the optode oxygen spectrum is marked by the green line. Vertical dashed lines show the period range (250 s - 50 s) that was used for the estimate of the time constant.

As an example, the Fourier spectra of the optode oxygen profile and the convoluted CTD oxygen profile are shown in Figure 3.9. Here, the CTD oxygen profile was convoluted with various time constants between 0.5 s - 30 s. A small time constant leads to a less damped signal on short time scales and thus to a smaller drop-off of the spectrum (bluish colors), whereas a large time constant leads to a steeper spectral slope (reddish colors) in the double logarithmic presentation (cf. the characteristics of the transfer function of the convolution in Figure B.1). The spectrum of the optode signal is shown in black. By comparing the spectral slopes (including the offset) of the different convolutions of the CTD oxygen profile with the spectral slope of the optode oxygen profile, a best approach (minimum root mean square error) for the spectral slope is determined (gray dashed line). The corresponding spectrum of the convoluted CTD oxygen profile with the time constant τ is highlighted in green line.

[28] Apart from the time constant effect itself, both signals can be subject to a time shift against each other.

The spectral slopes of the optode oxygen profile and the convoluted CTD oxygen profile are compared in a period band between $250\,\mathrm{s}$ and $50\,\mathrm{s}$, since (i) a distinct bifurcation of the spectra of the convoluted CTD oxygen profile exists in this band and (ii) the effects of oceanic variability as well as sensor noise on time scales roughly below $20\,\mathrm{s}$ can be neglected. The higher spectral energy of the optode oxygen profile - in comparison to the best approaching convoluted CTD oxygen profile - is particularly present for time scales close to the Nyquist frequency of $1/10\,\mathrm{s}^{-1}$ (i.e. a sampling time of $5\,\mathrm{s}$) which is likely due to the white noise of the sensor as well as oxygen variability on small time scales.

Using this method, the analyzed optode in Figure 3.9 was attributed with a time constant of $\tau = 18.5\,\mathrm{s}$ for a single CTD/O_2 cast. To better estimate the true optode time constant, an average of the time constant estimates from the pre and post deployment calibration casts (hypercast calibration) is determined.

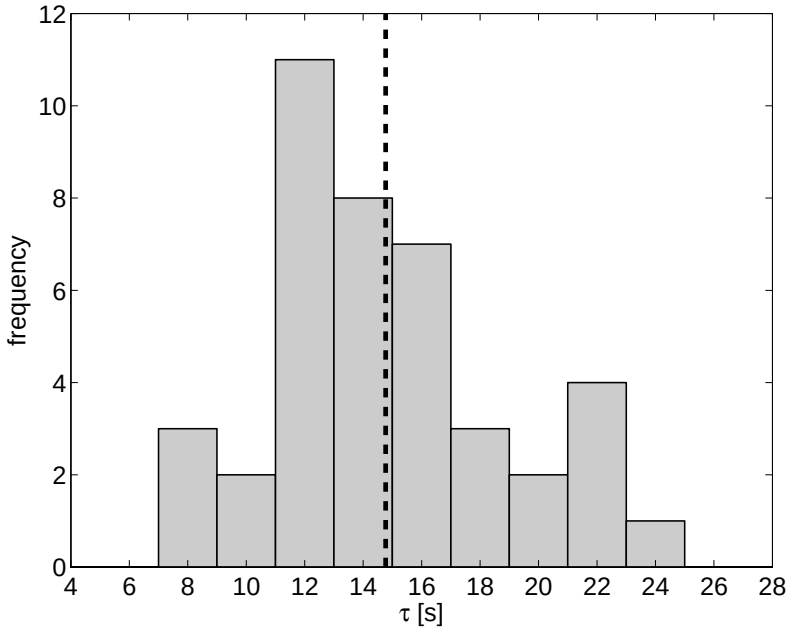

Figure 3.10. Frequency distribution of the optode time constant. The optode time constants were estimated from parallel measurements of the optode and a CTD Clark sensor. The average time constant was estimated to $\tau = 14.8\,\mathrm{s}$ with one standard deviation of $\sigma_\tau = 3.9\,\mathrm{s}$.

For every single hypercast calibration of an optode that was considered in section 3.5 (34 different optodes, 41 hypercast calibrations), an average time constant was estimated from the pre and post deployment calibration cast. Finally, a total mean over all optode hypercast calibrations was calculated yielding a time constant $\tau = 14.8\,\mathrm{s} \pm 3.9\,\mathrm{s}$ (Figure 3.10). *Uchida et al.* [2008] found a temperature dependence of the time constant by applying a temperature dependent time shift on the optode oxygen profile, even though the applied method is rather heuristic and not based on the characteristics of a sensor response function as discussed here or by *Miloshevich et al.* [2004]. From laboratory ex-

periments, *H. C. Bittig (pers. comm.)* found a temperature dependence of the optode time constant with a slope of $-0.40\,\mathrm{s\,K^{-1}}$. This temperature dependence was used within this analysis[29] and the time constants as reported above are given with respect to a reference temperature of $20\,^{\circ}\mathrm{C}$.

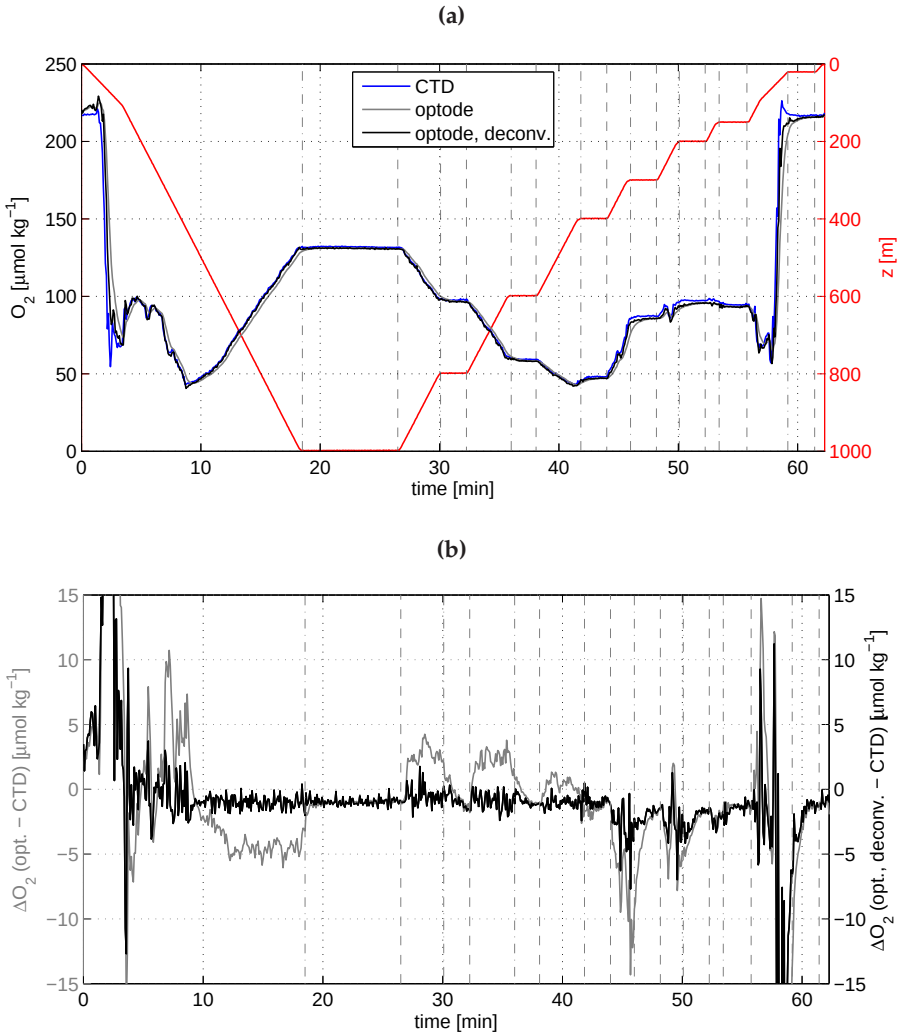

Figure 3.11. (a) Oxygen concentration (left abscissa) as a function of time recorded during a CTD/O_2 cast from a CTD Clark sensor (blue line) and an optode (gray line) attached to the CTD rosette. The deconvoluted optode oxygen profile is shown in black. Red line depicts depth (right abscissa) as a function of time. Several stops with a minimum length of $2\,\mathrm{min}$ were conducted during the upcast for purposes of calibration which is indicated by gray dash-dotted and dashed vertical lines (beginning and end of a stop, respectively). (b) Difference of the optode oxygen profile / deconvoluted optode oxygen profile (gray line / black line) to the CTD oxygen profile from (a). Stops during upcast are again indicated by gray dash-dotted and dashed vertical lines.

[29] A determination of such a temperature dependence from field data is highly uncertain, since cross effects against the time constant or other unknown parameters (e.g calibration coefficients, time shift) can occur during the calibration procedure.

Figure 3.11a shows the oxygen concentration as a function of time recorded during a regular CTD/O_2 cast ($0\,\mathrm{m} - 1000\,\mathrm{m}$) by the CTD Clark sensor and by an optode attached to the CTD rosette. Based on the estimated time constant[30] for this optode, the optode oxygen profile was deconvoluted using (3.12). The difference of the optode oxygen as well as the deconvoluted optode oxygen to the reference CTD oxygen is shown in Figure 3.11b. In general, a large bias is observed in strong oxygen gradients. However, the error of the deconvoluted optode oxygen profile is systematically smaller than the error of the unprocessed optode oxygen profile (as it is obvious between $10\,\mathrm{min}$ and $20\,\mathrm{min}$ or partly between $27\,\mathrm{min}$ and $42\,\mathrm{min}$). For the purpose of calibration, several stops were performed during the upcast of the CTD rosette indicated by the constant depth over time and the dash-dotted and dashed vertical gray lines in Figure 3.11a. During these stops, the optode oxygen sensor equilibrates and both the original and the deconvoluted optode oxygen show an error of comparable magnitude. The amplification of the sensor noise for the deconvoluted optode oxygen profile[31] is within the calibration error which is obvious for time intervals during the calibration stops.

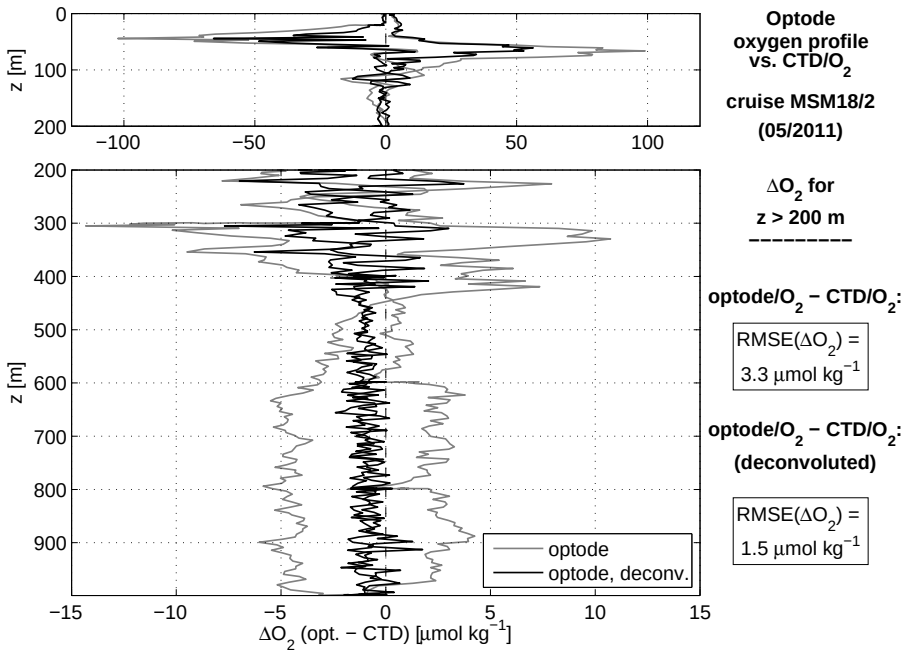

Figure 3.12. Error of the optode oxygen profile during a CTD/O_2 cast as a function of depth. Gray line marks the difference of the optode oxygen to the CTD oxygen. Black line marks the difference of the deconvoluted optode oxygen to the CTD oxygen. Note the different ranges of ΔO_2 for the upper and the lower panel.

The difference of the optode oxygen / deconvoluted optode oxygen to the CTD oxygen as a function of pressure is shown in Figure 3.12. A strong hysteresis of the optode

[30] Here, an average estimate from pre and post deployment calibration cast was used.

[31] Fluctuations on short time scales are amplified with a higher magnitude than fluctuations on long time scales, i.e. the sensor noise (corresponding to white noise) is mostly amplified at time scales of the Nyquist frequency (cf. the characteristics of the transfer function of the deconvolution in Figure B.2).

oxygen profile is observed between downcast and upcast which is reduced for the deconvoluted optode oxygen profile. Due to the high profiling speed of the CTD rosette counting about $1\,\mathrm{m\,s^{-1}}$, a strong error was even observed for the deconvoluted optode oxygen profile predominantly in the upper $100\,\mathrm{m}$, where strong oxygen gradients are present. Here, the root mean square error of the optode oxygen profile / the deconvoluted optode oxygen profile was calculated for depths larger than $200\,\mathrm{m}$. Based on all optodes, the average root mean square error of the optode oxygen profiles between $200\,\mathrm{m}$ and $1000\,\mathrm{m}$ was RMSE$(\Delta O_2) = 3.3\,\mu\mathrm{mol\,kg^{-1}}$, whereas the error of the deconvoluted oxygen profiles was RMSE$(\Delta O_2) = 1.5\,\mu\mathrm{mol\,kg^{-1}}$. In this special case, the deconvolution reduces the error of the oxygen profile between $200\,\mathrm{m}$ - $1000\,\mathrm{m}$ by roughly 50%. Comparison of the average calibration error of the optode ($2.4\,\mu\mathrm{mol\,kg^{-1}}$, see section 3.5) with the average error of the deconvoluted oxygen signal shows that both are in the same order of magnitude. Furthermore, as depicted in Figure 3.12, a slight amplification of fluctuations on short time scales is observed (as defined by the transfer function of the deconvolution, cf. Figure B.2), however, it stays within the range of the calibration error.

The profiling speed of the CTD rosette was generally kept at $1\,\mathrm{m\,s^{-1}}$ which is high compared to other profiling systems such as gliders (about $0.2\,\mathrm{m\,s^{-1}}$) or floats ($0.08\,\mathrm{m\,s^{-1}}$, *Körtzinger et al.* [2005]). Thus, the sensor hysteresis is weaker for the latter two platforms. *Körtzinger et al.* [2005] report that, with respect to floats, this effect is only important for large oxygen gradients of about $1\,\mu\mathrm{mol\,l^{-1}\,m^{-1}}$. Gliders profile with a larger velocity, thus a stronger hysteresis is expected. Despite the lower profiling speed of gliders and floats, a time constant correction will further improve the quality of the optode oxygen data, particularly at depths with strong oxygen gradients that could not be well resolved with the deconvoluted optode oxygen profile during the CTD/O_2 cast.

Within this study, optodes were exclusively applied in moored operations. Sampling times were not shorter than $5\,\mathrm{min}$, so a time constant correction was not applicable for these records. Even if the sampling time had been higher and a time constant correction had been applicable, the calibration stops in Figure 3.11b show that such correction would not have been necessary. An optode during such a calibration stop simulates a moored optode with a high sampling rate ($5\,\mathrm{s}$) and reveals temporal oxygen variability that is far beyond the effect of the time constant.

CHAPTER 4

Oxygen variability in the Tropical Atlantic along 23°W

In the following chapter, the oxygen variability in the Tropical Atlantic along 23°W shall be determined. A meridional section of oxygen variance is derived based on ship section data in section 4.1. Oxygen variability from moored observations is analyzed in section 4.2 and some distinct processes are explained particularly with respect to zonal velocity time series. Section 4.3 compares the previous estimates of oxygen variability from ship section and mooring data at the mooring positions.

4.1 Mean oxygen and oxygen variance along 23°W obtained from ship section data

Based on all single CTD/O_2 profiles that were obtained during research cruises carried out in the Tropical Atlantic along 23°W from 1999 - 2011 (cf. Table A.1), mean and variability of oxygen (and in general: a hydrographic tracer)[32] were calculated between 6°S and 14°N along 23°W with respect to potential density surfaces. The calculation was conducted as follows: Single CTD/O_2 profiles in a zonal range between 22°W and 24°W were assembled to a hydrographic data set as a function of potential density σ_θ and latitude ϕ, where the i^{th} CTD/O_2 profile of a hydrographic tracer C is defined as $C_i = C_i(\sigma_\theta, \phi_i)$. Mean and variance of C were then calculated as weighted variables

[32] Here, only oxygen mean and variability were estimated. Nevertheless, the procedure used here is introduced for a general hydrographic tracer, since in section 5.3 mean and variability of both oxygen and salinity are used to estimate the eddy length scale.

using a two-dimensional Gaussian interpolation scheme[33]:

$$\overline{C}(\sigma_\theta, \phi) = \frac{\sum_i w_i C_i}{\sum_i w_i} \tag{4.1}$$

$$\sigma_C^2(\sigma_\theta, \phi) = \frac{\sum_i w_i (C_i - \overline{C})^2}{\sum_i w_i} \tag{4.2}$$

where $\overline{C}(\sigma_\theta, \phi)$ is the weighted mean and $\sigma_C^2(\sigma_\theta, \phi)$ is the weighted variance. The (Gaussian) weights w_i were determined with the meridional and diapycnal influence (cutoff) radii 0.5° (1.0°) and $\sim 0.01\,\mathrm{kg\,m^{-3}}$ - $0.1\,\mathrm{kg\,m^{-3}}$ ($\sim 0.02\,\mathrm{kg\,m^{-3}}$ - $0.2\,\mathrm{kg\,m^{-3}}$) with maximum diapycnal radii at the surface and minimum at depth. The procedure allowed a determination of mean and variance of C on isopycnal surfaces, i.e. the resulting tracer variability was unaffected by vertical movements of isopycnal surfaces. Obtained fields $\overline{C}(\sigma_\theta, \phi)$ and $\sigma_C^2(\sigma_\theta, \phi)$ were transformed back onto depth coordinates by using the mean depth of the density surfaces $\overline{z}(\sigma_\theta, \phi)$ which was estimated from the mean hydrographic section. This calculation was not performed in the upper $60\,\mathrm{m}$ due to high depth variability of near surface density layers.

Using (4.1) and (4.2), meridional sections of the mean oxygen concentration and the oxygen variance were calculated for the TNEA. Figure 4.1 shows these sections (upper panel: mean oxygen concentration, lower panel: oxygen variance) as a function of latitude (6°S - 14°N) and depth ($60\,\mathrm{m}$ - $1000\,\mathrm{m}$) along 23°W.

The meridional section of the mean oxygen concentration is an update of the section shown in *Brandt et al.* [2010][34]. Evidently, the TNEA OMZ at latitudes north of 5°N spreads between $300\,\mathrm{m}$ and $700\,\mathrm{m}$. Minimum mean oxygen concentrations in the centre of the OMZ are slightly above $40\,\mu\mathrm{mol\,kg^{-1}}$. However, oxygen concentrations below $40\,\mu\mathrm{mol\,kg^{-1}}$ were frequently observed during the last years [*Stramma et al.*, 2009]. South of the TNEA OMZ an equatorial oxygen maximum is present which is generated by strong mean and variable zonal jets (cf. Figure 1.2b). South of the equator, the northern extent of the OMZ in the Tropical South East Atlantic is obvious.

The oxygen variance section in the lower panel of Figure 4.1 shows various maxima indicating strong oxygen variability in the equatorial Atlantic as well as at the boundaries of the OMZ. The southern (5°N - 8°N, $400\,\mathrm{m}$ - $700\,\mathrm{m}$) and the upper boundary (5°N - 12°N, $300\,\mathrm{m}$) of the OMZ are characterized by local oxygen variance maxima. In contrast, the interior of the OMZ shows only weak oxygen variability. Strong oxygen variability was

[33] Strictly speaking, in isopycnal coordinates these would be thickness-weighted means [*De Szoeke and Bennett*, 1993].

[34] Actually, the mean oxygen distribution in *Brandt et al.* [2010] was calculated differently (namely: a direct estimate on depth coordinates was conducted) from the method that was used here. Nevertheless, the comparison of both estimates shows that the mean distribution remains rather unchanged, but note that the mean section estimated here is stronger smoothed in meridional direction due to the larger influence and cutoff radii.

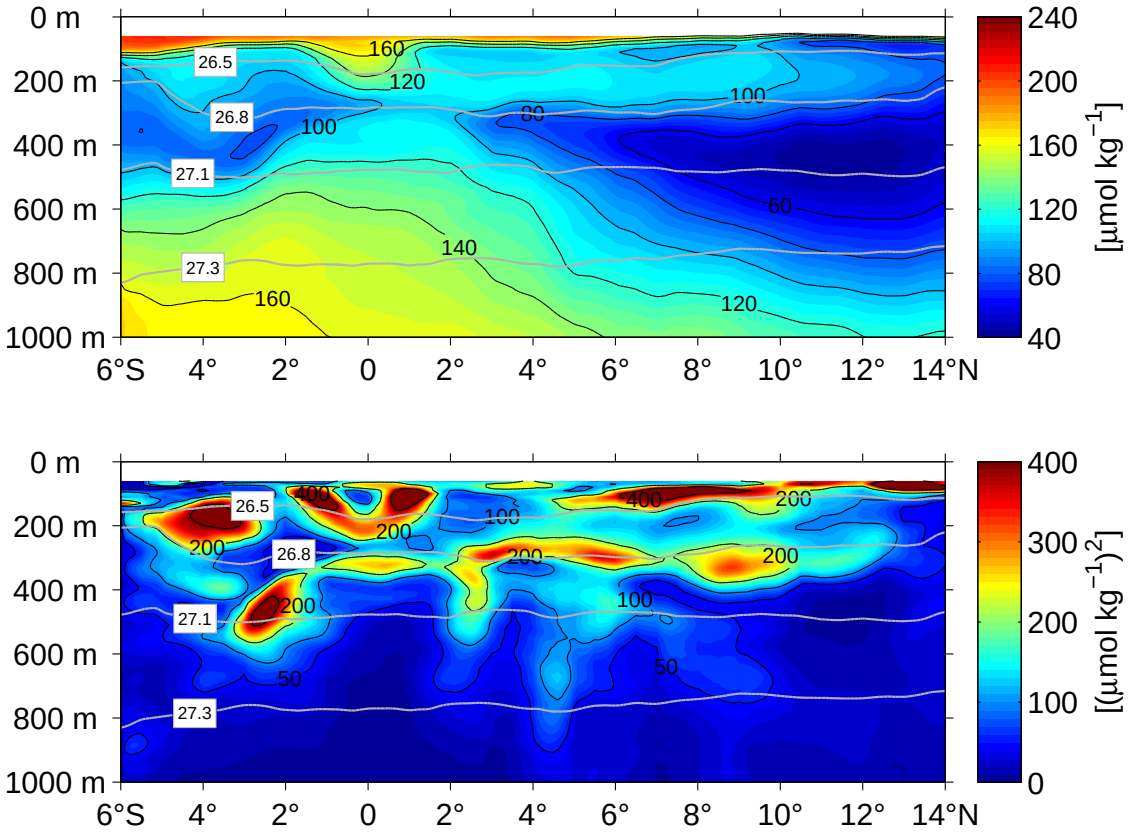

Figure 4.1. (upper panel) Mean oxygen concentration and (lower panel) oxygen variance in the Tropical Atlantic along 23°W (color scale and black contours). Gray contours mark surfaces of constant potential density.

also observed at shallow depths above 200 m over a wide latitudinal range between 4°N and 14°N. Mesoscale eddies, diapycnal mixing as well as zonal current variability are processes that might cause the observed oxygen variability in the Tropical Atlantic.

Due to the large number of CTD/O_2 profiles, the mean and variance sections could be derived at a meridional resolution of 0.5°, so regional differences particularly in oxygen variability are resolved. In contrast, this data set is based on shipboard CTD/O_2 data and thus has a very sparse time resolution. It is a reasonable question, whether the oxygen variance section is a reliable estimate for the oxygen variability in the Tropical Atlantic. Moored observations are capable of closing this gap for specific locations by resolving oxygen fluctuations with a comparatively high resolution.

4.2 Oxygen variability from moored observations

In comparison to shipboard observations, moored observations have a high time resolution and thus provide a reliable estimate of oxygen variability for specific locations. Moored observations in the Tropical Atlantic were carried out along the 23°W meridian at 6 different latitudes between the equator and the core of the OMZ (cf. Table A.2 details). At every mooring position, oxygen was measured at 300 m and 500 m depth (in fact, at 5°N and 8°N, oxygen was recorded overall at 8 different depths between 100 m and 800 m).

The corresponding oxygen time series for 300 m and 500 m are shown in Figure 4.2 and Figure 4.3, respectively. Lowest oxygen concentrations were observed in the interior of the OMZ (i.e. at 8°N and 11.5°N at 500 m depth). For comparison, the long-term mean oxygen concentration (estimated from shipboard observations, cf. mean oxygen section in Figure 4.1) and the average of the oxygen time series are shown as dash-dotted gray and dashed black line, respectively. Both averages agree well at latitudes and depth of the OMZ (5°N and 8°N at 300 m as well as from 5°N to 11.5°N at 500 m), whereas closer to the equator larger differences between both averages are observed. One cause could be longer-term fluctuations that lead to a biased average of the oxygen time series which is particularly obvious at 300 m (equator and 2°N), but also found at 500 m (cf. *Brandt et al.* [2012] as well as Figure 4.4 which is described further down). Further, the limited number of shipboard CTD/O_2 measurements leads to an uncertainty (standard error) of the mean oxygen that is larger in regions with high oxygen variability. A third possible reason concerns the different averages of the mean section and the time series. Whereas the oxygen time series are considered on depth coordinates, the mean oxygen distribution was calculated on density coordinates and consecutively was projected back onto depth coordinates (assuming mean depths of the density surfaces). The effect of the different averaging methods was tested by calculating the mean meridional oxygen distribution once on depth coordinates and once on density coordinates (as given in (4.1)). Both averages agreed well, when comparing them on depth coordinates, and could not explain the observed mismatch between the long-term and the time series average.

The comparison of the time series with respect to depth shows stronger oxygen fluctuations at 300 m than at 500 m depth for all latitudes. North of the equator, the deep oxycline is located roughly at the 300 m isobath (cf. mean meridional oxygen distribution in Figure 4.1). It is likely that a vertical displacement of isopycnal surfaces is responsible for the stronger fluctuations particularly on short time scales at the order of hours to days[35]. The lowest oxygen fluctuations were observed in the interior of the OMZ, particularly at 11.5°N, 500 m, suggesting a weaker ventilation of this regime.

[35] The sampling rate of the optode oxygen sensors was at least 2 h.

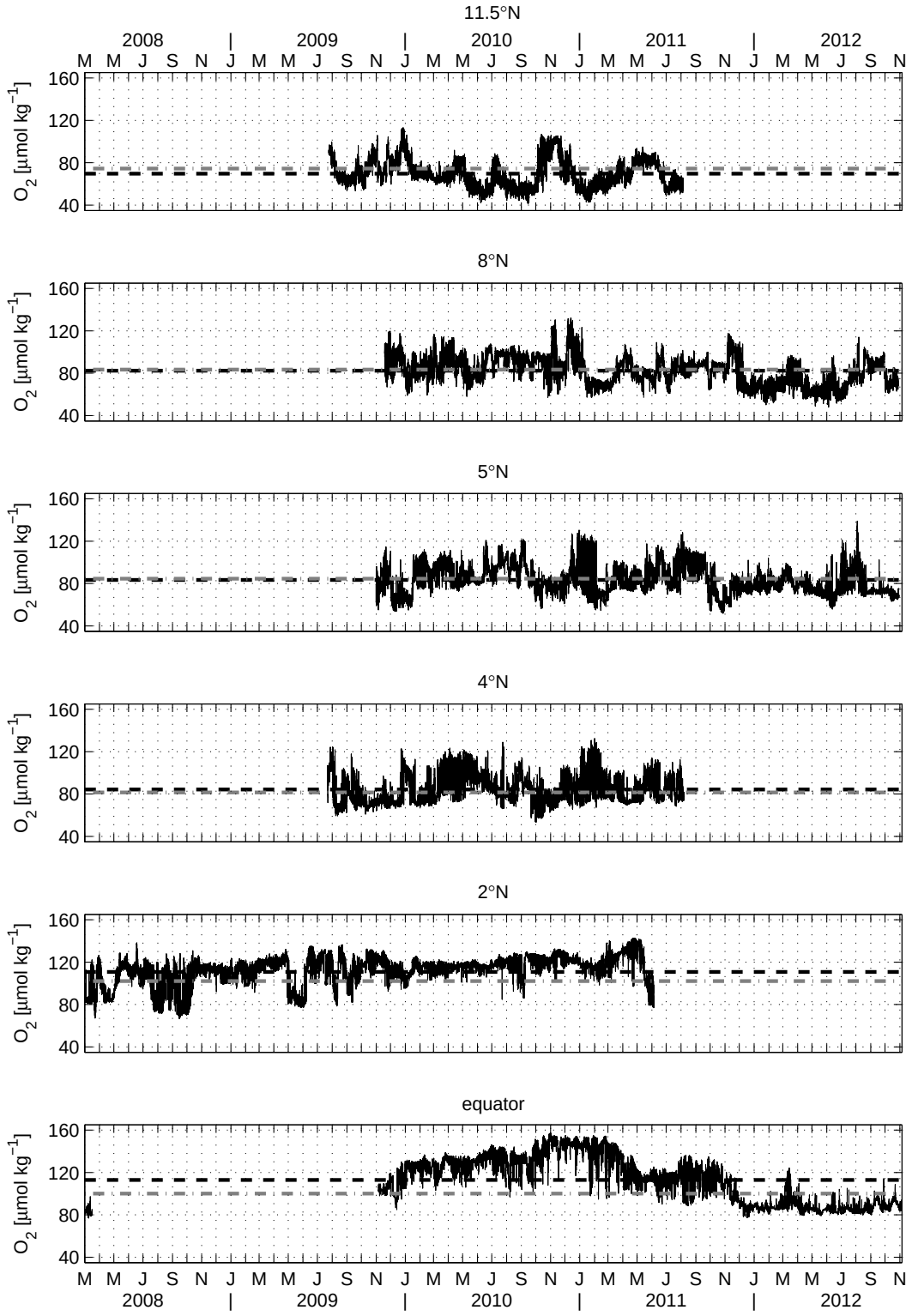

Figure 4.2. Oxygen time series from moored observations along 23°W at 300 m depth. Positions from upper to lower panel are 11.5°N, 8°N, 5°N, 4°N, 2°N and equator. Dash-dotted gray line and dashed black line represent the long-term oxygen mean (shipboard observations) and the average of the mooring time series, respectively.

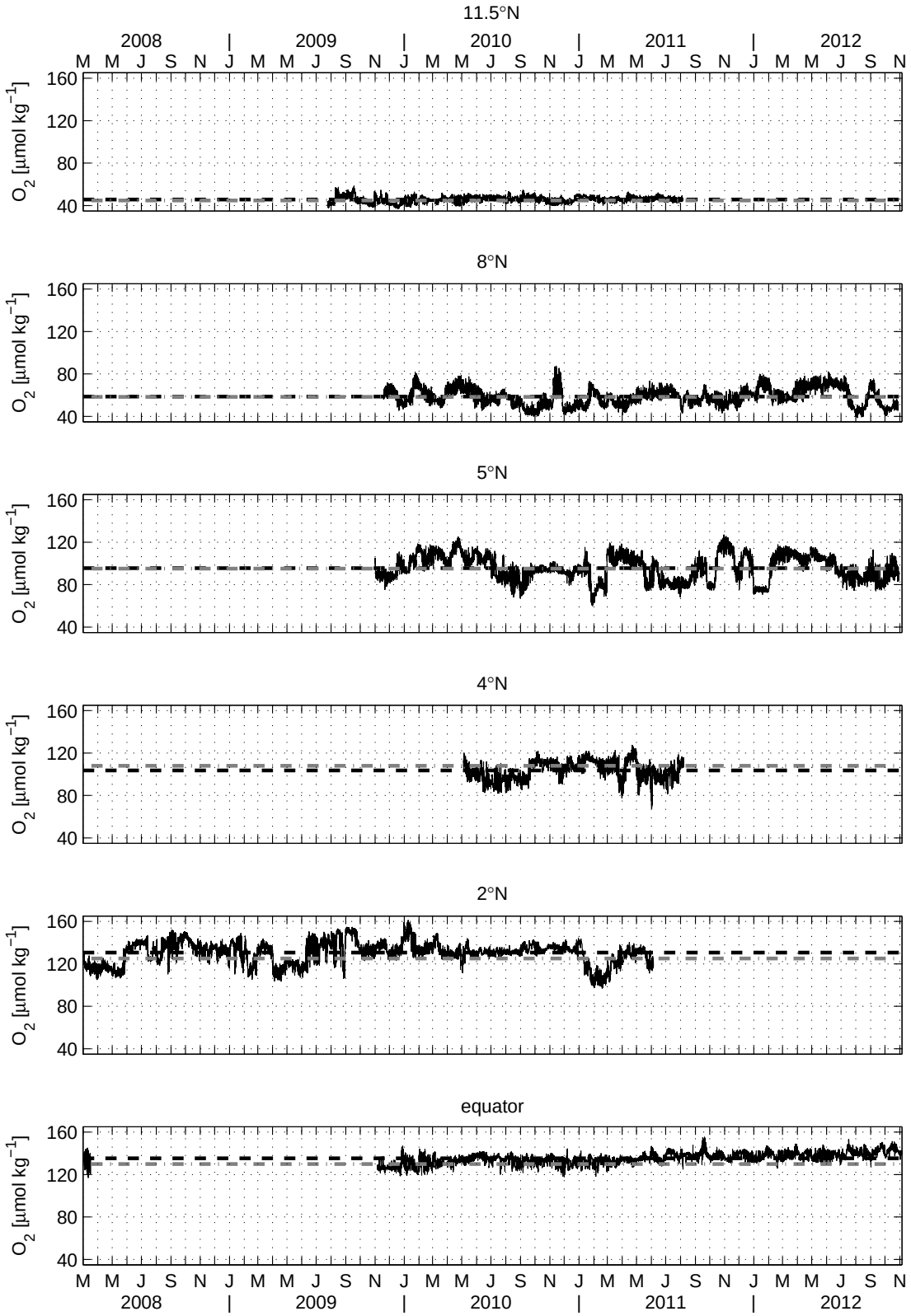

Figure 4.3. Same as Figure 4.2, but at 500 m depth.

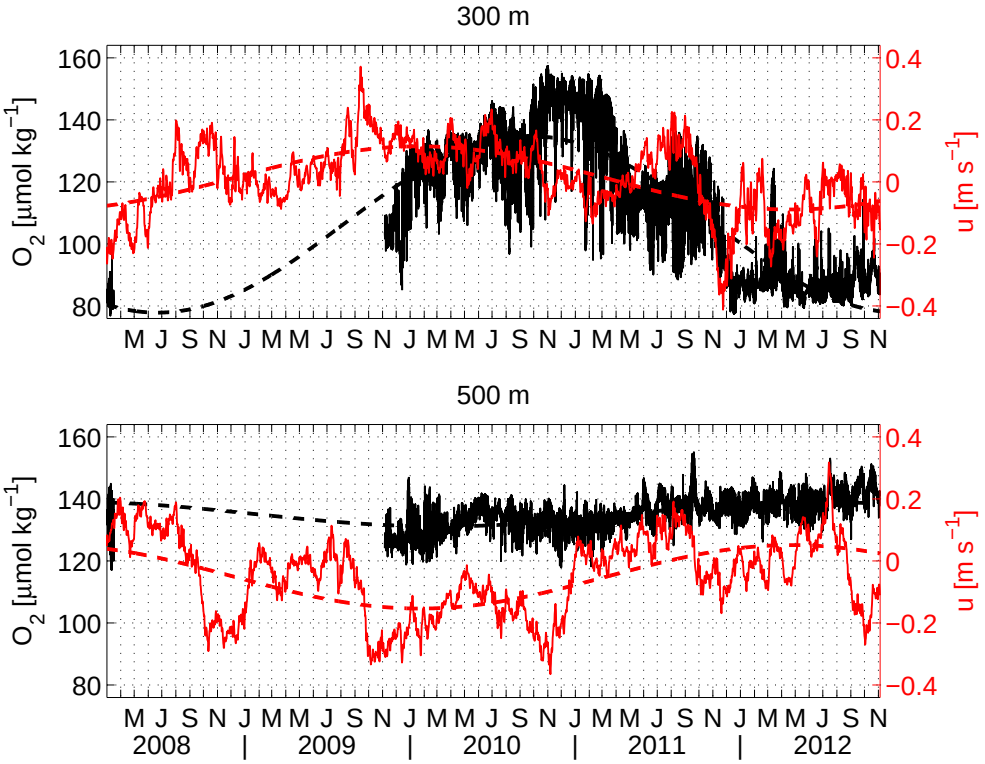

Figure 4.4. Oxygen (black solid line) and zonal velocity (red solid line) time series at the equator, 23°W at $300\,\mathrm{m}$ (upper panel) and $500\,\mathrm{m}$ (lower panel) depth. Note the oxygen time series of 2 weeks length in March 2008. Dashed lines show the harmonic fit to oxygen and zonal velocity, respectively, with a period of $4.5\,\mathrm{yr}$ corresponding to the equatorial deep jet cycle.

The different oxygen time series show oxygen fluctuations on various time scales reaching from dialy, intraseasonal and annual up to interannual variability. Some characteristic signals shall be pointed out in the following.

It was recently described by *Brandt et al.* [2012] that equatorial deep jets cause a strong oxygen variability at the equator on an interannual time scale of $4.5\,\mathrm{yr}$, shown on the basis of both moored observations and an advection-diffusion basin-mode model simulating the equatorial deep jets. An update[36] of the zonal velocity and oxygen time series (moored observations), considered in their study, is shown in Figure 4.4. In particular, the oxygen time series now comprises a full deep jet period[37] for $300\,\mathrm{m}$ and $500\,\mathrm{m}$ depth from Mar. 2008 - Oct. 2012. The velocity amplitude of the deep jets ($4.5\,\mathrm{yr}$ harmonic of the zonal velocity) is of similar magnitude at both depths with about $0.1\,\mathrm{m\,s^{-1}}$, whereas the amplitude of the oxygen fluctuations at the deep jet period is much stronger at $300\,\mathrm{m}$

[36] Extended by the mooring period June 2011 - Oct. 2012 (cf. Table A.2).

[37] The time series of zonal velocity is much longer and starting in 2002 (not shown here for the earlier period). Note the gap of the oxygen time series between mid of March 2008 and Nov. 2009 due to a failure of the optode oxygen loggers after a recording time of two weeks.

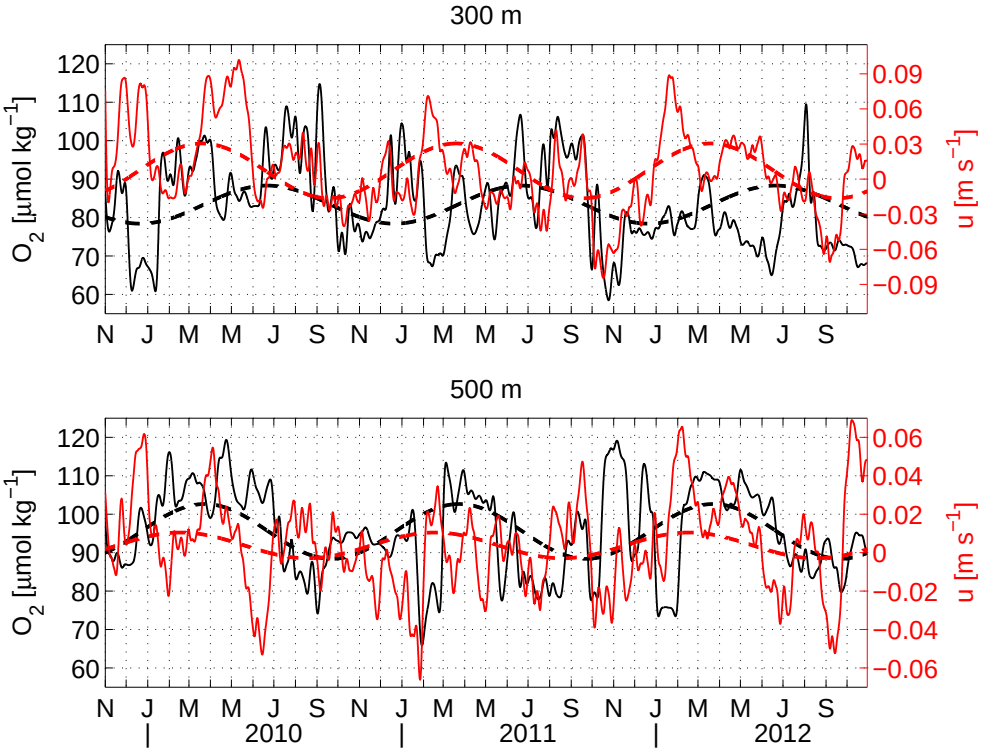

Figure 4.5. Oxygen (black solid line) and zonal velocity (red solid line) time series at 5°N, 23°W at 300 m (upper panel) and 500 m (lower panel) depth. Note that the zonal velocity is differently scaled in the upper and the lower panel. Dashed lines show an annual harmonic fit to oxygen and zonal velocity, respectively.

(about 30 μmol kg^{-1}) than at 500 m (about 5 μmol kg^{-1}) which is basically explained with the stronger zonal oxygen gradient at 300 m. Zonal velocity and oxygen show a phase shift (zonal velocity leading oxygen) of less than quadrature [*Brandt et al.*, 2012] which results in an overall eastward oxygen flux along the equator. Thus, equatorial deep jets supply the equatorial East Atlantic from the well-ventilated western boundary.

Based on the moored observations at 5°N, a second characteristic is described here. Figure 4.5 shows the oxygen (black solid line) and zonal velocity (red solid line) time series at 300 m and 500 m depth for this latitude. Short-term fluctuations were filtered out by applying a low-pass filter[38] with a cutoff period of 10 d. An annual harmonic was fitted to oxygen and zonal velocity, respectively. The observed annual cycle of the zonal velocity is associated with the annual variability of the NECC/NEUC [*Garzoli and Katz*, 1983] which is strongest near the surface with maximum eastward velocities during boral summer, but is still evident at 300 m and 500 m depth with an amplitude of about 0.02 m s^{-1} and less than 0.01 m s^{-1}, respectively. Despite the small magnitude of the annual cycle of the zonal velocity, a clear annual variability of oxygen is observed at these depths contributing by about 20% to the total oxygen variance at depth of the OMZ. A

[38] Here, a butterworth filter of 3^{rd} order was applied.

phase shift between zonal velocity and oxygen was observed (with zonal velocity leading oxygen) which is about 4 months at 300 m and about 2 months at 500 m. Similar characteristics were found for other oxygen and velocity time series at depths between 100 m and 800 m (not shown here).

In addition to the annual cycle, intraseasonal fluctuations on time scales of 1 month - 2 months were observed for the 5°N, 23°W mooring position that correspond to Tropical Instability Waves (TIW) [*Athie and Marin*, 2008]. In particular, strong intraseasonal variability is found for oxygen and meridional velocity (not shown here). A detailed analysis of these fluctuations and their contribution to the meridional oxygen flux into the OMZ is conducted in section 7.3.

The oxygen time series that are shown in Figure 4.2 and Figure 4.3, were recorded at distinct depth levels. Thus, a simple estimate of the oxygen variance from these time series is not comparable to the oxygen variance section in Figure 4.1, since this was evalu-

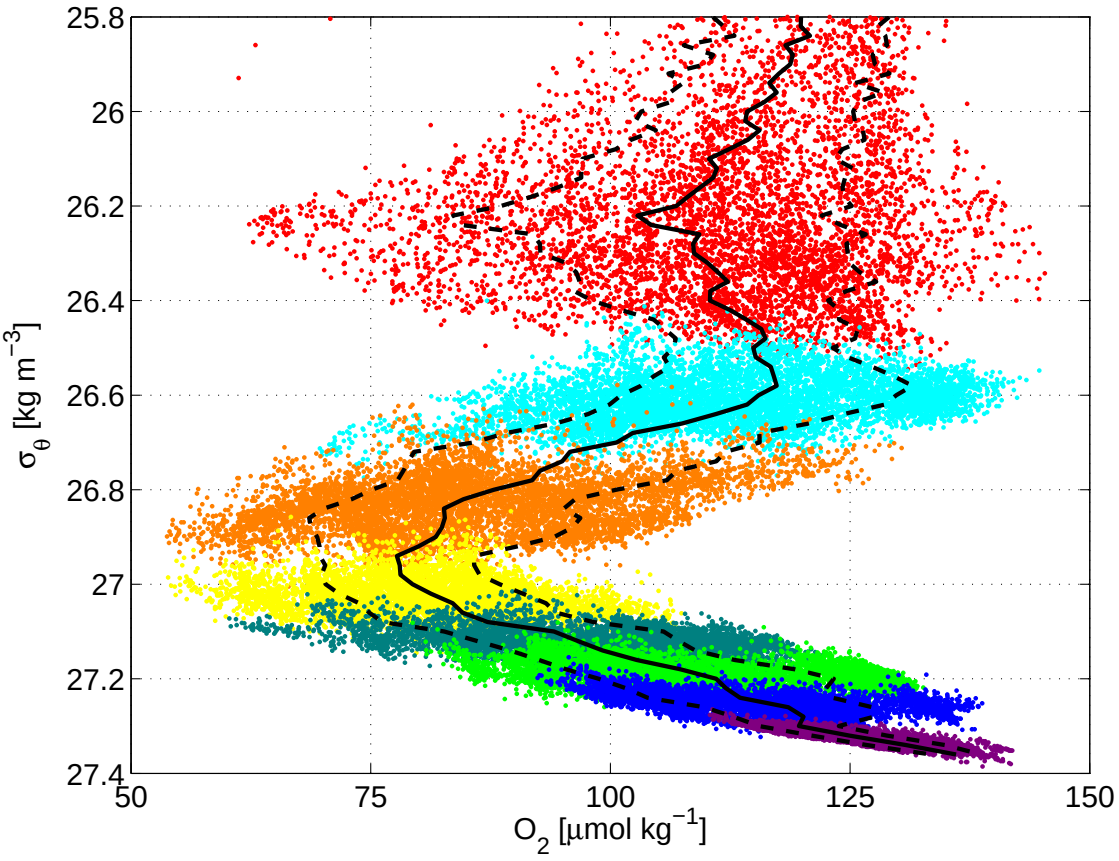

Figure 4.6. Oxygen concentration as a function of potential density as obtained from moored observations at 5°N, 23°W (Nov. 2009 - May 2011). Different colors mark instruments located at different depths between 100 m and 800 m (cf. Table Table A.3 for details). Mean and standard deviation are shown as solid and dashed lines, respectively.

ated on density coordinates. However, in addition to the oxygen time series, both salinity and temperature were recorded at the equator, 2°N, 5°N and 8°N (cf. Table A.3), allowing a consideration of these oxygen time series on potential density coordinates.

As an example, Figure 4.6 shows the oxygen concentration as a function of potential density recorded from the 5°N, 23°W mooring during the period Nov. 2009 - May 2011. Although oxygen was measured on eight distinct depth levels ($\Delta h = 100\,\mathrm{m}$), a quasi-continuous record of oxygen over potential densities from $\sigma_\theta = 26.3\,\mathrm{kg\,m^{-3}}$ to $\sigma_\theta = 27.3\,\mathrm{kg\,m^{-3}}$ was derived due to the vertical displacement of isopycnal surfaces. Mean and standard deviation of oxygen were calculated as a function of potential density and are shown as black solid and dashed lines, respectively. The oxygen minimum at the potential density surface $\sigma_\theta = 27.0\,\mathrm{kg\,m^{-3}}$ is evident. For all four mooring positions (equator, 2°N, 5°N and 8°N), oxygen variance profiles were estimated as a function of potential density and, similar to the 23°W oxygen variance section in Figure 4.1, these profiles were projected back onto depth grid by applying a mean depth for every density surface $\overline{z}(\sigma_\theta, \phi)$. A comparison with the oxygen variance section is done in the following section.

4.3 Comparison of oxygen variance from repeated ship sections and moored observations

In the last two sections, oxygen variance was calculated based on repeat ship sections and moored observations. The oxygen variance section estimated from shipboard observations provides a regional distribution of the oxygen variability. Even though, the reliability of this section needs to be checked due to the sparse time resolution. In contrast, the estimated oxygen variance profiles from the moored observations are based on a high time resolution and thus comprise oxygen variability on various time scales of the order of hours to years. Hence, these profiles are assumed to be a good approximation for the local oxygen variability.

To obtain an estimate of the uncertainty of the oxygen variance map in Figure 4.1, a comparison between profiles derived from shipboard and moored observations is shown in Figure 4.7 for the four mooring positions equator, 2°N, 5°N and 8°N along 23°W. A good correspondence was found for all four latitudes, suggesting that the oxygen variance map can indeed be regarded as a reasonable estimate of the oxygen variability in the Tropical Atlantic along 23°W.

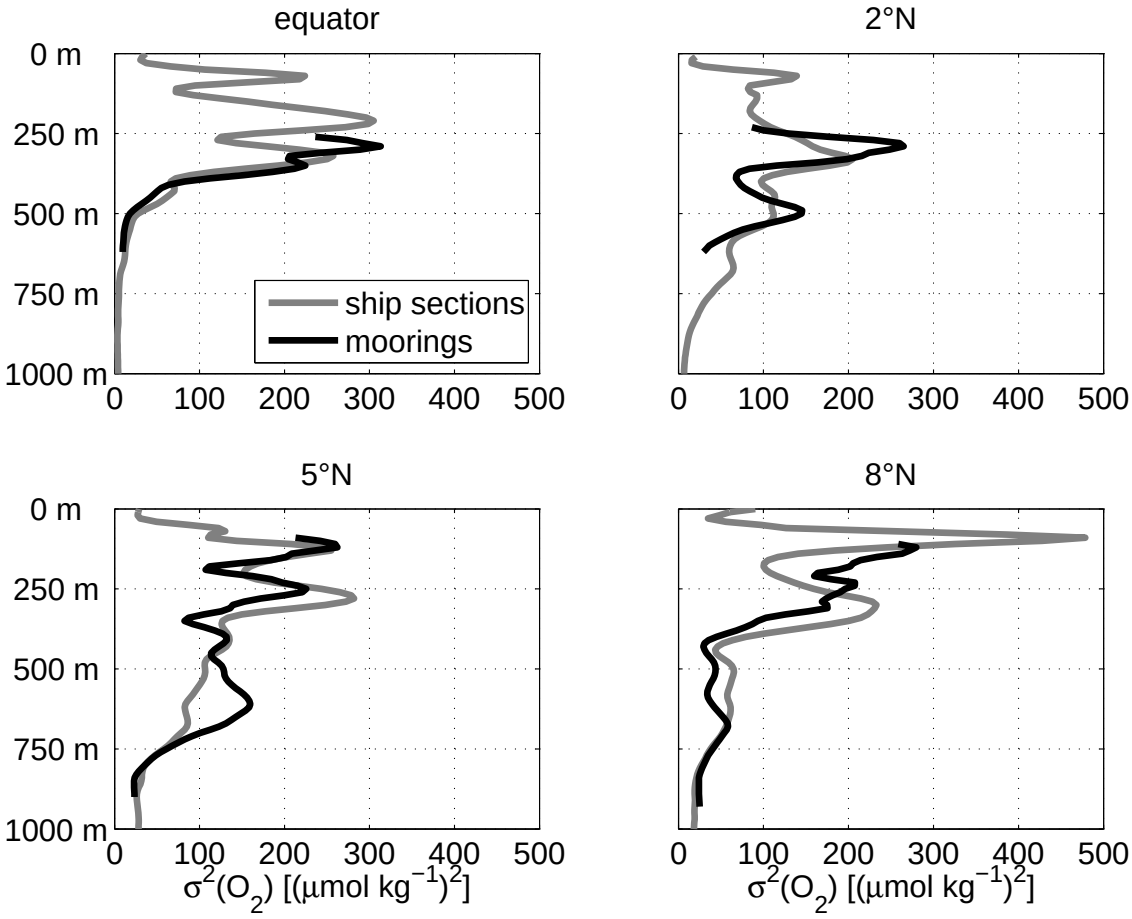

Figure 4.7. Oxygen variance as a function of depth obtained from shipboard (gray line) and moored (black line) observations for the equator, 2°N, 5°N and 8°N along 23°W (cf. Table A.1 and A.3 for details of used data).

CHAPTER 5

Estimate of the eddy diffusivity for the Tropical North East Atlantic

It is of central interest in this study to quantitatively describe the role of mesoscale eddies in (i) the oxygen variability (i.e. the production of oxygen variance using the extended Osborn-Cox relation; chapter 6) and (ii) the meridional ventilation of the TNEA OMZ (chapter 7). As will be shown in these chapters (6 and 7), the analysis is mainly based on a lateral eddy diffusion coefficient[39] in order to parameterize these processes. The determination of a reliable lateral eddy-diffusion coefficient is a long-standing challenge in oceanography and different methods have been applied in various studies to estimate eddy diffusivities from observational [*Ferrari and Polzin*, 2005; *Funk et al.*, 2009] or model data [*Gent and McWilliams*, 1990; *Eden and Greatbatch*, 2009; *Kamenkovich et al.*, 2009]. However, the estimate of the eddy diffusivity is often accompanied by large uncertainties, hence, the estimate of material fluxes using a diffusive flux parameterization has to be considered with care.

In this chapter, a mean eddy diffusivity profile will be derived for the Tropical North East Atlantic based on observational data which is described in detail in order to get some reliability in its estimate. It shall be noted here that the reliability will be further identified in chapter 7 by comparing the estimates of the meridional oxygen flux based on (i) the diffusive flux parameterization and (ii) the flux correlation method.

In general, the eddy diffusivity K_e can be defined proportional to a characteristic eddy velocity U_e and a characteristic eddy length scale $\widetilde{L}$:

$$K_e \sim U_e \widetilde{L} \tag{5.1}$$

[39] In addition, a flux correlation (based on mooring time series) is applied in chapter 7 to estimate the meridional oxygen flux.

In the following section 5.1, the characteristic eddy velocity is determined. In section 5.2, two methods from literature are introduced to estimate the eddy length scale and finally the eddy diffusivity. Eventually, both approaches are combined in section 5.3 to derive a mean eddy diffusivity profile.

5.1 Estimate of the characteristic eddy velocity

The characteristic velocity U_e of mesoscale eddies is defined as the square root of the eddy kinetic energy

$$U_e = \sqrt{\frac{u_e^2 + v_e^2}{2}} \tag{5.2}$$

where u_e and v_e represent the magnitude of zonal and meridional velocity fluctuations according to the mesoscale eddy field. A suitable method to derive these fluctuations is the analysis of mesoscale variability from velocity time series [*Müller and Siedler*, 1992]. Here, velocity time series were used that were recorded during three mooring periods at 5°N, 23°W (cf. Table A.4).

The observed velocity fluctuations contain contributions from the mesoscale eddy field as well as from inertial and tidal variability. By definition, near-inertial and tidal oscillations are not part of the velocity variability on the mesoscale and, hence, have to be excluded in the calculation of u_e and v_e. Near-inertial and tidal oscillations were removed by applying a low-pass filter to the time series, i.e. $\mathcal{L}u = \mathcal{L} * u$ and $\mathcal{L}v = \mathcal{L} * v$ with the low-pass filter operator[40] $\mathcal{L} = \mathcal{L}(1/f_c)$ and the cutoff frequency f_c which was chosen corresponding to a period of $10\,\mathrm{d}$ (the inertial period at 5°N is $T_i = 5.7\,\mathrm{d}$). Eventually, u_e and v_e were calculated as the standard deviation of the low-pass filtered time series ($\sigma_{\mathcal{L}u}$ and $\sigma_{\mathcal{L}v}$).

The estimate of the characteristic eddy velocity U_e from mooring time series as described above is limited to a single mooring position. To determine U_e for a broad latitudinal range, the standard deviations σ_u, σ_v of the 23°W velocity section were used which were derived from repeated ship sections (section 2.1) and are considered as ensemble mean values (cf. *Lilly et al.* [2003]). In contrast to mooring time series, repeated shipboard measurements do not include a similar time resolution to spectrally split these velocity fluctuations in order to obtain the characteristic eddy velocity.

Alternatively, a simple parameterization for the low-pass filter $\mathcal{L}$ is proposed to separate the variability on the mesoscale from short term variability, such as tidal and inertial oscillations. For this purpose, the velocity anomalies of the 5°N, 23°W mooring velocity time series were used. The basic idea is to calculate the magnitude (standard deviation)

[40] Here a butterworth filter of 3^{rd} order was used.

of the velocity fluctuations once with ($\sigma_{\mathcal{L}u} \mathrel{\widehat{=}} u_e$ and $\sigma_{\mathcal{L}v} \mathrel{\widehat{=}} v_e$, representing the mesoscale velocity fluctuations) and once without (σ_u and σ_v, representing the total velocity fluctuations) applying a low-pass filter $\mathcal{L}$, where the cutoff frequency of the low-pass filter is chosen corresponding to a period of 10 d. Then, a polynomial fit of σ_u and σ_v against $\sigma_{\mathcal{L}u}$ and $\sigma_{\mathcal{L}v}$ is applied to parameterize the effect of $\mathcal{L}$, i.e.

$$\begin{aligned} \sigma_{\mathcal{L}u} &= a_0 + a_1\sigma_u + a_2\sigma_u^2 + a_3\sigma_u^3 \\ \sigma_{\mathcal{L}v} &= a_0 + a_1\sigma_v + a_2\sigma_v^2 + a_3\sigma_v^3 \end{aligned} \tag{5.3}$$

The parameterization of the low-pass filter is based on the following assumptions: (i) The magnitude of the low-pass filtered velocity fluctuations ($\sigma_{\mathcal{L}u}$ and $\sigma_{\mathcal{L}v}$) tends to zero, if σ_u and σ_v tend to zero. Thus, $a_0 = 0$. (ii) Without loss of generality, it is assumed that the ratio of inertial and tidal oscillations to the total velocity variability varies with the magnitude of the total velocity variability. Consequently, at least three degrees of freedom are necessary for this parameterization, where a_0 is already defined as 0. Nevertheless, another degree of freedom is added to reduce the residual of the fit.

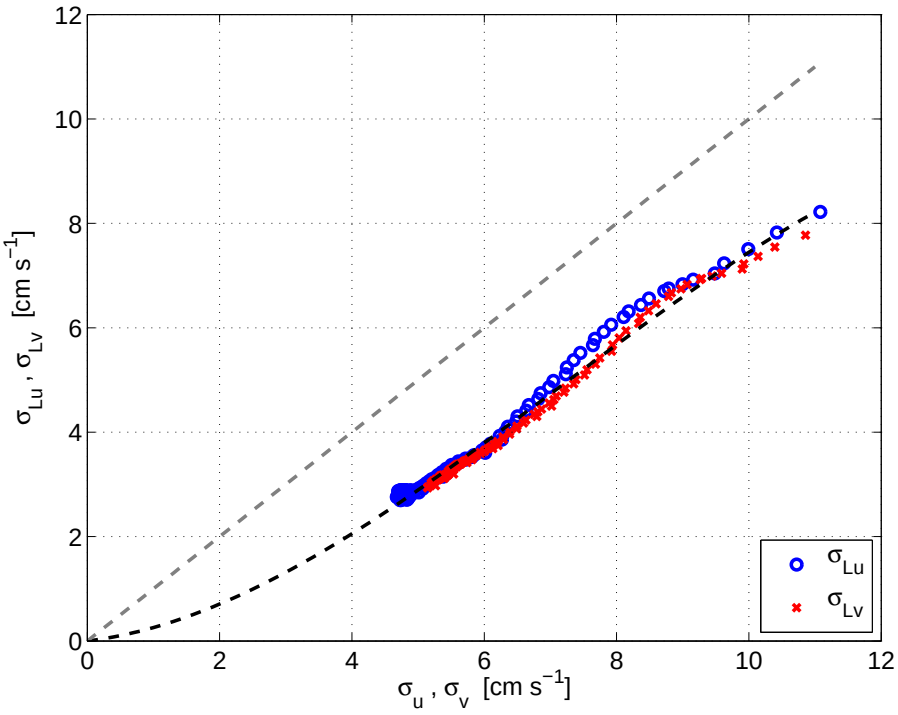

Figure 5.1. Standard deviation of low-pass filtered velocity ($\sigma_{\mathcal{L}u}$, $\sigma_{\mathcal{L}v}$) vs. standard deviation of unfiltered velocity (σ_u, σ_v) obtained from the 5°N, 23°W mooring velocity data. Blue circles and red crosses mark the estimates from the zonal and the meridional component, respectively. The black dashed line is the parameterization function and the gray dashed line marks the bisection line, i.e. $\sigma_{\mathcal{L}u} = \sigma_u$.

The application of the polynomial fit (5.3) on the standard deviation of the 5°N, 23°W mooring velocity time series (data from the depth range between 60 m and 780 m was used, cf. Table A.4 for details) is shown in Figure 5.1. The variability of the filtered

velocities $\sigma_{\mathcal{L}u}$ and $\sigma_{\mathcal{L}v}$ (standard deviation of low-pass filtered velocity) is clearly smaller (by about $2\,\mathrm{cm\,s^{-1}}$) than the variability of the unfiltered velocities σ_u and σ_v. Zonal and meridional velocity variability further occur with an equal magnitude, indicating that velocity variability on the mesoscale is isotropic. The parameterization for the low-pass filter $\mathcal{L}$ (black dashed line) yielded the following values for the polynomial coefficients: $a_1 = 0.15$, $a_2 = 0.11\,(\mathrm{m\,s^{-1}})^{-1}$, $a_3 = -5.2 \cdot 10^{-3}\,(\mathrm{m\,s^{-1}})^{-2}$.

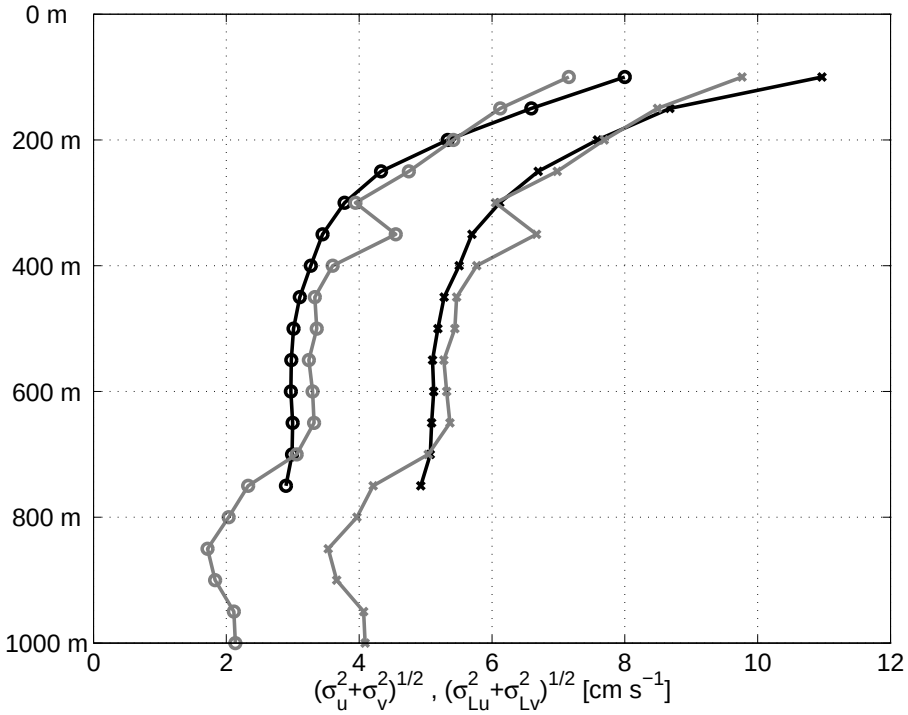

Figure 5.2. Velocity variability as a function of depth at 5°N, 23°W. Black (mooring data) and gray (ship section data) line with crosses mark the calculation using the unfiltered velocity, i.e. $\sqrt{\sigma_u^2 + \sigma_v^2}$. Black (mooring data) and gray (ship section data) line with circles mark the calculation using the low-pass filtered velocity, i.e. $U_e = \sqrt{\sigma_{\mathcal{L}u}^2 + \sigma_{\mathcal{L}v}^2}$, representing the characteristic eddy velocity (see text for details).

Since the above parameterization works well for moderate magnitudes of velocity variability, it was applied to the 23°W velocity section from shipboard observations. For 5°N, the variability from the unfiltered and the filtered velocities (calculated from shipboard and mooring data) using $\sqrt{\sigma_u^2 + \sigma_v^2}$ and $U_e = \sqrt{\sigma_{\mathcal{L}u}^2 + \sigma_{\mathcal{L}v}^2}$, respectively, are shown as a depth profile in Figure 5.2. Whereas the variability of the unfiltered velocities yields about $10\,\mathrm{cm\,s^{-1}}$ - $11\,\mathrm{cm\,s^{-1}}$ at $100\,\mathrm{m}$ and drops down to $5\,\mathrm{cm\,s^{-1}}$ at $700\,\mathrm{m}$, the characteristic eddy velocity U_e is smaller by about $2\,\mathrm{cm\,s^{-1}}$ for almost the entire depth range considered. The U_e profiles from both data sets match well, hence, in the following the corrected 23°W velocity section based on shipboard observations is used to estimate U_e in the whole domain.

The estimated (parameterized) characteristic eddy velocity U_e as well as the absolute

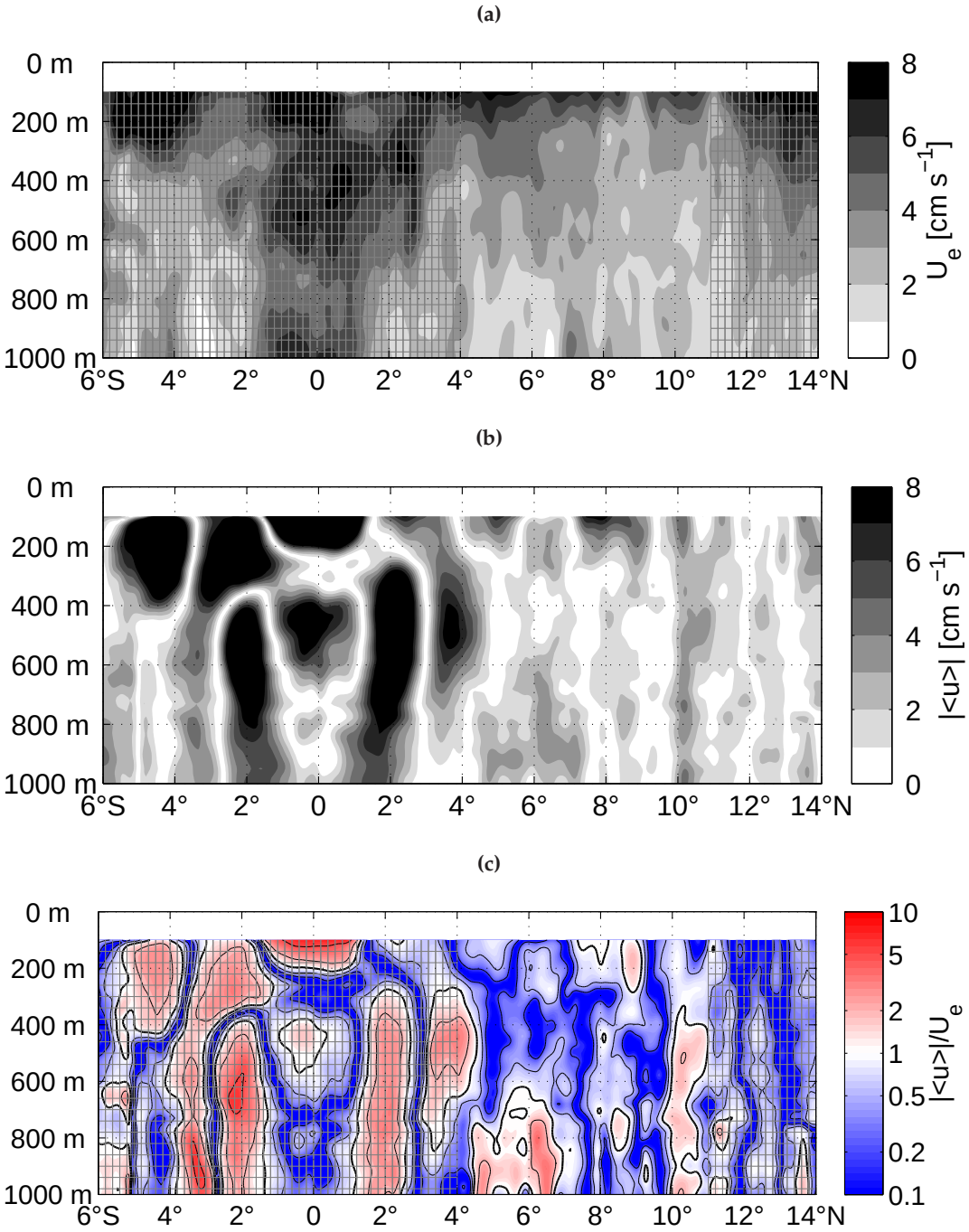

Figure 5.3. (a) Characteristic eddy velocity U_e, (b) absolute mean zonal velocity and (c) ratio of absolute mean zonal velocity over characteristic eddy velocity along 23°W. In (c) thick solid line marks isoline 1, thin solid lines mark isolines 0.2, 0.5 and 2, 5, respectively. Hatched areas in (a) and (c) mark regions, where U_e is uncertain and are therefore not used for further analysis.

mean zonal velocity along 23°W calculated from repeat ship sections are shown in Figure 5.3a and 5.3b, respectively. For the equatorial Atlantic, *Brandt and Eden* [2005], *Brandt et al.* [2006], *Bunge et al.* [2008] and *Brandt et al.* [2012] show that a high percentage of the ve-

locity fluctuations results from intra-seasonal variability (e.g. TIWs), seasonal cycle of the zonal currents as well as variability on interannual time scales leading to an overestimation of U_e which might explain the strong equatorial maximum of U_e in Figure 5.3a between 6°S and 4°N. Enhanced variability was also found between 11°N and 14°N, but it remains unclear whether this is the result of mesoscale or annual to longer-term fluctuations. Hence, for further analysis, the estimated U_e in the regime between 4°N and 11°N was considered.

Figure 5.3c shows the ratio of absolute mean zonal velocity over characteristic eddy velocity. Even though U_e is overestimated between 6°S - 4°N and might be overestimated between 11°N - 14°N, it is evident that the equatorial region is dominated by mean zonal advection, whereas the region from 5°N - 14°N is characterized by a relatively strong mesoscale activity.

5.2 Methodology to estimate the eddy diffusivity

Two different approaches are applied to estimate the eddy diffusivity as a function of depth for the TNEA. The reason for the use of two approaches is that one approach alone is not capable of estimating the eddy diffusivity for the depth range of $100\,\mathrm{m}$ - $1000\,\mathrm{m}$ as it will be discussed below and in the results in section 5.3.

The first parameterization is based on the mixing length theory and was already used in *Ferrari and Polzin* [2005]. The eddy diffusivity is given by

$$K_e^{(1)} = c_e U_e L_e \tag{5.4}$$

L_e is the mixing length and defines the distance that a fluid particle can move on an isopycnal surface before interchanging its properties with the surrounding fluid. From observations the mixing length can be estimated as

$$L_e = \frac{\sigma_C}{|\nabla_\sigma C_m|} \tag{5.5}$$

where σ_C represents the local tracer fluctuation on the isopycnal surface σ_θ with the mean tracer gradient $\nabla_\sigma C_m$. The tracer fluctuations σ_C are estimated from the square root of the tracer variance as obtained from (4.2). The absolute value of the mean isopycnal oxygen gradient is calculated by the modulus of the mean zonal and the mean meridional isopycnal gradient as follows

$$|\nabla_\sigma C_m| = \sqrt{(\nabla_{\sigma x} C_m)^2 + (\nabla_{\sigma y} C_m)^2} \tag{5.6}$$

$\nabla_{\sigma y} C_m$ is determined using the mean hydrographic 23°W section calculated by (4.1). Since no hydrographic information in the zonal direction can be obtained from the mostly

meridionally aligned measurements, the mean zonal isopycnal oxygen gradient $\nabla_{\sigma x} C_m$ is calculated from the hydrographic mean fields (temperature, salinity, oxygen) of the World Ocean Atlas 2009.

U_e is the characteristic velocity of the mesoscale as calculated in the previous section 5.1 and c_e is an efficiency factor that describes the mixing efficiency of mesoscale turbulence. Here, for the mixing efficiency the same value is applied ($c_e = 0.16$) as used by *Ferrari and Polzin* [2005], who refer to an observational study by *Wunsch* [1999]. It is considered as an average global value for the mixing efficiency of mesoscale eddies.

For calculating the mixing length L_e in (5.5), it has to be assumed that almost all tracer fluctuations on an isopycnal surface are generated by mesoscale turbulence - diapycnal mixing has to be negligible[41]. That's why the mixing length can only be estimated for locations with a strong mean isopycnal and a weak mean diapycnal tracer gradient. Otherwise, a contribution of diapycnal mixing to the tracer variance would result in an overestimation of L_e. To estimate its validity, L_e is determined based on two independent tracers: salinity and oxygen. That is, mixing lengths L_e^S (from salinity) and L_e^O (from oxygen) are calculated and compared to each other. The mixing length L_e is proposed to be properly determined in regions with a large mean isopycnal tracer gradient and conditions $L_e^S \approx L_e^O$ being valid over length scales much larger than the mixing length itself. Regions, where the estimated mixing length L_e is trustworthy, are discussed in the results in section 5.3.

The second parameterization is as in *Eden and Greatbatch* [2008], where the eddy diffusivity is given by

$$K_e^{(2)} \sim U_e L_R \tag{5.7}$$

Again, U_e is the characteristic velocity from the previous section 5.1. L_R is the Rhines scale which is a better approximation for the eddy length scale in the Tropical and Subtropical Atlantic ($< 30°$N) than the local Rossby radius [*Eden*, 2007]. In *Eden* [2007] the Rhines scale is defined by

$$L_R = \sqrt{\frac{U_e}{2\beta}} \tag{5.8}$$

The Rhines scales characterizes the length scale of two-dimensional mesoscale turbulence on a β-plane. For the Tropical and Subtropical Atlantic, *Eden* [2007] and *Eden and Greatbatch* [2009] show an anisotropy of the eddy length scale and the eddy diffusivity. This anisotropy exists due to the fact that mesoscale eddies lead to time mean currents in

[41] Here, it is referred to the two variance generating processes (mesoscale stirring and diapycnal mixing) described in the extended Osborn-Cox model which is introduced in section 6.1 and is expressed by (6.1). In general, both mesoscale stirring and diapycnal mixing are capable of generating oxygen variability on an isopycnal surface.

the zonal direction, whereas in the meridional direction they have a purely diffusive character [*Kamenkovich et al.*, 2009]. From the analysis of shipboard and moored observations (cf. chapter 2 as well as Table A.1 and A.3), an almost isotropic distribution of zonal and meridional velocity variability on the mesoscale was found (cf. Figure 5.1 in section 5.1). It is assumed that this estimate of the eddy diffusivity represents the diffusive character of the eddy field without any parameterization of eddy-driven mean zonal jets. Combining (5.7) and (5.8) yields proportionality between eddy diffusivity and characteristic eddy velocity to the power of 3/2 with a weak latitudinal dependence due to β:

$$K_e^{(2)} \sim \sqrt{\frac{U_e^3}{2\beta}} \tag{5.9}$$

Eden [2007] notes that no uniform definition of the Rhines scale exists (cf. also *Eden and Greatbatch* [2008]). This mainly results from the definition of the characteristic velocity which could be defined either by barotropic, first baroclinic mode or local velocity fluctuations[42]. Thus, a constant scaling factor α is introduced (which still has to be determined):

$$K_e^{(2)} = \alpha\sqrt{\frac{U_e^3}{2\beta}} \tag{5.10}$$

The two parameterizations (5.4) and (5.10) have the following restrictions. Regarding $K_e^{(2)}$, the scaling factor α needs to be determined. $K_e^{(1)}$ can only be determined for regions with a well-defined mixing length L_e, i.e. where a strong mean isopycnal tracer gradient exists. Once a reasonable $K_e = K_e^{(1)}$ is estimated for such region, $K_e^{(2)}$ can be fitted to $K_e^{(1)}$ to determine the constant scaling factor α which finally allows an estimation of K_e independent from L_e. Both parameterizations are a function of the characteristic eddy velocity U_e. Hence, the estimation of K_e depends on the validity of U_e which was discussed in section 5.1.

In summary, the approach to determine the eddy diffusivity is the following: (i) Estimate the mixing length L_e with (5.5) by using two different tracers (salinity and oxygen) and find regions, where L_e is well-determined. (ii) calculate $K_e^{(1)}$ with (5.4) for these regions. (iii) Find the scaling factor α by fitting $K_e^{(2)}$ from (5.10) to the estimated $K_e^{(1)}$. (iv) Use (5.10) to calculate K_e as a function of depth and latitude. (v) Find a mean K_e profile for the Tropical North East Atlantic.

5.3 Eddy diffusivity for the Tropical North East Atlantic

In this section, the five steps as described in the end of the previous section 5.2 are conducted to estimate the eddy diffusivity. The results are described in the following.

[42] Within this study, U_e was estimated based on the local velocity fluctuations as given by (5.2).

(i) The eddy length scale L_e was estimated by applying (5.5) for salinity and oxygen from shipboard CTD/O_2 sections. By comparing the results of the mixing lengths L_e^S and L_e^O, the robustness of the calculation was investigated. Figure 5.4 shows the eddy length scale as a function of latitude and depth averaged over both mixing lengths L_e^S and L_e^O, i.e. $L_e = (L_e^S + L_e^O)/2$. A good correspondence of both mixing lengths was found for

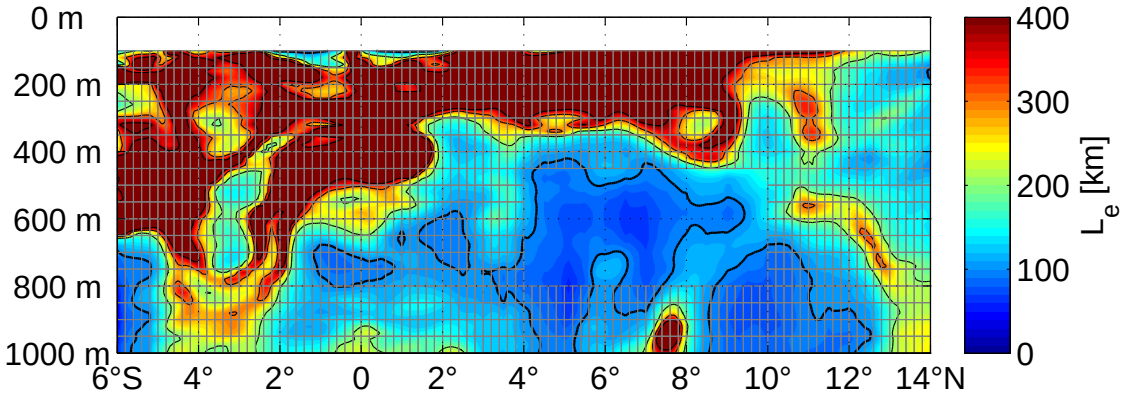

Figure 5.4. Estimate of the eddy length scale L_e in the Tropical Atlantic along 23°W based on shipboard observations using (5.5). Thick black lines mark the $100\,\mathrm{km}$ isoline of the eddy length scale. Thin lines mark isolines $200\,\mathrm{km}$, $300\,\mathrm{km}$ and $400\,\mathrm{km}$. Hatched areas define a highly uncertain estimate of the eddy length scale and are not used for further calculations. A robust estimate for L_e is given in the latitudinal range 4°N - 10°N and for a depth range of $450\,\mathrm{m}$ - $800\,\mathrm{m}$.

the latitudes 4°N - 10°N and for a depth range of $450\,\mathrm{m}$ - $800\,\mathrm{m}$ with an average eddy length scale of about $L_e = 100\,\mathrm{km}$. This region is characterized by strong (meridional) gradients in both salinity (transition zone from South Atlantic Central/Intermediate Water to North Atlantic Central/Intermediate Water) and oxygen (transition zone from the well-ventilated equatorial region to the core of the TNEA OMZ).

(ii) Using (5.4), the eddy diffusivity $K_e^{(1)}$ was determined based on both the eddy length scale L_e as estimated in (i) and the characteristic eddy velocity U_e (section 5.1). Restricted by L_e and U_e, a reasonable estimate for $K_e^{(1)}$ was found in the latitudinal range 4°N - 10°N and for the depth range $450\,\mathrm{m}$ - $800\,\mathrm{m}$. According to *Ferrari and Polzin* [2005], the error for $K_e^{(1)}$ was assumed with a factor of 2, i.e. $[0.5K_e^{(1)}, 2K_e^{(1)}]$.

(iii, iv) The scaling factor α in (5.10) was determined by fitting $\sqrt{U_e^3/2\beta}$ to the eddy diffusivity $K_e^{(1)}$ for the latitudes 4°N - 6°N in the depth range $450\,\mathrm{m}$ - $800\,\mathrm{m}$ and $\alpha = 0.59$ was found. Then, $K_e^{(2)}$ was calculated between 4°N - 11°N (meridionally restricted again by U_e) and covering a depth range from $100\,\mathrm{m}$ - $1000\,\mathrm{m}$.

(v) As for $K_e^{(1)}$, the uncertainty of $K_e^{(2)}$ was assumed with a factor of 2. This means, the meridional variability of $K_e^{(2)}$ between 4°N and 11°N is smaller than its uncertainty. Hence, one mean eddy diffusivity profile $K_e(z)$ as a function of depth was determined

for the TNEA by averaging $K_e^{(2)}$ between 4°N and 11°N.

The estimated eddy diffusivity profile $K_e(z)$ for the TNEA is shown in Figure 5.5. It reaches values of about $1350\,\mathrm{m^2\,s^{-1}}$ at $100\,\mathrm{m}$ depth and exponentially decays to values below $300\,\mathrm{m^2\,s^{-1}}$ at $800\,\mathrm{m}$ - $1000\,\mathrm{m}$ depth which is in principle a function of the characteristic eddy velocity. For comparing reasons, it is also shown the meridional eddy diffusivity at $300\,\mathrm{m}$ depth estimated from the Guinea Upwelling Tracer Release Experiment (carried out at 8°N, 23°W) in a study by *Banyte et al.* (*'Lateral diffusivity from tracer release experiments in the tropical north Atlantic thermocline'*, submitted to Journal of Geophysical Research, 2012, henceforth: *Banyte et al.* [2013], *subm.*). They estimate a meridional eddy diffusivity of $400\,\mathrm{m^2\,s^{-1}}$ ($\pm 200\,\mathrm{m^2\,s^{-1}}$) for the TNEA at $300\,\mathrm{m}$ depth. Both estimates are in good agreement with each other. Additionally, the eddy diffusivity profile estimated from the NATRE experiment at 26°N, 29°W [*Ferrari and Polzin*, 2005] is included. It is larger at depths from $200\,\mathrm{m}$ - $700\,\mathrm{m}$ and drops down to a similar magnitude at depths from $800\,\mathrm{m}$ - $1000\,\mathrm{m}$.

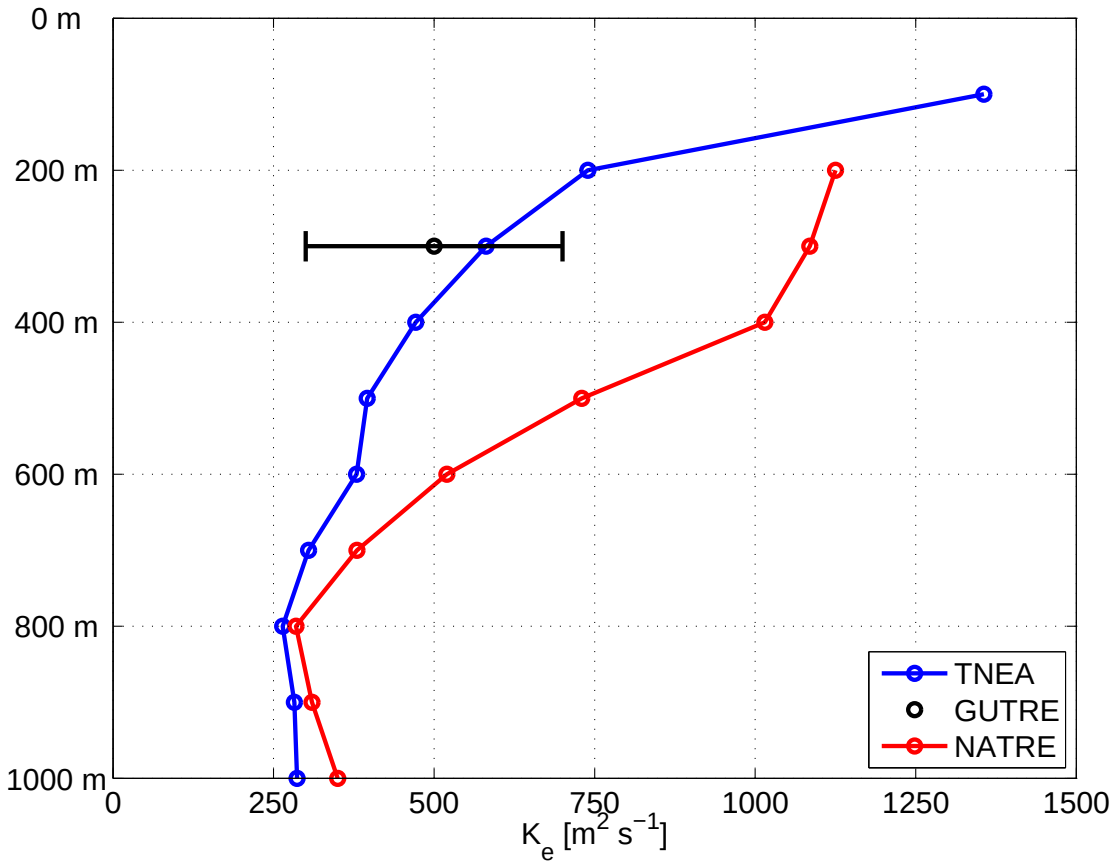

Figure 5.5. Mean depth profile of the eddy diffusivity. Blue line marks the estimate for the Tropical North East Atlantic (TNEA) from this study (4°N - 11°N, 23°W) with an assumed error of factor 2. Black dot with error bar marks the eddy diffusivity from the Guinea Upwelling Tracer Release Experiment (GUTRE) at 8°N, 23°W [*Banyte et al.* [2013], *subm.*] and the red line marks the eddy diffusivity from the North Atlantic Tracer Release Experiment (NATRE) at 26°N, 29°W [*Ferrari and Polzin*, 2005].

In the following chapters, the obtained eddy diffusivity profile $K_e(z)$ is applied to estimate the oxygen variance production caused by mesoscale stirring (chapter 6) as well as the eddy-driven meridional oxygen flux and supply (chapter 7) along the 23°W section. The whole section from 6°S - 14°N will be considered to show also qualitative differences between the equatorial region and the OMZ. Strictly speaking, these estimates are valid only in the latitude range from 4°N - 11°N.

CHAPTER 6

Diagnosis of the oxygen variance production based on the extended Osborn-Cox model

The estimate of the oxygen variance along the 23°W section (Figure 4.1) has revealed regimes with enhanced oxygen variability. In this chapter, the local maxima of oxygen variability, particularly at the boundaries of the OMZ, shall be understood using the extended Osborn-Cox relation. Section 6.1 introduces the methodology which is applied in section 6.2.

6.1 The extended Osborn-Cox model

The basic approach to analyze tracer variability (be it temperature, salinity or oxygen) is the Reynolds decomposition. For the case of temperature, *Osborn and Cox* [1972] found a simple relation between the generation and dissipation of tracer variance known as the Osborn-Cox model. However, *Ferrari and Polzin* [2005] elucidate that mesoscale dynamics are not considered as an individual process within the Reynolds decomposition and the standard Osborn-Cox relation, and applied a triple decomposition[43] $C = C_m + C_e + C_t$, where C_m, C_e and C_t are defined as the tracer mean[44], the tracer fluctuation on the mesoscale and the tracer fluctuation on the microscale, respectively. Within their study, they derive a parameterized tracer variance budget (extended Osborn-Cox model) for the steady and homogeneous state relating variance generating processes (left hand side) to

[43] Despite the fact that oxygen is a non-conservative tracer, it is applied here in the triple decomposition, since time scales of local oxygen change due to generation or consumption are much larger than time scales and magnitude of oxygen variability due to physical processes.

[44] Strictly speaking, this should be a thickness-weighted average in isopycnal coordinates.

the dissipation of tracer variance (right hand side), namely

$$\underbrace{K_e \left|\nabla_\sigma C_m\right|^2}_{[1]} + \underbrace{K_\rho \left(\nabla_\rho^\perp C_m\right)^2}_{[2]} = \underbrace{\frac{1}{2}\kappa_C \langle |\nabla C_t|^2 \rangle}_{[3]} \tag{6.1}$$

with eddy diffusivity K_e, mean isopycnal tracer gradient $\nabla_\sigma C_m$, diapycnal diffusivity K_ρ, mean diapycnal tracer gradient $\nabla_\rho^\perp C_m$ and molecular diffusivity κ_C of the tracer C. The terms in (6.1) can be summarized in a schematic which was originally proposed by *Garrett* [2001] and further discussed by *Ferrari and Polzin* [2005]. Term $[1]$ represents the generation of tracer variance by the mesoscale, i.e. mesoscale eddies act on a mean isopycnal tracer gradient and generate variability on the fine- to mesoscale $(O(0.1-100)\,\mathrm{km})$[45]. Term $[2]$ describes the generation of tracer variance on the microscale, i.e. diapycnal mixing acts on the mean diapycnal tracer gradient and generates variance on the microscale $(O(10^{-3}-1)\,\mathrm{m})$. Term [3] represents the dissipation of tracer variance on the molecular scale.

When deriving the extended Osborn-Cox model, *Ferrari and Polzin* [2005] hypothesized that the variance exchange between different scales of motion (triple products)[46] is negligible. They prove their hypothesis by showing that no large discrepancy in the temperature variance budget exists when applying the extended Osborn-Cox model for the Mediterranean outflow regime in the North Atlantic. However, here it shall be mentioned that the neglect of these divergent terms is strengthened by numerical studies [*Eden et al.*, 2007, 2009] which show that the original Osborn-Cox relation still holds for regions with strong advective fluxes of tracer variance, since these fluxes are compensated to a large extent by rotational eddy fluxes.

Within this study, (6.1) is used to estimate the generation of oxygen variance by mesoscale stirring $[1]$ and diapycnal mixing $[2]$ as a function of density and latitude. Although a proof of the oxygen variance budget is not possible since no appropriate measurements with a fast response oxygen sensor were available to estimate the oxygen variance dissipation, the role of these two generation processes in the TNEA can be compared.

To estimate [1], the absolute value of the mean isopycnal tracer gradient $|\nabla_\sigma C_m|$ is calculated according to (5.6). The depth profile of the eddy diffusivity K_e for the TNEA was estimated in section 5.3 and is applied here for the whole 23°W section.

To calculate [2], the mean diapycnal oxygen gradient is derived from the mean hydrographic section along 23°W as given in (4.1), i.e. $C_m \mathrel{\widehat{=}} \bar{C}$. The diapycnal diffusivity K_ρ was determined from microstructure measurements by *Fischer et al.* [2012], who propose a constant profile over a depth range of $150\,\mathrm{m}$ and $500\,\mathrm{m}$ for the TNEA with $K_\rho = 1.0 \cdot$

[45] For a mechanistic description of this process, see *Smith and Ferrari* [2009].
[46] Compare also the full tracer variance equation in *Ferrari and Polzin* [2005].

$10^{-5}\,\mathrm{m^2\,s^{-1}}$. This value is in good agreement with the value of $(1.19 \pm 0.18) \cdot 10^{-5}\,\mathrm{m^2\,s^{-1}}$ as obtained from a tracer release experiment carried out at 8°N, 23°W at $350\,\mathrm{m}$ depth [*Banyte et al.*, 2012]. To estimate the variance production by diapycnal mixing for a density range that is associated with a depth range of $100\,\mathrm{m}$ to $1000\,\mathrm{m}$, K_ρ was extrapolated by assuming a constant diapycnal diffusivity.

6.2 Oxygen variance production by mesoscale stirring and diapycnal mixing

In this section, the oxygen variance production due to mesoscale stirring and diapycnal mixing as defined in the extended Osborn-Cox relation ([1] and [2] in (6.1)) is estimated. The following variables were used: the eddy diffusivity profile from section 5.3, the constant diapycnal diffusivity profile estimated by *Fischer et al.* [2012], the hydrographic section along 23°W estimated in section 4.1 based on (4.1) as well as the hydrographic distribution of the World Ocean Atlas 2009 (cf. section 2.3).

All variables were computed on density surfaces and projected back onto depth coordinates afterward by using the mean depth of the density surfaces $\overline{z}(\sigma_\theta, \phi)$. The oxygen variance production due to mesoscale stirring and diapycnal mixing is shown as color shaded contours in Figure 6.1a and 6.1b, respectively. Both terms describe the generation of oxygen variance $(\mu mol\ kg^{-1})^2$ within the time period of one year. The mean oxygen distribution is superimposed as black contour lines.

The sum of both terms reflects the total oxygen variance production and is shown in Figure 6.1c. Regarding the regime of the OMZ, evidently high oxygen variance production occurrs at the southern boundary (5°N - 8°N, $400\,\mathrm{m}$ - $700\,\mathrm{m}$) and the upper boundary (5°N - 12°N, $300\,\mathrm{m}$) of the OMZ, whereas the interior of the OMZ shows little oxygen variance production.

To evaluate the contribution of either process to the total oxygen variance production, the ratio of both terms can be calculated, i.e.

$$R = \frac{K_e \left|\nabla_\sigma O_{2m}\right|^2}{K_\rho \left(\nabla_\sigma^\perp O_{2m}\right)^2} \tag{6.2}$$

The result is shown in Figure 6.1d. For $R \gg 1$, mesoscale stirring along isopycnal surfaces mainly generates the oxygen variance, whereas in case of $R \ll 1$ diapycnal mixing is the larger variance production term. $R \sim 1$ indicates that both processes contribute to the variance production in the same order of magnitude. Regimes with a total oxygen variance production of less than $50\,(\mu\mathrm{mol\,kg^{-1}})^2\,\mathrm{yr^{-1}}$ are marked gray in the figure. It was found that oxygen variance at the southern boundary of the OMZ (5°N - 8°N, $400\,\mathrm{m}$ -

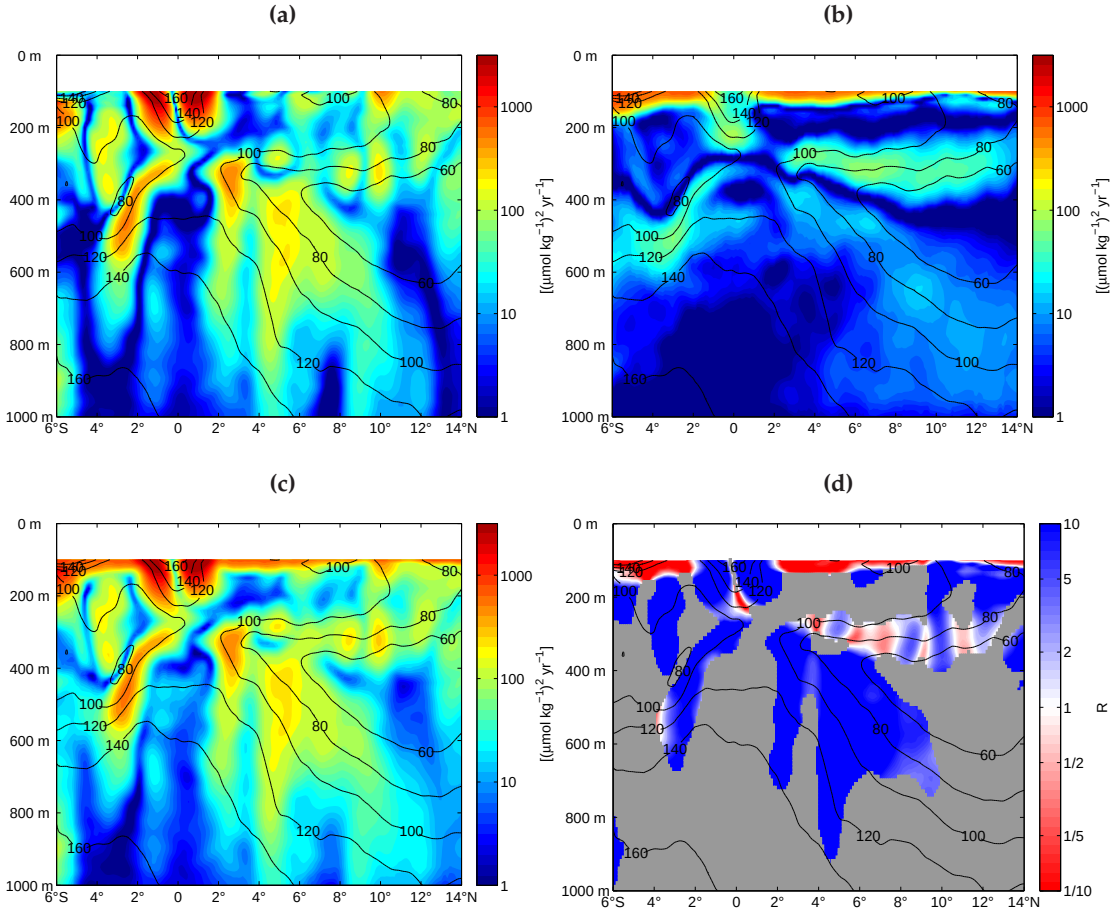

Figure 6.1. 23°W sections (6°S - 14°N) of (a) O_2 variance production by mesoscale stirring, (b) O_2 variance production by diapycnal mixing, (c) total O_2 variance production due to mesoscale stirring and diapycnal mixing (sum of (a) and (b)) and (d) ratio R of O_2 variance production terms (mesoscale stirring over diapycnal mixing). Gray areas in (d) define regions with a total O_2 variance production of less than $50\,(\mu\mathrm{mol\,kg^{-1}})^2\,\mathrm{yr^{-1}}$. In all four panels, the mean oxygen distribution is superimposed as black contour lines.

700 m) is dominantly produced by mesoscale stirring. The oxygen variance at the upper boundary of the OMZ (5°N - 12°N, 300 m) is generated by both mesoscale stirring and diapycnal mixing.

CHAPTER 7

Eddy-driven meridional oxygen flux and oxygen supply along 23°W

A point of main research in this study is the determination of the meridional ventilation of the TNEA OMZ due to mesoscale eddies. Based on repeat ship sections and moored observations (cf. Table A.1, Table A.3 and Table A.4), two different methods are applied in this chapter to derive the eddy-driven meridional oxygen flux along 23°W: (i) a diffusive flux parameterization using both the estimated mean profile of the eddy diffusivity (section 5.3) and the mean meridional oxygen distribution (Figure 4.1) to estimate a meridional section of the meridional oxygen flux, and (ii) a correlation of oxygen and meridional velocity time series acquired from the 5°N, 23°W and 8°N, 23°W moorings to determine local oxygen fluxes. The results of both methods are compared to identify the reliability of these estimates. In addition, this comparison implicitely gives information about the uncertainty of the estimated eddy diffusivity profile from chapter 5.

Time scales of mesoscale activity at low latitudes are found to be of the order of a month (e.g. TIWs have time scales of 25 d - 50 d [*Athie and Marin*, 2008]). Here, oxygen and meridional velocity time series from moored observations are used to determine time scales of oxygen and velocity fluctuations as well as time scales of the meridional oxygen flux.

The derived 23°W section of the eddy-driven meridional oxygen flux will be further used to determine the meridional oxygen supply due to mesoscale eddies that sheds light on regimes of meridional oxygen flux divergence (loss of oxygen) and convergence (gain of oxygen). Eventually, these results are compared with recent estimates of oxygen consumption, diapycnal oxygen supply and the oxygen trend to refine the oxygen budget in the TNEA OMZ.

Section 7.1 describes the methods used to realize the above goals. In section 7.2, the eddy-driven meridional oxygen flux is derived. Time scales of oxygen, meridional velocity and the meridional oxygen flux are estimated in section 7.3. The eddy-driven meridional oxygen supply is calculated in section 7.4 and its results are used in section 7.5 to develop a refined picture of the oxygen budget in the TNEA OMZ.

7.1 Methodology to estimate the meridional oxygen flux and oxygen supply

7.1.1 Parameterization of the meridional oxygen flux

The parameterization of the eddy-driven meridional oxygen flux can be expressed as a diffusive flux along a density surface, since a fluid particle does no work against gravity when moving along a neutral density surface [*McDougall*, 1987][47]. It is

$$F_d(\sigma_\theta, \phi) = -K_e(\sigma_\theta)\nabla_{\sigma y}\overline{O_2}(\sigma_\theta, \phi) \tag{7.1}$$

Here, K_e is the mean eddy diffusivity profile for the TNEA. In section 5.3, K_e was determined as a function of depth. For the application in (7.1), it is transformed onto density coordinates by using the mean depth of the density surfaces $\overline{z}(\sigma_\theta, \phi)$ estimated from the mean hydrographic section. $\nabla_{\sigma y}\overline{O_2}$ is the mean meridional oxygen gradient along an isopycnal surface - the mean oxygen, $\overline{O_2}$, is calculated according to (4.1). A constant thickness of an isopycnal layer with respect to latitude is assumed here because the depth of the potential density surfaces is rather constant over latitude (cf. Figure 4.1), i.e. a thickness weighting of the mean oxygen distribution $\overline{O_2}$ is neglected in (7.1).

7.1.2 Meridional oxygen flux from time series correlation

The second method to determine the meridional oxygen flux is given by the correlation of meridional velocity and oxygen time series. The total meridional oxygen flux at a given position is defined as

$$\mathcal{F}(\sigma_\theta) = \overline{vO_2} \tag{7.2}$$

where the overbar denotes the temporal average of $v(\sigma_\theta, t)O_2(\sigma_\theta, t)$ on a density surface over the recorded time series.

[47] Neutral density surfaces are defined locally, but do not necessarily exist continuously. Here, the calculations are based on surfaces of potential density referred to the ocean surface.

The Reynolds decomposition is used to separate the time series v and O_2 into a mean $\overline{(\cdot)}$ and an anomaly $(\cdot)'$ on surfaces of potential density, i.e.

$$v(\sigma_\theta, t) = \overline{v}(\sigma_\theta) + v'(\sigma_\theta, t) \tag{7.3}$$

$$O_2(\sigma_\theta, t) = \overline{O_2}(\sigma_\theta) + O_2'(\sigma_\theta, t) \tag{7.4}$$

where $\overline{v'} = \overline{O_2'} = 0$. Combining (7.2) - (7.4), the flux on a density surface is then given by

$$\mathcal{F}(\sigma_\theta) = \underbrace{\overline{v}(\sigma_\theta)\overline{O_2}(\sigma_\theta)}_{\overline{\mathcal{F}}(\sigma_\theta)} + \underbrace{\overline{v'(\sigma_\theta, t)O_2'(\sigma_\theta, t)}}_{\mathcal{F}'(\sigma_\theta)} \tag{7.5}$$

with the mean isopycnal oxygen flux $\overline{\mathcal{F}}(\sigma_\theta)$ and the turbulent isopycnal oxygen flux $\mathcal{F}'(\sigma_\theta)$. The mean oxygen flux is highly uncertain (not shown), since the relative error of the meridional velocity $\Delta v/\overline{v}$ is large[48]. The mean oxygen flux due to a zonal mean flow was studied using a simple advection diffusion model in *Brandt et al.* [2010] and will not be considered here. The main goal is the estimation of the eddy-driven oxygen flux and therefore the concentration is on term $\mathcal{F}'(\sigma_\theta)$.

Oxygen time series were recorded on distinct depth levels z_I (cf. Table A.3). Due to the variability of density surfaces, (7.4) leads to gappy oxygen time series for a single density surface which can cause large uncertainties for the results of (7.5). Alternatively, the turbulent lateral oxygen flux at the instrument depth z_I can be defined via a weighted average over density surfaces which is given by

$$F'(z_I) = \frac{\sum_{i=1}^{S} n_i \mathcal{F}'(\sigma_{\theta i})}{\sum_{i=1}^{S} n_i} \tag{7.6}$$

where n_i is the number of data points that were measured on the i^{th} density surface during the mooring period and $\sum_{i=1}^{S} n_i = N$ is the total number of data points of the time series. The time average in (7.5) is defined by $\overline{(\cdot)} = \sum_j^n (\cdot)/n$ and (7.6) transforms to

$$\begin{aligned} F'(z_I) &= \frac{\sum_{i=1}^{S} n_i \left(\frac{1}{n_i} \sum_{j=1}^{n_i} v_j'(\sigma_{\theta i}) O_{2j}'(\sigma_{\theta i}) \right)}{\sum_{i=1}^{S} n_i} \\ &= \frac{\sum_{i=1}^{S} \sum_{j=1}^{n_i} v_j'(\sigma_{\theta i}) O_{2j}'(\sigma_{\theta i})}{\sum_{i=1}^{S} n_i} \end{aligned} \tag{7.7}$$

The double summation over indices i and j is basically a sum over the whole time series and can be written as

$$F'(z_I) = \frac{\sum_{k=1}^{N} v_k' O_{2k}'}{N} \tag{7.8}$$

[48] Based on repeat shipboard ADCP sections and moored ADCPs, the absolute value of the mean meridional velocity at 5°N, 23°W and 8°N, 23°W was estimated to $< 1\,\mathrm{cm\,s^{-1}}$. The measurement error (cf. section 2.1) is of the same order of magnitude ($< 2\,\mathrm{cm\,s^{-1}}$).

with v'_k and O'_{2k} being the velocity and oxygen anomalies of the recorded time series at the instrument depth z_I. $F'(z_I)$ is interpreted as the turbulent meridional oxygen flux at the instrument depth z_I which is the weighted average over all isopycnal surfaces that were sampled by the instrument during the mooring period. The error for the turbulent meridional oxygen flux is estimated as the standard error of an arithmetic mean value, i.e.

$$\Delta F'(z_I) = \frac{F'(z_I)}{\sqrt{n_f}} \tag{7.9}$$

where n_f represents the degrees of freedom of the time series. n_f is estimated from the autocorrelation function of the velocity time series as follows: The number m of correlated data points in the time series is calculated by testing the autocorrelation function of the meridional velocity against 0-coherence on a 95% confidence level while assuming the statistics of a t-distribution for the correlation coefficient. Then, the degrees of freedom are computed with the total number of data points N divided by the number of correlated data points m

$$n_f = \frac{N}{m} \tag{7.10}$$

At 5°N, 23°W and 8°N, 23°W, meridional velocity and oxygen were recorded simultaneously during the periods Nov. 2009 - Oct. 2012 and May 2011 - Oct. 2012, respectively (cf. Table A.3 and A.4), hence (7.8) is applicable. In general, (7.8) contains a divergent and rotational flux component. However, the rotational flux component does not contribute to the mean tracer budget at all. From a single mooring location, it is impossible to estimate the pure divergent tracer flux that contributes to the mean tracer budget. Nevertheless, *Marshall and Shutts* [1981] and *Eden et al.* [2007] show that rotational fluxes are coupled to the strength of the divergence of the flux of variance which in turn is related to the mean current field. This provides a justification for the assumption that rotational fluxes are rather small in regions with a weak mean flow.

At the mooring positions 5°N, 23°W and 8°N, 23°W, weak mean currents are found at depth (e.g. cf. Figure 4.5 or Figure 5.3) and a weak contribution of rotational fluxes to the flux estimates in (7.8) is assumed. The largest bias due to rotational fluxes is expected at shallow depths (100 m and 200 m), since a stronger mean flow exists due to the NECC/NEUC and the nNECC current band at 5°N and 8°N, respectively.

Since the eddy-driven meridional oxygen flux is of main interest, the velocity and oxygen variability on time scales of the inertial period and shorter was excluded by low-pass filtering[49] the time series anomalies v' and O'_2 with a cutoff frequency corresponding to a period of 10 d (the inertial period is $T_i = 5.7$ d and $T_i = 3.6$ d at 5°N and 8°N, respectively).

[49] Here, a butterworth filter of 3^{rd} order was used.

The high temporal resolution of the oxygen and velocity time series from the 5°N, 23°W and 8°N, 23°W moorings allows a spectral analysis of these data sets. Apart from Fourier spectra that are calculated from velocity and oxygen time series, a spectral analysis of the turbulent meridional oxygen flux $F'(z_I)$ is performed. For this purpose, a low-pass filter[50] $\mathcal{L}(\tau)$ with different cutoff periods τ is applied on the time series anomalies, i.e.

$$\begin{aligned} \mathcal{L}_\tau v' &= \mathcal{L}(\tau) * v' \\ \mathcal{L}_\tau O_2' &= \mathcal{L}(\tau) * O_2' \end{aligned} \tag{7.11}$$

Then, the oxygen flux can be calculated as a function of the filter period τ:

$$\mathcal{L}_\tau F'(z_I) = \overline{\mathcal{L}_\tau v' \mathcal{L}_\tau O_2'} \tag{7.12}$$

$\mathcal{L}_\tau F'(z_I)$ can be interpreted as the cumulative oxygen flux resulting from processes on time scales between the filter period τ and the total length of the time series T_{max}.

7.1.3 Parameterization of the meridional oxygen supply

Based on the parameterized eddy-driven meridional oxygen flux (7.1), the eddy-driven meridional supply of oxygen is estimated. Meridional loss or gain of oxygen due to eddy diffusion is given by the meridional divergence of the oxygen flux on an isopycnal surface which is the meridional derivative $-\nabla_{\sigma y} F_d$. Using the diffusive flux parameterization (7.1), the meridional oxygen supply along 23°W is then given by

$$-\nabla_{\sigma y} F_d(\sigma_\theta, \phi) = K_e(\sigma_\theta) \nabla^2_{\sigma y} \overline{O_2}(\sigma_\theta, \phi) \tag{7.13}$$

7.2 Eddy-driven meridional oxygen flux

The eddy-driven meridional oxygen flux along the 23°W section was calculated on potential density surfaces using the flux gradient parameterization (7.1) and was projected back onto depth coordinates afterward. The result is shown in Figure 7.1 which basically reflects the mean meridional oxygen gradient. Reddish/bluish colors define a northward/southward eddy-driven oxygen flux, respectively. Black contour lines represent oxygen isolines in interval steps of $20\,\mu\mathrm{mol\,kg^{-1}}$. Between the southern boundary and the interior of the OMZ (in a depth range $400\,\mathrm{m}$ - $700\,\mathrm{m}$), a northward oxygen flux is found which continuously decreases from 5°N towards north, drops to zero at the core

[50] Here, a running mean was applied with a rectangular filter window, where the window length was defined as the cutoff period. The reason for using a running mean instead of a butterworth filter is that a zero oxygen flux for large filter periods could be ensured (due to weak edge effects of the filter) which has to be given by definition (since time series anomalies were used for the correlation).

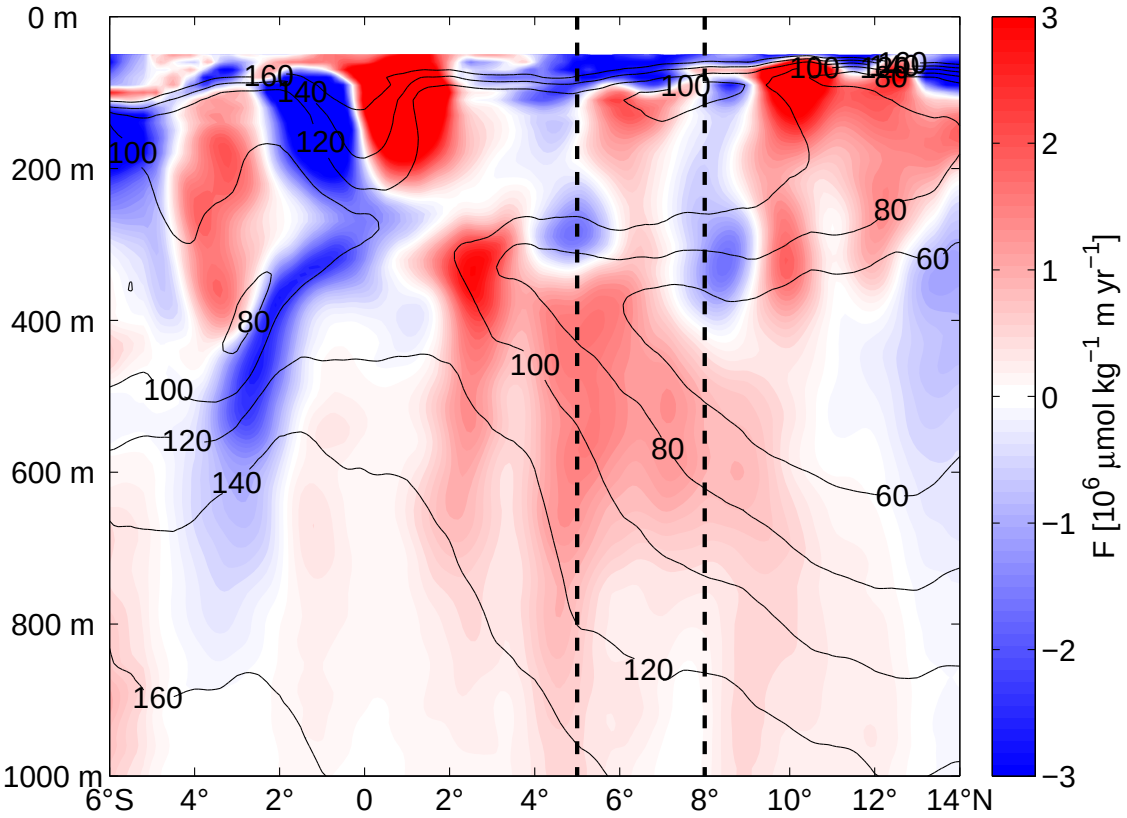

Figure 7.1. Eddy-driven meridional oxygen flux along 23°W calculated using the diffusive flux parameterization (7.1). Positive/negative values mark an eddy-driven oxygen flux directed toward north/south. Superimposed black contour lines mark the mean oxygen distribution. Dashed vertical lines mark the mooring positions 5°N, 23°W and 8°N, 23°W that are considered in Figure 7.2a and Figure 7.2b.

of the OMZ (11°N) and turns into a southward flux north of 11°N. Between 100 m and 400 m, meridionally alternating bands of north- and southward oxygen flux are dominant. Near the equator, mainly poleward directed oxygen fluxes are found.

Based on the 5°N, 23°W and 8°N, 23°W mooring data, the eddy-driven meridional oxygen flux and its error was calculated via correlation using (7.8) and (7.9) after having low-pass filtered the time series anomalies to remove inertial and tidal variability.

Figure 7.2a and Figure 7.2b show the comparison of both flux calculations (parameterization and correlation) at 5°N, 23°W and 8°N, 23°W, respectively. For 5°N, 23°W, both estimates match well within the error at depths from 100 m - 500 m. Nevertheless, at depths of 100 m and 200 m, the stronger meridional oxygen flux calculated from the mooring data as well as its estimated error reflect a high variability of oxygen flux which decreases at depths between 300 m - 500 m. In a depth range of 600 m - 800 m, the correlation method generally shows a smaller and southward directed oxygen flux, whereas the parameterized flux is stronger and directed toward north. For 8°N, 23°W, both flux

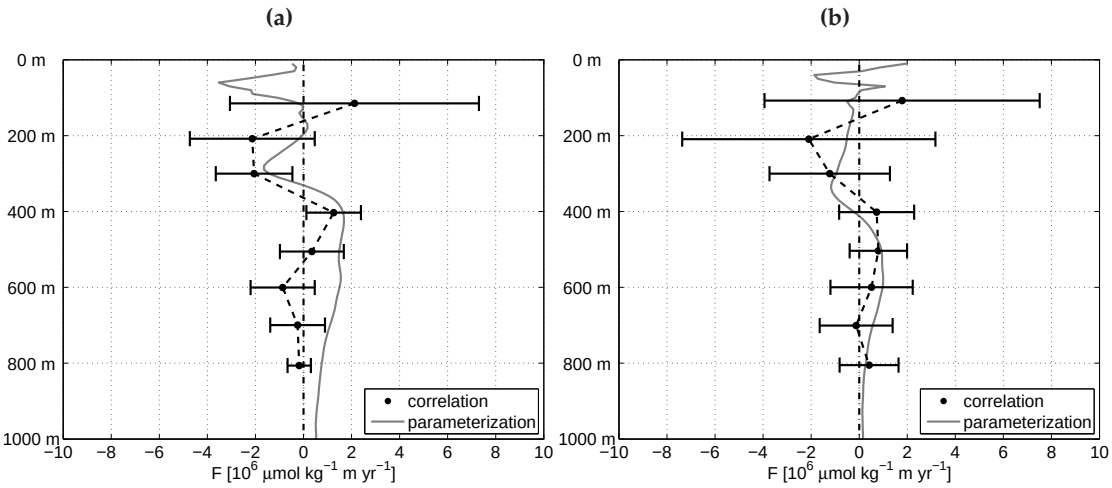

Figure 7.2. (a) Eddy-driven meridional oxygen flux at 5°N, 23°W calculated via correlation of low-pass filtered mooring time series (black dots) with error bars and via diffusive flux parameterization (gray line) as it is shown in Figure 7.1. For the correlation, the meridional velocity and oxygen time series were low-pass filtered with a cutoff frequency corresponding to a period of $10\,\mathrm{d}$. (b) same as (a), but for 8°N, 23°W.

estimates are in good agreement within the error at almost all depths between $100\,\mathrm{m}$ and $800\,\mathrm{m}$. Similar to 5°N, 23°W, a high variability of the oxygen flux is found at $100\,\mathrm{m}$ and $200\,\mathrm{m}$ depth. The southward oxygen flux between $100\,\mathrm{m}$ - $300\,\mathrm{m}$ as well as the northward oxygen flux at depths from $400\,\mathrm{m}$ - $800\,\mathrm{m}$ is well represented by both estimates.

7.3 Time scales of meridional velocity, oxygen and oxygen flux

Time scales of velocity and oxygen variations being responsible for the oxygen flux were estimated from the 5°N, 23°W and 8°N, 23°W mooring data and are presented throughout this section. Figure 7.3a and 7.3b show the low-pass filtered (cutoff frequency corresponding to a period of $10\,\mathrm{d}$) oxygen and velocity time series from 5°N, 23°W at $400\,\mathrm{m}$ and $500\,\mathrm{m}$ depth (core depth of OMZ), respectively. The corresponding time series of the turbulent meridional oxygen flux that was calculated via the product[51] $v'O_2'$, is shown in Figure 7.4a and 7.4b, respectively. Strong variability is obvious on various time scales which was investigated by spectral analysis and is shown in the following paragraphs.

The corresponding average $\overline{v'O_2'}$ (turbulent meridional oxygen flux using (7.8)) of the flux time series is shown in Figure 7.4c and 7.4d and yields $1.3 \cdot 10^6\ \mu\mathrm{mol\,kg^{-1}\,m\,yr^{-1}}$ and

[51] Note here that not the correlation $\overline{v'O_2'}$, but the simple product was calculated to show the fluctuations of the oxygen flux.

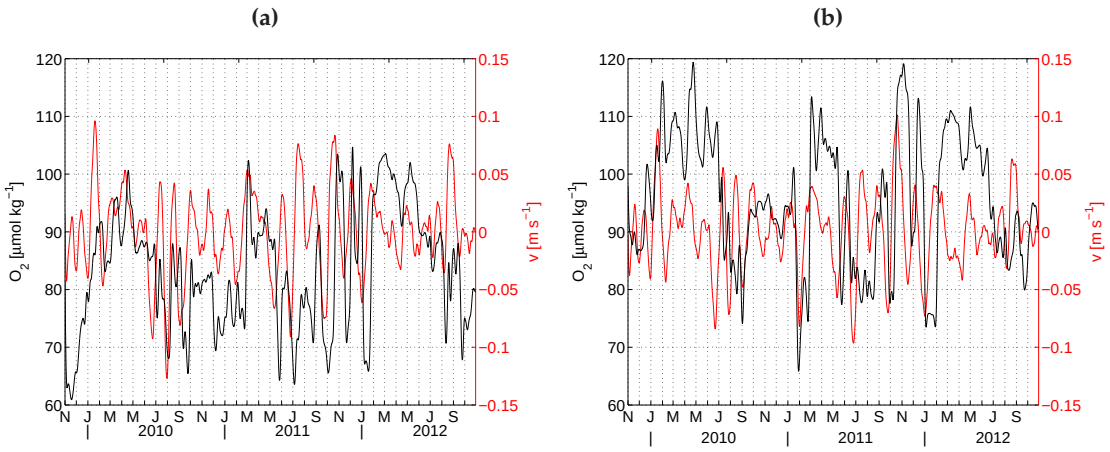

Figure 7.3. Time series of oxygen (black) and meridional velocity (red) from 5°N, 23°W at (a) 400 m and (b) 500 m depth. The time series were low-pass filtered with a cutoff frequency corresponding to a period of 10 d.

$0.3 \cdot 10^6\,\mu\mathrm{mol\,kg^{-1}\,m\,yr^{-1}}$ at 400 m and 500 m depth, respectively (marked by the thick dashed line). Additionally, an annual harmonic was fitted to the oxygen flux time series as indicated by the solid line in Figure 7.4c and 7.4d. Positive and negative phases of the annual cycle are marked by gray and white bars. The amplitude of the annual cycle of the turbulent meridional oxygen flux is of comparable magnitude to the mean turbulent meridional oxygen flux resulting into phases of enhanced and reduced northward oxygen flux at 400 m or enhanced northward and even reversed (southward) oxygen flux at 500 m. The analysis of the annual harmonic of zonal velocity and oxygen was done in section 4.2 and is shown in Figure 4.5 holding an amplitude of about $0.02\,\mathrm{m\,s^{-1}}$ at 400 m (not shown) and $0.01\,\mathrm{m\,s^{-1}}$ at 500 m. About 2 months after maximum eastward velocity, the annual harmonic of oxygen is at maximum suggesting a seasonal variation in the zonal ventilation at the southern boundary of the OMZ that is likely responsible for the seasonal variation in the turbulent meridional oxygen flux.

The power spectral density (PSD) of the unfiltered meridional velocity and oxygen is shown for depths of 400 m and 500 m for 5°N in Figure 7.5a and Figure 7.5b and for 8°N in Figure 7.6a and Figure 7.6b (comparable characteristics were obtained for other depths between 100 m and 800 m). In the double logarithmic presentation, mean spectral slopes between frequencies $1/100\,\mathrm{d^{-1}}$ and $1\,\mathrm{d^{-1}}$ were fitted and are shown for both velocity and oxygen spectra as gray dashed and dash-dotted lines, respectively.

At 5°N (Figure 7.5a and 7.5b), the meridional velocity shows a band of high energy for periods of 30 d - 60 d corresponding to the period of Tropical Instability Waves (TIW). Time scales of TIWs have been reported e.g. by *Athie and Marin* [2008], who determined dominant variability in the period band between 25 d - 50 d. A second maximum was

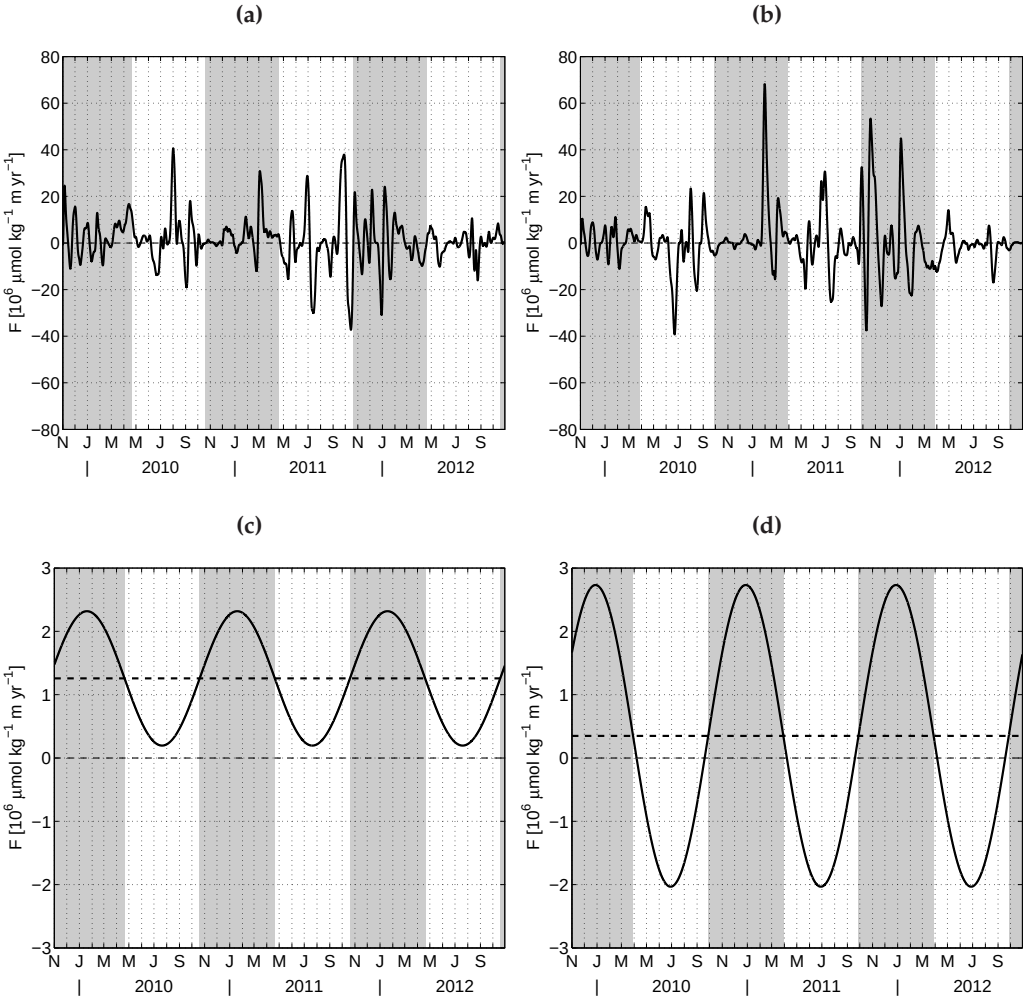

Figure 7.4. Time series of the product $v'O_2'$ (corresponding to oxygen and meridional velocity time series from Figure 7.3) at 5°N,23°W at (a) $400\,\mathrm{m}$ and (b) $500\,\mathrm{m}$ depth. (c) and (d) show the annual harmonic (solid line) that was fitted to $v'O_2'$ at $400\,\mathrm{m}$ and $500\,\mathrm{m}$, respectively. Additionally, the average oxygen flux $\overline{v'O_2'}$ (thick dashed line) is shown. Gray and white regimes mark the positive and negative phases of the estimated annual cycle.

found close to the inertial period ($T_i = 5.7\,\mathrm{d}$) with enhanced energy between $3\,\mathrm{d}$ - $6\,\mathrm{d}$ corresponding to near-inertial oscillations of the ocean. Semidiurnal and diurnal tidal oscillations could be observed as well. Between the inertial period T_i and the period range of TIWs, a distinct minimum of wave energy was found. In contrast, the oxygen PSD shows a more linear decrease in the double logarithmic presentation (corresponding to a power law $f^{-1.5}$ and $f^{-1.7}$ for a depth of $400\,\mathrm{m}$ and $500\,\mathrm{m}$, respectively) from low frequencies to high frequencies with only weak maxima in the period range of TIWs and near-inertial oscillations suggesting that oxygen variability is present on all time scales.

At 8°N (Figure 7.6a and 7.6b), the meridional velocity shows a band of high energy

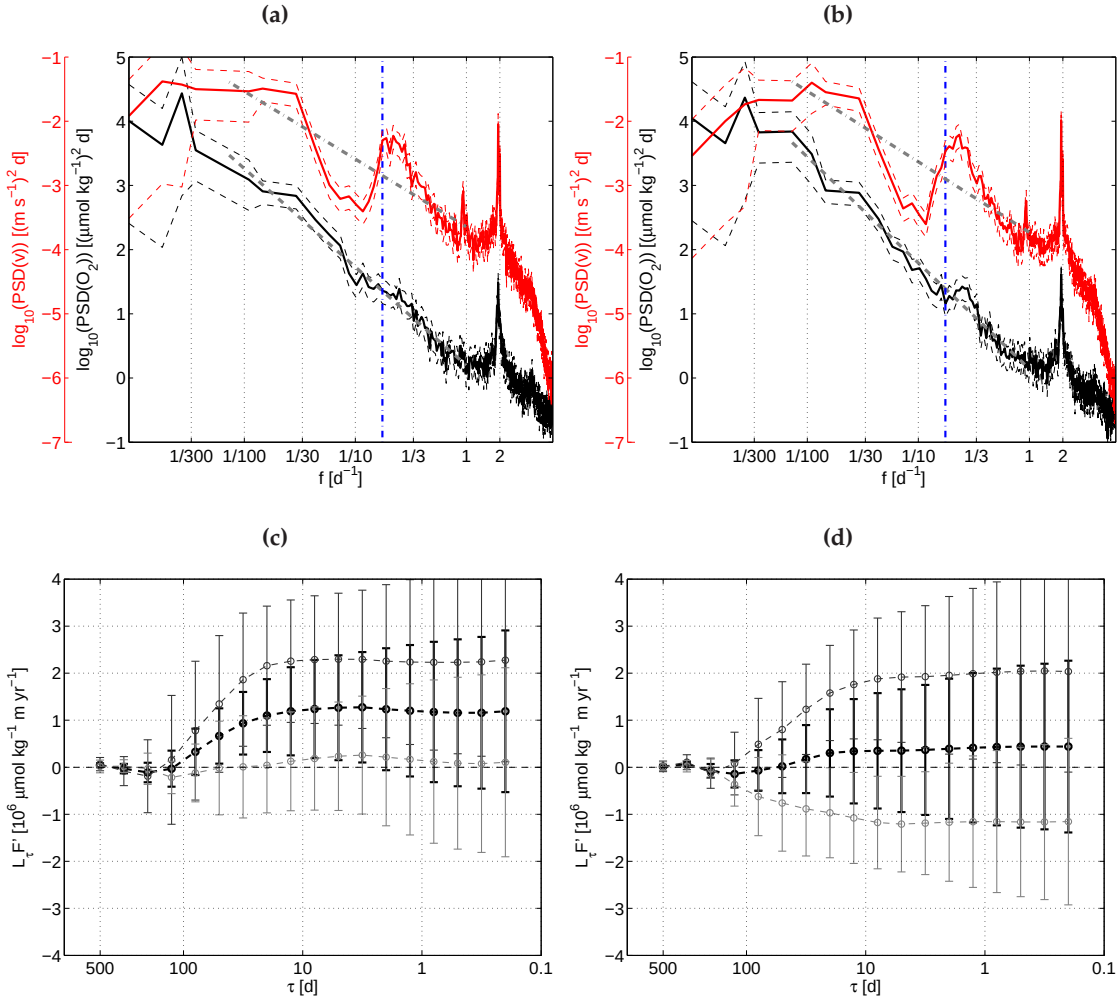

Figure 7.5. (a) Power spectral density of velocity (red solid line) and oxygen (black solid line) at 5°N, 23°W at 400 m depth. The 95% confidence intervals (red and black dashed lines) were calculated by assuming a χ^2-distribution of the power spectral density. Gray dashed and dash-dotted lines mark the spectral slopes (estimated for the frequency band $f = [1/100, 1\,]d^{-1}$) of velocity ($\sim f^{-1.1}$) and oxygen ($\sim f^{-1.5}$), respectively. Blue dash-dotted line marks the inertial period $T_i = 5.7\,\mathrm{d}$ for 5°N. (b) same as (a), but at 500 m depth. Spectral slopes for velocity and oxygen spectra are $\sim f^{-1.1}$ and $\sim f^{-1.7}$, respectively. (c) Cumulative oxygen flux $\mathcal{L}_\tau F'$ (black circles with black dashed thick line) at 5°N, 23°W at 400 m depth calculated using (7.12). The cumulative oxygen flux defines the flux on time scales between the filter period τ and the time length of the mooring time series (here 1094 d). Error bars were calculated as the standard error of the arithmetic mean following (7.9). The dark and light gray circles with thin dashed lines represent the cumulative oxygen flux calculated for the positive and negative half period of the annual cycle of the oxygen flux (indicated by the gray and white regimes in Figure 7.4c). Both estimates reflect the annual variability of the turbulent oxygen flux. (d) Same as (c), but at 500 m depth. The corresponding annual cycle of the turbulent oxygen flux is shown in Figure 7.4d.

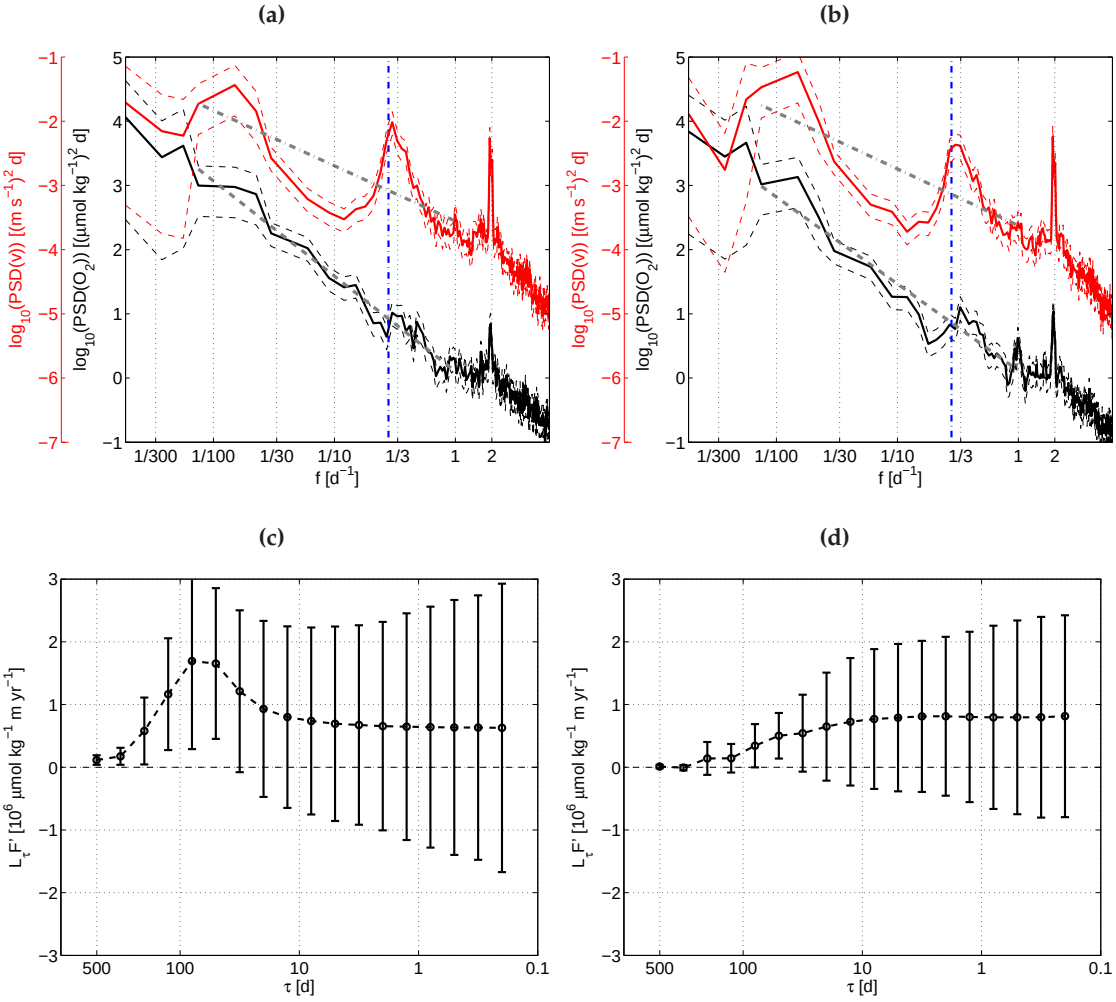

Figure 7.6. Same as Figure 7.5, but for 8°N, 23°W. In (a) the spectral slopes for the velocity and oxygen spectrum are $\sim f^{-0.9}$ and $\sim f^{-1.5}$, respectively, in (b) the spectral slopes are $\sim f^{-0.9}$ and $\sim f^{-1.4}$, respectively. The length of the mooring time series was $533\,\mathrm{d}$. The inertial period for 8°N is $T_i = 3.6\,\mathrm{d}$. In (c) and (d) the annual variability of the turbulent meridional oxygen flux is not included, since the time series was too short for this estimate.

for periods larger than about $35\,\mathrm{d}$. The second energy maximum, corresponding to near-inertial oscillations, was also found, but it is shifted to lower periods ($2\,\mathrm{d}$ - $4\,\mathrm{d}$) due to the lower inertial period at 8°N ($T_i = 3.6\,\mathrm{d}$). Hence, a broader minimum of wave energy between the inertial period and the period range of the mesoscale was observed. Similar to 5°N, the oxygen PSD shows a more linear decrease in double logarithmic presentation from low to high frequencies. The maxima at the inertial period and the period range of the mesoscale as well as the minimum in between are slightly more pronounced at least at $500\,\mathrm{m}$ (also at depths of $600\,\mathrm{m}$ - $800\,\mathrm{m}$, not shown here) suggesting that oxygen variability is slightly decreased on time scales between the inertial period and the period range of the mesoscale.

Figure 7.5c and Figure 7.5d show the turbulent meridional oxygen flux at 5°N at $400\,\mathrm{m}$ and $500\,\mathrm{m}$, respectively, as a function of the low-pass filter period τ (black circles). It is defined as the cumulative oxygen flux $\mathcal{L}_\tau F'$ (cf. (7.12)) on time scales between τ and the time length T_{max} ($= 1094\,\mathrm{d}$) of the mooring time series[52]. Error bars were calculated as the standard error for an arithmetic mean using (7.9). For the limit $\tau \to 0$, the cumulative oxygen flux includes processes on all time scales smaller than the total time period of the time series down to double the sampling interval of $2\,\mathrm{h}$. Strong changes in the cumulative oxygen flux within a certain period band are associated with a strong oxygen flux in this band. Here, strong oxygen fluxes were found for the period band from $10\,\mathrm{d}$ - $80\,\mathrm{d}$ which corresponds to the period range of mesoscale variability. Additionally, the annual variability of the oxygen flux was estimated which is shown by the dark/light gray circles with dashed line. The dark/light gray circles represent the cumulative oxygen flux during the positive/negative phase of the annual cycle of the oxygen flux, represented by the gray and white regimes in Figure 7.4c and Figure 7.4d. During the positive half period, the cumulative oxygen flux is much stronger towards the north, whereas the flux is almost zero (at $400\,\mathrm{m}$) or even directed to the south (at $500\,\mathrm{m}$) during the negative half period.

Similarly, the cumulative oxygen flux as a function of the low-pass filter period τ was calculated for 8°N (time length of the analyzed time series was $533\,\mathrm{d}$) at $400\,\mathrm{m}$ and $500\,\mathrm{m}$ depth and is shown in Figure 7.6c and Figure 7.6d, respectively. At $400\,\mathrm{m}$, most of the oxygen flux was observed in two period bands. A northward oxygen flux was observed in the period band between $80\,\mathrm{d}$ - $300\,\mathrm{d}$, whereas the flux was weaker and directed to the south at periods between $10\,\mathrm{d}$ - $80\,\mathrm{d}$. Summing up the flux on all time scales (i.e. $\tau \to 0$) yielded a northward oxygen flux. At $500\,\mathrm{m}$ depth, a northward oxygen flux was observed, mainly driven on time scales between $10\,\mathrm{d}$ - $100\,\mathrm{d}$. An annual variability of the oxygen flux was not quantified due to a too short time series.

7.4 Eddy-driven meridional oxygen supply

Figure 7.7 shows the eddy-driven meridional oxygen supply along 23°W which was calculated on potential density surfaces using (7.13) and consecutively projected onto depth coordinates. Regions with reddish/bluish colors define an overall gain/loss of oxygen due to meridional eddy diffusion. At depths between $450\,\mathrm{m}$ - $600\,\mathrm{m}$, the eddy-driven meridional oxygen supply into the OMZ (gain of oxygen) is rather constant over latitudes between 6°N - 14°N (region marked by the gray dashed box) with an average value of $2.1\,\mu\mathrm{mol\,kg^{-1}\,yr^{-1}}$. Above $400\,\mathrm{m}$, latitudinally alternating bands of oxygen loss and gain were observed reaching absolute values of more than $10\,\mu\mathrm{mol\,kg^{-1}\,yr^{-1}}$. The equator

[52] By definition, the cumulative oxygen flux is zero for $\tau \to T_{max}$, since the calculation is based on the time series anomalies.

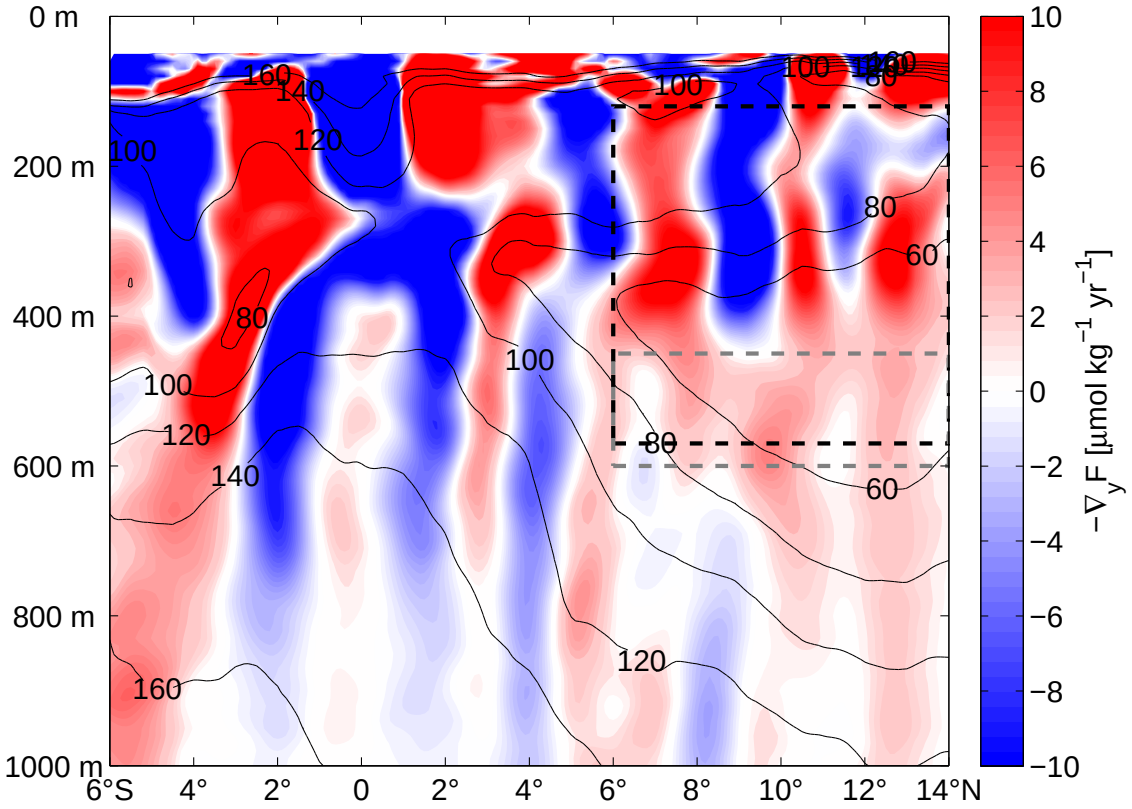

Figure 7.7. Eddy-driven meridional oxygen supply along 23°W. Reddish/bluish colors mark gain/loss of oxygen due to eddy-driven meridional oxygen flux. Superimposed black contour lines mark the mean oxygen distribution. Gray dashed box marks the regime (450 m - 600 m, 6°N - 14°N) of a rather homogeneous oxygen supply in the OMZ with an average value of 2.1 μmol kg^{-1} yr^{-1}. Black dashed box marks the region (120 m - 570 m, 6°N - 14°N) for which a mean eddy-driven meridional oxygen supply was calculated as a function of depth and was used for the estimate of the oxygen budget in Figure 7.8 (section 7.5).

shows an overall loss of oxygen in the upper 400 m. Above 200 m, oxygen is transported poleward to 2°N and 2°S, where a gain of oxygen was observed. This corresponds to the eddy-driven transport of oxygen out of the EUC core into the lower oxygenated westward current branches north and south of the EUC. Below 400 m, a maximum oxygen loss was found at about 2°N and 2°S corresponding to the mean positions of the NICC and SICC which advect oxygen-rich water from the west.

7.5 Oxygen budget of the Tropical North East Atlantic OMZ

Following *Fischer et al.* [2012], who estimated a profile of the diapycnal oxygen supply for the upper half of the TNEA OMZ (120 m - 570 m) in the box 6°N - 15°N and 30°W - 15°W, the 23°W section of the eddy-driven meridional oxygen supply (Figure 7.7) was analyzed

in a similar latitudinal range (6°N - 14°N, illustrated by the black dashed box in Figure 7.7) and an average vertical profile for this regime was calculated. The error of this profile was estimated as follows. For every individual research cruise with a representative CTD/O_2 section along 23°W (cf. Table A.1) a 2^{nd} order polynomial fit was applied to the oxygen data for every single potential density surface to estimate the curvature of the meridional oxygen distribution between 6°N and 14°N. Double the standard deviation σ of all oxygen curvatures was used to estimate the standard error $\Delta = 2\sigma/\sqrt{N}$ (with N the number of all (independent) research cruises) for the average oxygen curvature on a 95% confidence level. Combined with the assumed uncertainty of the eddy diffusivity K_e (factor of 2, cf. section 5.3), the error of the mean meridional oxygen supply in (7.13) was estimated using the standard formula for the error propagation, formally written as

$$\Delta(\nabla_{\sigma y} F_d) = \sqrt{\left(\Delta K_e \nabla^2_{\sigma y} \overline{O_2}\right)^2 + \left(K_e \Delta(\nabla^2_{\sigma y} \overline{O_2})\right)^2} \tag{7.14}$$

Based on the oxygen consumption profile for the TNEA [*Karstensen et al.*, 2008] and the assumption of a steady state, *Fischer et al.* [2012] further proposed a residual oxygen supply reflecting the zonal and meridional isopycnal ventilation of the OMZ. Here, the results regarding the eddy-driven meridional oxygen supply are combined with the results of *Karstensen et al.* [2008] and *Fischer et al.* [2012] to further refine the picture of the ventilation of the TNEA OMZ.

The steady state assumption is in general invalid, as *Stramma et al.* [2008b] determined a significant average oxygen decrease in the TNEA OMZ ($-0.34 \pm 0.13\,\mu\mathrm{mol\,kg^{-1}\,yr^{-1}}$) over the last decades. In the following considerations, this trend (oxygen tendency) is included in the oxygen budget. In general, the oxygen tendency must balance the sum of all other terms (consumption and supply) that contribute to the oxygen budget, hence the oxygen budget can be written as

$$aOUR + O_{2,dia} + O_{2,y,eddy} + R = \partial_t O_2 \tag{7.15}$$

where $aOUR$ is the apparent oxygen utilization rate (oxygen consumption), $O_{2,dia}$ represents the diapycnal oxygen supply, $O_{2,y,eddy}$ is the eddy-driven meridional oxygen supply, R defines the residual oxygen supply due to mean advection and zonal eddy diffusion and $\partial_t O_2$ stands for the oxygen tendency of the TNEA OMZ.

To estimate a mean depth profile for the oxygen tendency $\partial_t O_2$ in the TNEA OMZ, the difference of the apparent oxygen utilization (AOU) between the periods 1999-2008 and 1972-1985 was used that was estimated by *Brandt et al.* [2010] along 23°W. The uncertainties of the AOU for both periods were estimated as double the standard error from all individual CTD/O_2 profiles obtained along 23°W between 6°N and 14°N within the two periods. Finally, the error for the oxygen tendency (95% confidence) was estimated based on the AOU errors from both periods using the standard formula for the error propagation which is $\Delta\partial_t O_2 = \sqrt{(\Delta AOU_1)^2 + (\Delta AOU_2)^2}$.

Figure 7.8 shows the four different terms (left hand side of (7.15)) contributing to the oxygen budget of the TNEA OMZ. Additionally, it shows the oxygen tendency which expresses the mismatch to a hypothetically closed oxygen budget.

Karstensen et al. [2008] proposed an oxygen consumption profile for the TNEA OMZ with an exponential decay as a function of depth which is $aOUR(z) = -0.5+12 \cdot e^{-0.0021 \cdot z}$, with z being depth in m. A 40% error (95% confidence) for the oxygen consumption was

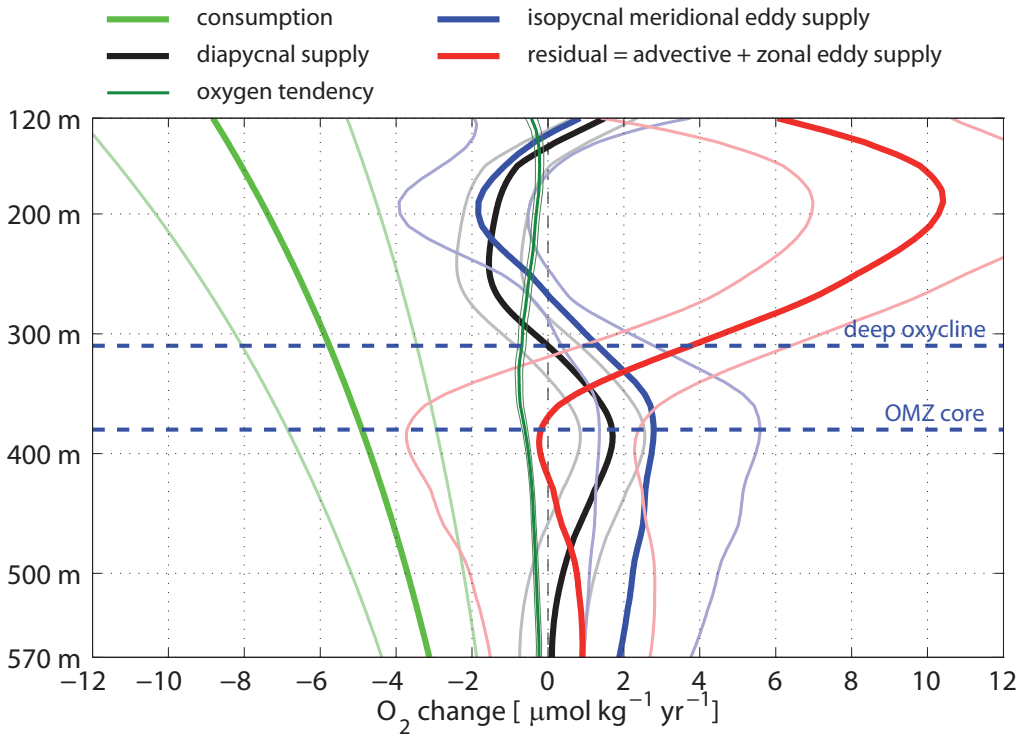

Figure 7.8. Terms contributing to the oxygen budget (O_2 tendency = O_2 consumption + diapycnal O_2 supply + isopycnal meridional O_2 eddy supply + residual O_2 supply) in the Tropical North East Atlantic (latitudinal average between 6°N - 14°N, cf. black dashed box in Figure 7.7) as a function of depth. The oxygen consumption profile (green thick line) was estimated by *Karstensen et al.* [2008]. Diapycnal oxygen supply (black thick line) was estimated by *Fischer et al.* [2012]. The isopycnal meridional eddy-driven oxygen supply (blue thick line) is from this study. Oxygen tendency was estimated as the difference of the apparent oxygen utilization (AOU) between the time periods 1999-2008 and 1972-1985 (data used from *Brandt et al.* [2010]). The residual oxygen supply (red thick line) defines the ventilation through mean advection and zonal eddy diffusion. All error estimates are referred to a 95% confidence (except the isopycnal meridional eddy supply, where the error was estimated from both the error of the oxygen curvature (95% confidence) and the error of the eddy diffusivity (factor 2 assumed); see text for details). Horizontal dashed blue lines mark the depths of the upper boundary (deep oxycline) and the core of the OMZ that were calculated from the mean oxygen profile between 6°N - 14°N.

estimated by the authors. *Fischer et al.* [2012] estimated the diapycnal oxygen supply with an average error of $0.85\,\mu\mathrm{mol\,kg^{-1}\,yr^{-1}}$ (95% confidence). They show that diapycnal mixing supplies the OMZ with about $0.9\,\mu\mathrm{mol\,kg^{-1}\,yr^{-1}}$ in the depth range $350\,\mathrm{m}$ - $570\,\mathrm{m}$ with a maximum supply of about $1.7\,\mu\mathrm{mol\,kg^{-1}\,yr^{-1}}$ at about $390\,\mathrm{m}$ depth. The diapycnal oxygen supply decreases to zero at the upper boundary of the OMZ (deep oxycline). Above, diapycnal mixing contributes to a net oxygen loss in the oxygen-rich Central Waters supplying the OMZ below.

The mean profile of the eddy-driven meridional oxygen supply that was estimated in this study, shows that mesoscale eddies strongly contribute to the ventilation of the OMZ via meridional pathways which is $2.4\,\mu\mathrm{mol\,kg^{-1}\,yr^{-1}}$ in the depth range $350\,\mathrm{m}$ - $570\,\mathrm{m}$. Above this depth range, the eddy-driven meridional oxygen supply decreases and in the shallow Central Water layer between $100\,\mathrm{m}$ - $300\,\mathrm{m}$ it is reversed leading to an oxygen loss.

The oxygen tendency profile shows a maximum oxygen decrease at a depth of about $330\,\mathrm{m}$ which is slightly below the upper boundary of the oxygen minimum zone (deep oxycline) and yields $-0.76\,\mu\mathrm{mol\,kg^{-1}\,yr^{-1}}$. In the depth range $350\,\mathrm{m}$ - $570\,\mathrm{m}$, the average oxygen tendency is $-0.41\,\mu\mathrm{mol\,kg^{-1}\,yr^{-1}}$.

Based on the estimates of all other terms in (7.15), the residual oxygen supply is rather weak at depth of the OMZ (on average $0.4\,\mu\mathrm{mol\,kg^{-1}\,yr^{-1}}$ in the depth range $350\,\mathrm{m}$ - $570\,\mathrm{m}$)[53] suggesting that most of the ventilation is explained by diapycnal mixing and meridional eddy diffusion. Above $350\,\mathrm{m}$, the residual is strongly increased showing a maximum residual oxygen supply of about $10\,\mu\mathrm{mol\,kg^{-1}\,yr^{-1}}$ at $200\,\mathrm{m}$ depth.

[53] The average oxygen consumption yields $-4.1\,\mu\mathrm{mol\,kg^{-1}\,yr^{-1}}$ between $350\,\mathrm{m}$ - $570\,\mathrm{m}$.

CHAPTER 8

Summary and discussion

a) In situ calibration of optode oxygen sensors

This study was based on hydrographic and velocity data that were obtained from repeat ship sections as well as moored observations along 23°W in the Tropical Atlantic. Whereas the processing of CTD/O_2 data from shipboard observations follows standard procedures that ensure high quality data, an in situ calibration procedure for optode oxygen sensors (inspired by recent studies from *Uchida et al.* [2008] and *Bittig et al.* [2012]) was developed, analyzed and applied in this study to achieve a high quality of oxygen data from moored observations. The analysis of 34 different optodes has revealed an average error for the optode oxygen measurements of $4.6\,\mu\mathrm{mol\,kg^{-1}} \pm 1.2\,\mu\mathrm{mol\,kg^{-1}}$ with 95% confidence - evaluated for the upper $1000\,\mathrm{m}$ in the Tropical Atlantic along 23°W as well as for lab calibrations against zero oxygen. On the one hand, this calibration procedure yielded calibration errors that are roughly a factor of 2 worse in comparison to laboratory calibrations. On the other hand, no severe sensor drifts were observed, when the calibration was conducted immediately before and after the field measurement which is an important advantage for this simple calibration method.

The time constants of the individual optode oxygen sensors were determined based on in situ measurements during regular CTD/O_2 casts. It was shown that the time constant correction (assuming an exponential sensor response function) is applicable for these sensors improving the quality of the oxygen data in case of profiling systems (here: for CTD/O_2 casts). However, regarding the calibration error, the quality of oxygen measurements from moored optodes is not affected by this time constant effect.

b) Eddy diffusivity for the Tropical North East Atlantic

A mean depth profile of the lateral eddy diffusivity was estimated based on moored and shipboard observations for the TNEA by applying two different parameterizations. Strictly, the methodology only allowed a reasonable calculation for a limited meridional range from 4°N to 11°N. Nevertheless, the obtained mean profile ($100\,\mathrm{m} - 1000\,\mathrm{m}$) was applied for the complete 23°W section between 6°S and 14°N to qualitatively discuss the regional distribution of oxygen variance production as well as meridional oxygen flux and supply due to mesoscale eddy activity.

The reliability of the estimated eddy diffusivity profile could be proved by (i) comparison with a recent estimate of the eddy diffusivity from the Guinea Upwelling Tracer Release Experiment (GUTRE) and (ii) comparison of the oxygen fluxes based on the diffusive flux parameterization and the correlation of oxygen and meridional velocity time series.

c) Oxygen variability and variance production in the Tropical Atlantic

The Tropical North East Atlantic Ocean is a region of rich oxygen variability. The analysis of repeated shipboard CTD/O_2 sections on density surfaces along 23°W showed that local maxima of oxygen variability exist over the whole section between 6°S - 14°N at depths between $100\,\mathrm{m}$ - $800\,\mathrm{m}$. The representativeness of the oxygen variance section from shipboard observations was tested by comparison with oxygen variance profiles estimated from mooring time series (equator, 2°N, 5°N and 8°N). A good agreement of the variance profiles was found and it is concluded that the estimated section of oxygen variance is a reasonable representation of oxygen variability in the Tropical Atlantic.

Depending on the physical processes that lead to oxygen variability, the oxygen variance section was devided into two regimes. The first regime is defined as the well-ventilated equatorial Atlantic (6°S - 4°N) with its strong mean and variable zonal currents. The second regime covers the region from 4°N to 14°N. In the upper $400\,\mathrm{m}$, it is characterized by latitudinally alternating zonal currents consisting of two mean eastward current branches, namely the surface NECC and the subsurface NEUC at 5°N as well as the northern branch of the NECC (nNECC) at 9°N, meridionally surrounded by westward flow [*Garzoli and Katz*, 1983; *Garzoli and Richardson*, 1989; *Urbano et al.*, 2006]. The currents are strong in the upper $200\,\mathrm{m}$ and decrease with depth. Below $400\,\mathrm{m}$, a sluggish flow regime with weak mean zonal currents exists, where mesoscale eddy fluxes and small scale diapycnal fluxes play a major role in the ventilation (cf. Figure 5.3; see also section 1.2 for a description of the mean flow field).

The oxygen variance (Figure 4.1) in regime 1 (6°S - 4°N) shows a strong coherence (i) to the latitudinally banded structure of the mean zonal currents and (ii) to locations

with a strong mean isopycnal or diapycnal oxygen gradient. In case (i), oxygen variability is assumably caused by seasonal and interannual current variability which leads to variability in the strength of the zonal ventilation from the west [*Brandt et al.*, 2008]. Otherwise, it can be caused by a meridional or vertical displacement of the high/low oxygen regimes which are generally associated with eastward/westward currents. In case (ii), the results derived with the extended Osborn-Cox model point out that mesoscale stirring/diapycnal mixing generates oxygen variance on isopycnal surfaces when acting on a mean isopycnal/diapycnal oxygen gradient. A quantification of the processes mentioned in (i) and (ii) which are responsible for the oxygen variability, cannot be made in the near-equatorial regime. Under such conditions, the full tracer variance equations (cf. (4.4) and (4.5) in *Ferrari and Polzin* [2005]) would have to be considered with their divergent and non-homogeneous terms that are neglected when deriving the extended Osborn-Cox relation.

Nevertheless, the strong oxygen variance maximum at the equator at $300\,\mathrm{m}$ depth could be recently explained by *Brandt et al.* [2012]. They show that most of the oxygen variability is caused by equatorial deep jets having a dominant oscillation period at an interannual time scale of about $4.5\,\mathrm{yr}$ ($\Delta O_2 = 60\,\mu\mathrm{mol\,kg^{-1}}$). In this study, an update of the oxygen and zonal velocity time series (including the mooring period June 2011 - Oct. 2012) was shown, almost comprising a full equatorial deep jet cycle. Oxygen fluctuations observed from the recent mooring period match well with the predictions made in *Brandt et al.* [2012] which corroborates their mechanistic description.

In regime 2 (4°N - 14°N), strong oxygen variability occurred at shallow depths ($100\,\mathrm{m}$) over a wide meridional range as well as at intermediate depths ($300\,\mathrm{m}$ - $800\,\mathrm{m}$). Oxygen variability at intermediate depths was enhanced at the boundaries of the OMZ following the $80\,\mu\mathrm{mol\,kg^{-1}}$ oxygen isoline. Due to a reduced mean flow below a depth of $200\,\mathrm{m}$, mesoscale stirring and diapycnal mixing are the dominant processes for the generation of oxygen variance. Here, it is assumed that the effect of seasonal and longer-term variations of the mean flow field on the oxygen variance is negligible against other terms. In such a regime, the total observed oxygen variance can be considered as the equilibrium state between oxygen variance production and dissipation as described in the extended Osborn-Cox relation. However, in the present study the oxygen variance dissipation could not be determined in order to prove the validity of this relation.

A distinct oxygen variance maximum was found at the southern boundary of the TNEA OMZ (5°N - 8°N, $400\,\mathrm{m}$ - $700\,\mathrm{m}$). Using the extended Osborn-Cox relation it could be shown that this maximum is primarily caused by mesoscale eddy motion stirring the strong mean isopycnal oxygen gradient. The oxygen variance maximum at the upper boundary of the TNEA OMZ ($300\,\mathrm{m}$, 5°N - 12°N) is generated by both mechanisms described in the extended Osborn-Cox model: (i) isopycnal stirring of the mean oxygen field by mesoscale motion and (ii) diapycnal mixing within the mean diapycnal oxygen gradi-

ent. The oxygen variance production by diapycnal mixing is rather constant over latitude. The generation of oxygen variance due to mesoscale stirring is slightly enhanced at 5°N, 8°N and 10°N which might be related to slightly enhanced isopycnal oxygen gradients associated with the pattern of the mean flow field.

The 5°N and 8°N mooring data revealed strong fluctuations of meridional velocity in a period band of 30 d - 60 d (5°N) predominantly associated with TIWs and at periods larger than 35 d (8°N) corresponding to mesoscale activity. A second energy maximum was observed between 3 d - 6 d (5°N) and 2 d - 4 d (8°N), respectively which corresponds to near-inertial oscillations. At 5°N, in contrast, oxygen fluctuations were observed pretty much on all time scales with only weak energy maxima in the period range of TIWs and inertial oscillations, and no distinct minimum in between both time scales. This indicates that mesoscale stirring generates oxygen variability also on shorter time scales leading to a down-cascading of oxygen variance. At 8°N, a weakly pronounced energy minimum of oxygen variability between the similarly weak energy maxima of mesoscale activity and inertial oscillations was observed at least at 500 m depth[54] suggesting the existence of a weak spectral gap. For 5°N, the dominant time scale of oxygen and velocity fluctuations responsible for the oxygen flux at intermediate depths (400 m and 500 m) was found between 10 d - 80 d which is in good agreement with the underlying assumptions of the extended Osborn-Cox model.

The interior of the TNEA OMZ showed little oxygen variability. Due to the fact that weak mean oxygen gradients are present, neither mesoscale stirring nor diapycnal mixing is able to generate elevated oxygen variability in this region.

The cause for the shallow oxygen variance maximum above 200 m (6°N - 14°N) could not be clarified. Stronger mean near-surface zonal currents as well as strong diapycnal oxygen gradients occur at this depth. With the same arguments as for regime 1, it is assumed that zonal current variability as well as diapycnal mixing are responsible mechanisms causing this broad maximum.

d) Eddy-driven meridional oxygen flux and oxygen supply in the Tropical Atlantic

The eddy-driven meridional oxygen flux along 23°W was estimated with the diffusive flux parameterization. An overall northward flux of oxygen through the southern boundary of the OMZ was found (5°N - 8°N, 400 m - 700 m). The flux was strongest at about 5°N and continuously decreased to zero at about 11°N, representing the core of the OMZ. North of 11°N, a southward oxygen flux was observed. Hence, the eddy-driven oxygen flux through the meridional boundaries of the OMZ is directed towards the center of the OMZ.

[54] Similar characteristics were observed for depths between 600 m - 800 m.

For 5°N, 23°W and 8°N, 23°W, the parameterized eddy-driven meridional oxygen flux was compared with the eddy-driven flux derived via the correlation of oxygen and meridional velocity from mooring time series of $3\,\mathrm{yr}$ and $1.5\,\mathrm{yr}$ length, respectively. Although the estimate from a time series of this length is hardly significant, the flux profiles of both independent estimates matched well (at depths of $100\,\mathrm{m}$ - $500\,\mathrm{m}$ for 5°N and at almost all depths from $100\,\mathrm{m}$ - $800\,\mathrm{m}$ for 8°N) and give some confidence in the validity of the estimated oxygen fluxes. Even though rotational fluxes (that have no contribution to the mean tracer budget) cannot be estimated, and thus cannot be excluded, from a single mooring time series, they are assumed to have only a minor contribution to the estimated oxygen fluxes due to weak mean currents (at least at depths below $200\,\mathrm{m}$) [*Marshall and Shutts*, 1981]. At shallower depths ($100\,\mathrm{m}$ - $200\,\mathrm{m}$), a stronger variability of the meridional oxygen fluxes was observed and it is likely that stronger currents at these depths lead to enhanced rotational fluxes [*Marshall and Shutts*, 1981; *Eden et al.*, 2007]. A second reason for the higher variability is that the correlation of oxygen and velocity time series reflects a local estimate of the oxygen flux leading to a higher variability in regions with a strongly changing meridional oxygen gradient. Between 4°N to 6°N, the NECC advects oxygen-rich water from the western boundary eastward, at least during boreal summer [*Stramma et al.*, 2008a]. It is likely that the seasonal variability as well as a meridional meandering of the NECC/NEUC [*Garzoli and Richardson*, 1989] causes a strong variability of the meridional oxygen gradients leading to a higher variability of the meridional oxygen flux (cf. Figure 4.5).

At 5°N, 23°W, a seasonal cycle of the turbulent meridional oxygen flux was discovered which is of the same order of magnitude as the flux itself. The variability was strongest near the surface at depths[55] of $100\,\mathrm{m}$ - $300\,\mathrm{m}$, but it is still evident at larger depths from $400\,\mathrm{m}$ - $800\,\mathrm{m}$ (here, it was shown for $400\,\mathrm{m}$ and $500\,\mathrm{m}$). The calculation of annual harmonics of zonal velocity and oxygen from mooring time series at 5°N, 23°W and $500\,\mathrm{m}$ depth yield an amplitude of about $0.01\,\mathrm{m\,s^{-1}}$ and $6\,\mu\mathrm{mol\,kg^{-1}}$. A phase lag is found with zonal velocity leading oxygen by about two months. These amplitudes are in general agreement with zonal ventilation from the western boundary. Associated changes in the meridional oxygen gradient might thus be responsible for the seasonal cycle of the turbulent meridional oxygen flux. However, a contribution from seasonal variations in the eddy diffusivity (e.g. due to a seasonal cycle in the strength of TIWs) cannot be excluded.

It shall be noted here that the observed seasonal cycle of oxygen at 5°N, 23°W contributes to the total observed oxygen variance with about 20% at depth of the OMZ. This results in a slight overestimate of the eddy length scale (cf. (5.5))[56] and thus in the eddy diffusivity, but is still within the assumed error of K_e (factor 2).

[55] This was not shown for all depths, but exemplarily for $300\,\mathrm{m}$.

[56] Actually, an average eddy length scale was calculated from both oxygen and salinity fluctuations (cf. section 5.3).

The eddy-driven meridional oxygen supply was estimated along 23°W. The interior of the OMZ (6°N - 14°N, $450\,\mathrm{m}$ - $600\,\mathrm{m}$) is characterized by a rather homogeneous oxygen supply due to meridional eddy diffusion with an average value of $2.1\,\mu\mathrm{mol\,kg^{-1}\,yr^{-1}}$. The eddy-driven meridional oxygen flux already suggested that the eddy-driven oxygen supply south of 11°N is maintained by the oxygen flux through the southern boundary of the OMZ, whereas the eddy-driven oxygen supply north of 11°N is maintained by the oxygen flux from the north.

At $100\,\mathrm{m}$ - $400\,\mathrm{m}$, the eddy-driven meridional oxygen supply alternates in meridional bands of strong oxygen flux divergence (O_2 loss) and convergence (O_2 gain). Bands with a strong oxygen loss are centered at 4.5°S, at the equator, 5°N - 6°N and 9°N which corresponds to locations of oxygen-rich eastward currents. In between, bands with a strong oxygen gain coincide with locations of either low-oxygen westward currents or bands with no or weak mean currents. Hence, the mesoscale eddy field redistributes oxygen-rich water from eastward currents and low-oxygen water from westward currents which results in a total loss/gain of oxygen in eastward/westward currents. Locally, eddy-driven meridional oxygen fluxes with an absolute value of about $10\,\mu\mathrm{mol\,kg^{-1}\,yr^{-1}}$ are found and it is assumed that most of the flux is balanced by advection through the mean zonal currents. However, *Brandt et al.* [2010] showed in a conceptual model study that the mean current field can be reasonably described by mean circulation cells. In such cell, a recirculation takes place from an eastward current band into westward current bands north and south of it, also resulting in oxygen fluxes due to mean meridional advection.

e) Oxygen budget of the Tropical North East Atlantic

A refined picture of the oxygen budget in the TNEA (6°N - 14°N along 23°W) was derived by combining the estimate of the eddy-driven meridional oxygen supply from this study with the results from *Karstensen et al.* [2008] and *Fischer et al.* [2012], who estimated the oxygen consumption and the diapycnal oxygen supply, respectively, for the TNEA OMZ. Additionally, the oxygen tendency for the TNEA OMZ [*Stramma et al.*, 2008b; *Brandt et al.*, 2010] was considered reflecting the sum of all terms that contribute to the oxygen budget. The oxygen budget of the TNEA OMZ (here, an average over the depth range of $350\,\mathrm{m}$ - $570\,\mathrm{m}$ was analyzed) was discussed (section 7.5) regarding the terms in (7.15) and is composed as follows. *Karstensen et al.* [2008] found an average oxygen consumption of $-4.1\,\mu\mathrm{mol\,kg^{-1}\,yr^{-1}}$. Diapycnal mixing supplies the OMZ with about $0.9\,\mu\mathrm{mol\,kg^{-1}\,yr^{-1}}$ [*Fischer et al.*, 2012], whereas meridional eddy fluxes ventilate the OMZ with about $2.4\,\mu\mathrm{mol\,kg^{-1}\,yr^{-1}}$. The oxygen tendency is about $-0.4\,\mu\mathrm{mol\,kg^{-1}\,yr^{-1}}$ (data used from *Brandt et al.* [2010]). Thus, the residual oxygen supply required to balance all the other terms is $\sim 0.4\,\mu\mathrm{mol\,kg^{-1}\,yr^{-1}}$. This residual supply consists of (i) an oxygen supply through mean advection and (ii) an eddy-driven zonal oxygen supply. The eddy-driven zonal oxygen supply is expected to be at least an order of magnitude smaller than

the eddy-driven meridional oxygen supply, since the zonal curvature of the mean isopycnal oxygen distribution is much smaller than the meridional curvature[57]. If the eddy-driven zonal oxygen supply is negligible, the mean advection will account for an oxygen supply of $0.4\,\mu\mathrm{mol\,kg^{-1}\,yr^{-1}}$. Consequently, the eddy-driven meridional oxygen flux is the dominant mechanism for the ventilation of the TNEA OMZ. A comparison shows that the eddy-driven meridional oxygen supply accounts for almost 60%, the diapycnal supply for about 20% and the advective supply for less than 10% of the total required oxygen supply ($-4.1\,\mu\mathrm{mol\,kg^{-1}\,yr^{-1}}$) at the depth range between $350\,\mathrm{m}$ - $570\,\mathrm{m}$. The oxygen trend estimated by *Stramma et al.* [2008b] and *Brandt et al.* [2010] reveals that about 10% of the consumed oxygen are not supplied by any of these ventilation processes.

The observed oxygen decrease over the last decades in the TNEA OMZ ($-0.34 \pm 0.13\,\mu\mathrm{mol\,kg^{-1}\,yr^{-1}}$, [*Stramma et al.*, 2008b]) reveals that some changes, either in the ventilation or the oxygen consumption, must have happened during this period. *Brandt et al.* [2010] suggested that a weakening of the nNECC, in particular at depth of the OMZ, could have contributed to such oxygen decrease. This might be corroborated by the shape of the oxygen tendency depth profile showing maximum oxygen decrease at about $330\,\mathrm{m}$ depth slightly below the deep oxycline. Such depth dependence of the oxygen tendency would be in agreement with a general weakening and/or shallowing of the advective oxygen supply. Here, it shall be only noted that the average oxygen tendency at depth of the OMZ is $-0.4\,\mu\mathrm{mol\,kg^{-1}\,yr^{-1}}$ which is a non-negligible term in the oxygen balance. It corresponds to about 10% of the magnitude of the oxygen consumption, 20% of the magnitude of the eddy-driven meridional oxygen flux, and about 45% of the magnitude of the diapycnal oxygen supply. As an instructive example, to close the oxygen budget just by an increase of the eddy-driven meridional oxygen flux, the oxygen curvature between northern and southern boundary of the OMZ (or the oxygen difference between OMZ core and its northern and southern boundary) would have to increase by 20% when assuming no change in the eddy diffusivity K_e which corresponds to a substantial deoxygenation in the core of the OMZ.

Above the OMZ in a depth range of $120\,\mathrm{m}$ - $350\,\mathrm{m}$, meridional eddy fluxes and diapycnal mixing lead to a loss of oxygen. The residual oxygen supply is largest in this depth range showing a maximum of $10\,\mu\mathrm{mol\,kg^{-1}\,yr^{-1}}$ at $200\,\mathrm{m}$ depth. Considering Figure 7.7, this result can be the effect of an asymmetric average over meridional bands of strong oxygen flux divergence and convergence. It is supposed that a meridional average including latitudes further north (>14°N) would reduce the strength of this residual. However, the essential mechanism responsible for the ventilation of this regime is the mean advection through the circulation cells associated with zonal jets, whereas the eddy diffusion leads to a meridional redistribution of oxygen between these jets. Hence, a substantial contribution of the mean advection at this depth range is expected.

[57] The diffusive oxygen supply is the stronger the larger the curvature (2^{nd} derivative) of the isopycnal oxygen distribution (cf. (7.13)).

CHAPTER 9

Outlook

This study quantified the regional distribution and time scales of oxygen variability in the Tropical Atlantic along 23°W. The respective roles of two variance generating processes (mesoscale stirring and diapycnal mixing) were identified. In particular, these processes are responsible for the oxygen variability at the southern and upper boundary of the TNEA OMZ.

However, a quantitative analysis of the length scales, corresponding to these fluctuations, is still pending. For this purpose, a triangular mooring array (with a lateral distance between these moorings of $\approx 60\,\mathrm{km}$) was deployed at the southern boundary of the OMZ at 5°N, 23°W in Nov. 2012 (planned to be recovered in 2014) in order to observe submesoscale oxygen variability which is generated by mesoscale eddy activity. In parallel, a glider swarm experiment (consisting of 3 gliders) was conducted at the same position between Nov. 2012 - Dec. 2012 in order to record corresponding length scales with a lateral and vertical resolution of $> 4\,\mathrm{km}$ and $1\,\mathrm{m}$, respectively. The combined analysis of both data sets will provide a better quantitative understanding of the oxygen variability and its corresponding length scales at the southern boundary of the OMZ.

For a comprehensive study of the oxygen variability in the Tropical Atlantic, particularly at the southern boundary of the OMZ, a high-resolution advection-diffusion model is necessary. Spectral analysis of the modeled oxygen field, both in frequency and wavenumber space, and the comparison with frequency and wavenumber spectra of oxygen obtained from moored and glider observations, may improve the mechanistic understanding of mesoscale stirring as a variance generating process. In this context, it is of central interest to further understand the oxygen fluctuations observed over a frequency band in the oxygen spectrum ranging from mesoscale variability to fluctuations at the inertial period. This suggests an energy cascade from low to high frequencies and

wavenumbers, respectively, whose phyiscal description remains unclear.

Apart from mesoscale activity, longer-term oxygen fluctuations were observed. Particularly at the 5°N, 23°W mooring position, the annual cycle of the NECC/NEUC is likely responsible for the phase-delayed annual cycle of the oxygen concentration which in turn is likely related to the annual variability of the eddy-driven meridional oxygen flux. Moreover, the annual variability of the mesoscale activity (e.g. the energy of TIWs is maximum in boreal summer) could be another process contributing to the annual variability of the meridional oxygen flux. However, further analysis needs to be done to identify the driving mechanisms. In particular, a meridional structure of the annual variability of the oxygen and velocity field may help to analyze and interpret the observed features.

Meridional ship sections and moored observations along 23°W will be continued during upcoming research cruises and, thus, will improve the estimates of (i) the regional distribution of the mean oxygen and the oxygen variability and (ii) the meridional oxygen flux, oxygen supply and thus the oxygen budget of the TNEA OMZ.

Using the in situ calibration procedure for *AADI* optode oxygen sensors which was validated in this study, high quality oxygen measurements will be provided for future glider and moored observations. The time constant correction for profiling systems will be applied on glider-based oxygen measurements, but the effect of this correction remains to be quantified.

Appendix

APPENDIX A

Data - Tables

In the following, an overview about the data is given which was used within this study. CTD/O_2 profiles and shipboard ADCP data were acquired during repeat ship sections along 23°W (Table A.1). Table A.2 gives an overview about all oxygen time series recorded with *AADI* optode oxygen sensors. Table A.3 shows all optode oxygen sensors that were deployed in combination with *Sea-Bird* microcats (CTD sensors) to allow a projection of oxygen on potential density surfaces. In Table A.4, an overview about ADCP data from moored observations is given. Climatological hydrographic mean fields were taken from the World Ocean Atlas 2009 (WOA09, `http://www.nodc.noaa.gov/OC5/WOA09/pr_woa09.html`).

Table A.1. Shipboard ADCP and CTD/O_2 sections between 6°S - 14°N and 22°W - 24°W. lat. / lon. and depth of each section mark the latitude and longitude range as well as the maximum depth of the used data. # profiles marks the number of CTD/O_2 profiles that were available from this cruise and were used for the analysis. A dash signifies that no velocity or CTD/O_2 data was used from this cruise.

cruise (date)	VM-ADCP / L-ADCP		CTD/O_2		
	lat. / lon.	depth [m]	lat. / lon.	depth [m]	# profiles
Thalassa (Jul-Aug 1999)	6°S-6°N / 23°W	1000	6°S-6°N / 23.1°W-22.5°W	1000	45
Seward Johnson (Jan 2000)	6°S-4°N / 23°W	1000	-	-	-
Meteor 47/1 (Apr 2000)	5°S-4°N / 23°W	1000	5°S-4°N / 24.0°W-23.0°W	1000	27
Meteor 55 (Oct 2002)	0°-10°N / 24°W	650	-	-	-
Polarstern Ant XXII/5 (Jun 2005)	6°S-14°N / 23°W	300	-	-	-
Meteor 68/1 (May 2006)	2°S-0.5°N / 23°W	500	-	-	-
Ron Brown (Jun 2006)	5°S-13.5°N / 23°W 5°S-14°N / 23°W	750 750	5°S-14°N / 23.0°W	1000	96
Meteor 68/2 (Jun-Jul 2006)	4°S-14°N / 23°W	1000	4°S-14°N / 23.2°W-22.0°W	1000	48
Ron Brown (May 2007)	4°N-14°N / 23°W	750	4°N-14°N / 23.1°W-22.6°W	1000	22
L'Atalante (Feb-Mar 2008)	2°S-14°N / 23°W 2°S-14°N / 23°W	400 1000	2°S-14°N / 23.1°W-23.0°W	1000	48
Merian 08/1 (April-May 2008)	7.5°N-14°N / 23°W	600	7°N-11°N / 24.0°W-22.0°W	1000	36
Merian 10/1 (Nov-Dec 2008)	4°N-14°N / 23°W	650	4°N-14°N / 24.0°W-22.0°W	1000	70
Polarstern Ant XXV/5 (May 2009)	6°S-14°N / 23°W	250	-	-	-
Endeavor 463 (May-Jun 2009)	4°S-3°N / 23°W	700	-	-	-
Ron Brown (Jul-Aug 2009)	0°-14°N / 23°W	700	-	-	-
Polarstern Ant XXVI/1 (Nov 2009)	6°S-14°N / 23°W	250	-	-	-
Meteor 80/1 (Oct-Nov 2009)	5°S(6°S)-14°N / 23°W 6°S-14°N / 23°W	1000 (590) 600	5°S-14°N / 23.1°W-23.0°W	1000	76
Meteor 80/2 (Dec 2009)	-	-	4°N-11°N / 24.0°W-22.0°W	1000	9
Meteor 81/1 (Feb-Mar 2010)	6°S-13°N / 22°W	1000	-	-	-
Polarstern Ant XXVI/4 (May 2010)	5°S-13.5°N / 23°W	250	-	-	-
Meteor 83/1 (Oct-Nov 2010)	-	-	2°N-14°N / 24.0°W-22.0°W	1000	21
MSM18/2 (May-Jun 2011)	0°-14°N / 23°W 5°S-5°N / 23°W	1000 1000	5°S-5°N / 23.0°W	1000	29
Ron Brown (Jul-Aug 2011)	0°-12.2°N (14°N) / 23°W	700 (650)	-	-	-

Table A.2. Oxygen sensors deployed during different mooring periods and at different depths along 23°W at equator, 2°N, 4°N, 5°N, 8°N and 11.5°N.

date (mm/yyyy)	depth [m]
0°N, 23°W	
03/2008 - 03/2008 (2 weeks)	300 / 500
11/2009 - 05/2011	300 / 500
06/2011 - 10/2012	300 / 500
2°N, 23°W	
03/2008 - 10/2009	300 / 500
11/2009 - 05/2011	300 / 500
4°N, 23°W	
07/2009 - 04/2010	300 / 500
05/2010 - 07/2011	300 / 500
5°N, 23°W	
11/2009 - 05/2011	100 / 200 / 300 / 400 / 500 / 600 / 700 / 800
05/2011 - 10/2012	100 / 200* / 300 / 400 / 500 / 600 / 800
8°N, 23°W	
11/2009 - 05/2011	100 / 200 / 300 / 400 / 500 / 600 / 700 / 800
05/2011 - 10/2012	100 / 200 / 300 / 400 / 500 / 600 / 700 / 800
11.5°N, 23°W	
07/2009 - 04/2010	300 / 500
05/2010 - 07/2011	300 / 500

* data recorded only for four months (05/2011 - 09/2011)

Table A.3. CTD and oxygen sensors deployed next to each other during different mooring periods and at different depths along 23°W (equator, 2°N, 5°N and 8°N). The quality of salinity (S), temperature (T) and oxygen (O_2) time series is shown. A cross marks a clean record (100% good data) of the instrument. Percentages signify the rate of good data referred to the total mooring time period.

date (mm/yyyy)	depth [m]	S	T	O_2
0°N, 23°W				
03/2008 - 03/2008	300	x	x	2%
	500	x	x	2%
11/2009 - 05/2011	300	x	x	x
	500	x	x	x
2°N, 23°W				
03/2008 - 10/2009	300	x	x	x
	500	x	x	x
5°N, 23°W				
11/2009 - 05/2011	100	x	x	x
	200	x	x	x
	300	x	x	x
	400	x	x	x
	500	x	x	x
	600	x	x	x
	700	x	x	x
	800	0%	x	x
05/2011 - 10/2012	100	x	x	x
	200	x	x	24%
	300	x	x	x
	400	x	x	x
	500	x	x	x
	600	x	x	x
	700	x	x	0%
	800	x	x	x
8°N, 23°W				
11/2009 - 05/2011	100	x	x	x
	200	x	x	x
	300	x	x	x
	400	x	x	x
	500	x	x	x
	600	0%	x	x
	700	41%	x	x
	800	x	x	x
05/2011 - 10/2012	100	x	x	x
	200	x	x	x
	300	x	x	x
	400	x	x	x
	500	x	x	x
	600	x	x	x
	700	28%	x	x
	800	96%	x	x

Table A.4. Moored ADCPs that were deployed at the equator, 5°N and 8°N along 23°W during different mooring periods. Depths or depth ranges for measurements of horizontal velocity are shown that were used within this study.

date (mm/yyyy)	used ADCP depths [m]
0°N, 23°W	
03/2008 - 10/2009	300 / 500
11/2009 - 05/2011	300 / 500
06/2011 - 10/2012	300 / 500
5°N, 23°W	
07/2006 - 02/2008	70 - 750
11/2009 - 05/2011	100 - 780
05/2011 - 10/2012	60 - 750
8°N, 23°W	
05/2011 - 10/2012	60 - 750

APPENDIX B

Theory of the sensor response function

The response function of the optode oxygen sensor can be basically described with an exponential behaviour. Mathematically, this is expressed by a convolution of the true oxygen signal $O_2(t)$ which shall be approached here with the oxygen profile of the CTD, with the response function of the optode, defined as $h = \mathrm{e}^{-\frac{t}{\tau}}$. Here, τ is the time constant of the sensor defining the time of 63% adjustment to the true oxygen concentration. Applying the definition of the convolution, the optode signal at the time point t_0 is given by

$$\begin{aligned} O_2^{opt}(t_0) &= O_2(t_0) * h(t_0) \\ &= \int_{-\infty}^{\infty} O_2(t')\, h(t_0 - t')\, dt' \\ &= \int_{-\infty}^{t_0} O_2(t')\, \mathrm{e}^{-\frac{t_0 - t'}{\tau}}\, dt' \end{aligned} \tag{B.1}$$

In the last step the response function $h(t)$ was only defined for $t > 0$ (i.e. $t' < t_0$) for reasons of causality that is the optode only reacts to past events. Since the signals of CTD and optode are discrete, (B.1) is transformed into a sum. By Considering the normalization in the discrete case[58] it is

$$O_2^{opt}(t_0) = \sum_{i=0}^{N} O_2(t_0 - i\triangle t)\mathrm{e}^{-\frac{i\triangle t}{\tau}} \Bigg/ \sum_{i=0}^{N} \mathrm{e}^{-\frac{i\triangle t}{\tau}} \tag{B.2}$$

The index i only runs over positive values due to causality and $\triangle t$ defines the sampling interval of the optode. Strictly, it is $N \to \infty$ to fulfill the convergence to the continuous

[58] In the continuous case, the normalization is $\int_{-\infty}^{t_0} \mathrm{e}^{-\frac{t_0 - t'}{\tau}}\, dt' = 1$ and thus not written at all.

case (B.1) and (B.2) can be further transformed:

$$\begin{aligned} O_2^{opt}(t_0) &= \frac{O_2(t_0)}{\sum_{i=0}^{N} \mathrm{e}^{-\frac{i\triangle t}{\tau}}} + \frac{\sum_{i=1}^{N} O_2(t_0 - i\triangle t)\mathrm{e}^{-\frac{i\triangle t}{\tau}}}{\sum_{i=0}^{N} \mathrm{e}^{-\frac{i\triangle t}{\tau}}} \\ &= \frac{O_2(t_0)}{\sum_{i=0}^{N} \mathrm{e}^{-\frac{i\triangle t}{\tau}}} + \underbrace{\frac{\sum_{i=0}^{N} O_2(t_0 - (i+1)\triangle t)\mathrm{e}^{-\frac{i\triangle t}{\tau}}}{\sum_{i=0}^{N} \mathrm{e}^{-\frac{i\triangle t}{\tau}}}}_{=O_2^{opt}(t_0-\triangle t)} \mathrm{e}^{-\frac{\triangle t}{\tau}} \\ &= \frac{O_2(t_0)\cdot(1-\mathrm{e}^{-\frac{\triangle t}{\tau}})}{\underbrace{\sum_{i=0}^{N} \mathrm{e}^{-\frac{i\triangle t}{\tau}}\cdot(1-\mathrm{e}^{-\frac{\triangle t}{\tau}})}_{=1-\mathrm{e}^{-\frac{(N+1)\triangle t}{\tau}} \longrightarrow 1\ (N\to\infty)}} + O_2^{opt}(t_0-\triangle t)\cdot\mathrm{e}^{-\frac{\triangle t}{\tau}} \end{aligned} \tag{B.3}$$

Hence, the optode oxygen is given by the two point formula

$$O_2^{opt}(t_0) = O_2(t_0)\cdot(1-\mathrm{e}^{-\frac{\triangle t}{\tau}}) + O_2^{opt}(t_0-\triangle t)\cdot\mathrm{e}^{-\frac{\triangle t}{\tau}} \tag{B.4}$$

It shall be noted that the recursive expression in (B.4) is a simple model to describe the time response of the optode, but needs an accurate initial value based on a steady state. On the other hand, using (B.4) the original oxygen profile can be estimated by deconvoluting the optode oxygen signal.

The transfer function of the convolution is given by the Fourier transform of the convolution function[59]:

$$\begin{aligned} \widetilde{h}(\omega) &= \int_0^\infty \mathrm{e}^{-t/\tau}\mathrm{e}^{\mathrm{i}\omega t}dt \\ &= -\frac{1}{1/\tau+\mathrm{i}\omega}\,\mathrm{e}^{-t(1/\tau+\mathrm{i}\omega)}\Big|_0^\infty \\ &= \frac{1/\tau-\mathrm{i}\omega}{1/\tau^2+\omega^2} \end{aligned} \tag{B.5}$$

Taking the modulus of the transfer function gives a spectrum that represents the filter properties of the convolution function:

$$|\widetilde{h}(\omega)| = \frac{1}{\sqrt{1/\tau^2+\omega^2}} \tag{B.6}$$

Here, dimensionless variables are defined

$$\begin{aligned} \omega &\to \omega_\tau = \omega\cdot\tau \\ \widetilde{h}(\omega) &\to \widetilde{h}_\tau(\omega_\tau) = \frac{\widetilde{h}(\omega_\tau)}{\tau} \end{aligned} \tag{B.7}$$

The spectrum $\left|\widetilde{h}_\tau(\omega_\tau)\right|$ of the transfer function is shown in Figure B.1 representing the characteristics of a low-pass filter with the cutoff frequency ω_τ.

[59] This is based on the convolution theorem $\mathscr{F}\{g*h\} = \sqrt{2\pi}\mathscr{F}\{g\}\cdot\mathscr{F}\{h\}$.

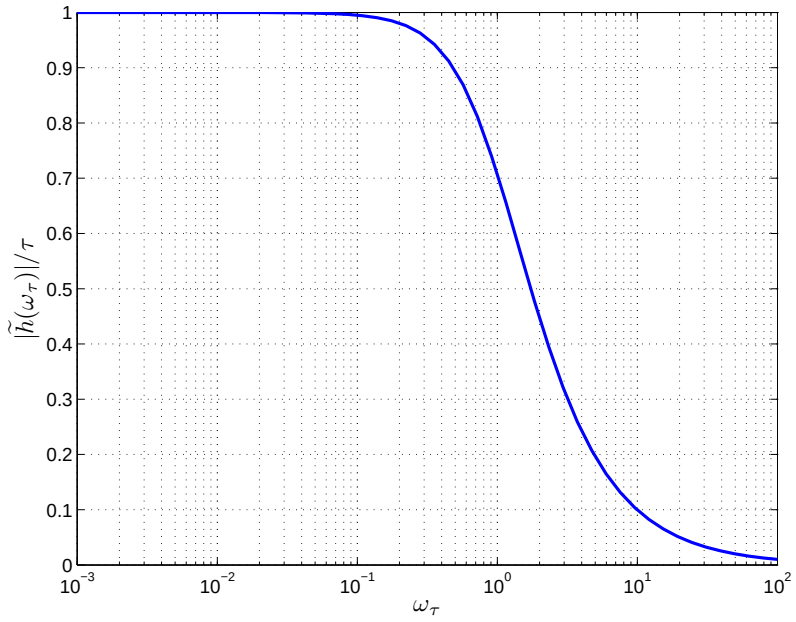

Figure B.1. Transfer function $|\widetilde{h_\tau}(\omega_\tau)|$ of the convolution

To determine the transfer function of the deconvolution the deconvolution function has to be defined. In general, the deconvolution of the optode signal can be defined as a convolution with the convolution function $h^\dagger(t)$:

$$O_2(t_0) = O_2^{opt}(t_0) * h^\dagger(t_0) = \int_{-\infty}^{\infty} O_2^{opt}(t')h^\dagger(t_0 - t')\,dt' \tag{B.8}$$

The determination of $h^\dagger(t)$ is not trivial, but can be found here by comparing (B.8) with (B.4):

$$h^\dagger(t) = \frac{\delta(t)}{1 - \mathrm{e}^{-\frac{(t+\triangle t)}{\tau}}} - \frac{\delta(t-\triangle t)\mathrm{e}^{-\frac{t}{\tau}}}{1 - \mathrm{e}^{-\frac{t}{\tau}}} \tag{B.9}$$

Again, the Fourier transform of $h^\dagger(t)$ is calculated

$$\begin{aligned}
\mathscr{F}\{h^\dagger(t)\} &= \int_{-\infty}^{\infty} \left(\frac{\delta(t)}{1 - \mathrm{e}^{-\frac{(t+\triangle t)}{\tau}}} - \frac{\delta(t-\triangle t)\mathrm{e}^{-\frac{t}{\tau}}}{1 - \mathrm{e}^{-\frac{t}{\tau}}} \right) \mathrm{e}^{-\mathrm{i}\omega t} dt \\
&= \frac{\mathrm{e}^{-i\omega\cdot 0}}{1 - \mathrm{e}^{-\frac{\triangle t}{\tau}}} - \frac{\mathrm{e}^{-\triangle t(1/\tau + \mathrm{i}\omega)}}{1 - \mathrm{e}^{-\frac{\triangle t}{\tau}}} \\
\widetilde{h}^\dagger(\omega) &= \frac{1 - \mathrm{e}^{-\triangle t(1/\tau + \mathrm{i}\omega)}}{1 - \mathrm{e}^{-\frac{\triangle t}{\tau}}}
\end{aligned} \tag{B.10}$$

and the modulus yields again the spectrum:

$$\begin{aligned}
|\widetilde{h}^\dagger(\omega)| &= \frac{1}{1 - \mathrm{e}^{-\frac{\triangle t}{\tau}}} \sqrt{\left[1 - \mathrm{e}^{-\frac{\triangle t}{\tau}} cos(\omega\triangle t)\right]^2 + \left[\mathrm{e}^{-\frac{\triangle t}{\tau}} sin(\omega\triangle t)\right]^2} \\
&= \frac{1}{1 - \mathrm{e}^{-\frac{\triangle t}{\tau}}} \sqrt{1 - 2\mathrm{e}^{-\frac{\triangle t}{\tau}} cos(\omega\triangle t) + \mathrm{e}^{-\frac{2\triangle t}{\tau}}}
\end{aligned} \tag{B.11}$$

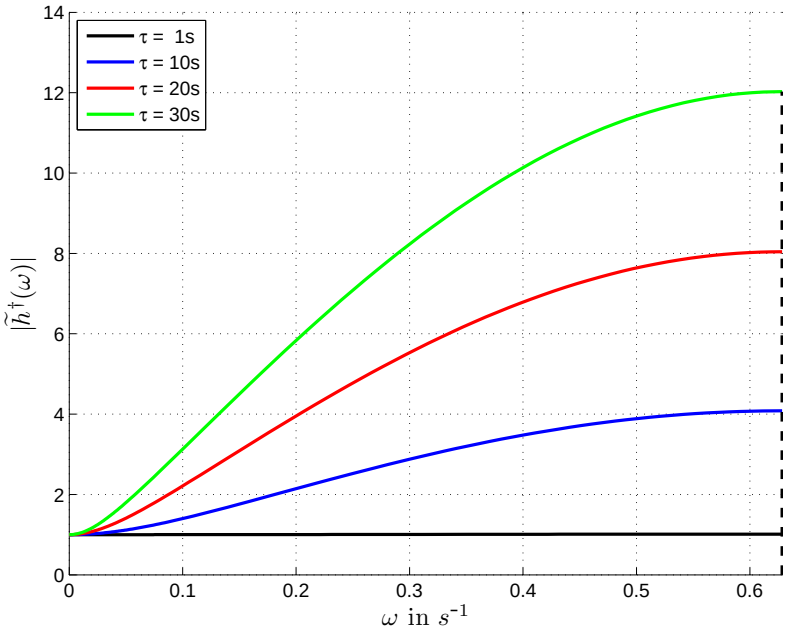

Figure B.2. Transfer function $|\widetilde{h}^{\dagger}(\omega)|$ of the deconvolution in dependence of the time constant τ (at a sampling rate of $\triangle t = 5\,\mathrm{s}$)

The spectrum $|\widetilde{h}^{\dagger}(\omega)|$ is only reasonable in the interval $\omega \in [0, \omega_{max}]$ with the Nyquist frequency $\omega_{max} = 2\pi f_{max} = \pi/\triangle t$ The transfer function of the deconvolution (B.8) is shown in Figure B.2.

Being the inverse of the convolution function $h(t)$ (low-pass filter) the deconvolution function $h^{\dagger}(t)$ strongly amplifies high frequencies, whereas low frequency oscillations ($\omega \to 0$) remain unchanged that is oscillations on the Nyquist frequency, such as sensor noise, can strongly affect the quality of the deconvoluted signal.

Bibliography

AADI (2007): *TD 218 Operating Manual Oxygen Optode 3830, 3835, 3930, 3975, 4130, 4175*. (Aanderaa Data Instruments).

AADI (2009): *TD 269 Operating Manual Oxygen Optode 4330, 4835*. (Aanderaa Data Instruments).

Antonov, J. I., D. Seidov, T. P. Boyer, R. A. Locarnini, A. V. Mishonov, H. E. Garcia, O. K. Baranova, M. M. Zweng and D. R. Johnson (2010): *World Ocean Atlas 2009, Volume 2: Salinity*. Tech. rep., S. Levitus, Ed. NOAA Atlas NESDIS 69, U.S. Government Printing Office, Washington, D.C., 184 pp.

Ascani, F., E. Firing, P. Dutrieux, J. P. McCreary and A. Ishida: Deep Equatorial Ocean Circulation Induced by a Forced-Dissipated Yanai Beam. *Journal of Physical Oceanography*, **40**, 1118–1142 (2010).

Athie, G. and F. Marin: Cross-equatorial structure and temporal modulation of intraseasonal variability at the surface of the Tropical Atlantic Ocean. *Journal of Geophysical Research - Oceans*, **113**, C08020 (2008).

Banyte, D., T. Tanhua, M. Visbeck, D. W. R. Wallace, J. Karstensen, G. Krahmann, A. Schneider, L. Stramma and M. Dengler: Diapycnal diffusivity at the upper boundary of the tropical North Atlantic oxygen minimum zone. *Journal of Geophysical Research - Oceans*, **117**, C09016 (2012).

Banyte, D., M. Visbeck, T. Tanhua, T. Fischer, G. Krahmann and J. Karstensen (2013): Lateral diffusivity from tracer release experiments in the tropical north atlantic thermocline. *submitted to Journal of Geophysical Research*.

Bittig, H. C., B. Fiedler, T. Steinhoff and A. Körtzinger: A novel electrochemical calibration setup for oxygen sensors and its use for the stability assessment of Aanderaa optodes. *Limnology and Oceanography - Methods*, **10**, 921–933 (2012).

Bopp, L., C. Le Quere, M. Heimann, A. Manning and P. Monfray: Climate-induced oceanic oxygen fluxes: Implications for the contemporary carbon budget. *Global Biogeochemical Cycles*, **16** (2002).

Bourles, B., R. Lumpkin, M. J. McPhaden, F. Hernandez, P. Nobre, E. Campos, L. Yu, S. Planton, A. Busalacchi, A. D. Moura, J. Servain and J. Trotte: The PIRATA program: History, accomplishments, and future directions. *Bulletin of the American Meteorological Society*, **89**, 1111+ (2008).

Brandt, P. and C. Eden: Annual cycle and interannual variability of the mid-depth tropical Atlantic Ocean. *Deep-Sea Research Part I - Oceanographic Research Papers*, **52**, 199–219 (2005).

Brandt, P., R. J. Greatbatch, M. Claus, S.-H. Didwischus, V. Hormann, A. Funk, J. Hahn, G. Krahmann, J. Fischer and A. Körtzinger: Ventilation of the equatorial Atlantic by the equatorial deep jets. *Journal of Geophysical Research - Oceans*, **117** (2012).

Brandt, P., V. Hormann, B. Bourles, J. Fischer, F. A. Schott, L. Stramma and M. Dengler: Oxygen tongues and zonal currents in the equatorial Atlantic. *Journal of Geophysical Research - Oceans*, **113** (2008).

Brandt, P., V. Hormann, A. Körtzinger, M. Visbeck, G. Krahmann, L. Stramma, R. Lumpkin and C. Schmid: Changes in the Ventilation of the Oxygen Minimum Zone of the Tropical North Atlantic. *Journal of Physical Oceanography*, **40**, 1784–1801 (2010).

Brandt, P., F. Schott, C. Provost, A. Kartavtseff, V. Hormann, B. Bourles and J. Fischer: Circulation in the central equatorial Atlantic: Mean and intraseasonal to seasonal variability. *Geophysical Research Letters*, **33** (2006).

Bunge, L., C. Provost, B. L. Hua and A. Kartavtseff: Variability at intermediate depths at the equator in the Atlantic ocean in 2000-06: Annual cycle, equatorial deep jets, and intraseasonal meridional velocity fluctuations. *Journal of Physical Oceanography*, **38**, 1794–1806 (2008).

Carlson, J. (2002): Tech. rep., Development of an Optimized Dissolved Oxygen Sensor for Oceanographic Profiling. *International Ocean Systems, Volume 6, Number 5, September/October 2002*. Sea-Bird Electronics, Inc.

Clark, L., R. Wolf, D. Granger and Z. Taylor: Continuous Recording of Blood Oxygen Tensions by Polarography. *Journal of Applied Physiology*, **6**, 189–193 (1953).

De Szoeke, R. and A. Bennett: Microstructure Fluxes across Density Surfaces. *Journal of Physical Oceanography*, **23**, 2254–2264 (1993).

Defant, A. (1939): *Wissenschaftliche Ergebnisse der Deutschen Atlantischen Expedition auf dem Forschungs- und Vermessungsschiff 'Meteor' 1925-1927*. Verlag von Walter de Gruyter & Co.

Demas, J. N., B. A. DeGraff and P. B. Coleman: Oxygen sensors based on luminescence quenching. *Analytical Chemistry*, **71**, 793A–800A (1999).

Dickson, A. G. (1995): *Determination of Dissolved Oxygen in Seawater by Winkler Titration*. Tech. rep., WOCE Operations Manual. Part 3.1.3 Operations & Methods. WHP Office Report WHPO 91-1.

Eden, C.: Eddy length scales in the North Atlantic Ocean. *Journal of Geophysical Research - Oceans*, **112** (2007).

Eden, C. and R. J. Greatbatch: Towards a mesoscale eddy closure. *Ocean Modelling*, **20**, 223–239 (2008).

Eden, C. and R. J. Greatbatch: A diagnosis of isopycnal mixing by mesoscale eddies. *Ocean Modelling*, **27**, 98–106 (2009).

Eden, C., R. J. Greatbatch and D. Olbers: Interpreting eddy fluxes. *Journal of Physical Oceanography*, **37**, 1282–1296 (2007).

Eden, C., D. Olbers and R. J. Greatbatch: A generalized Osborn-Cox relation. *Journal of Fluid Mechanics*, **632**, 457–474 (2009).

Ferrari, R. and K. Polzin: Finescale structure of the T-S relation in the eastern North Atlantic. *Journal of Physical Oceanography*, **35**, 1437–1454 (2005).

Fiedler, B., P. Fietzek, N. Vieira, P. Silva, H. C. Bittig and A. Körtzinger: In Situ CO_2 and O_2 Measurements on a Profiling Float. *Journal of Atmospheric and Oceanic Technology*, **30**, 112–126 (2013).

Fischer, T., D. Banyte, P. Brandt, M. Dengler, G. Krahmann, T. Tanhua and M. Visbeck: Diapycnal oxygen supply to the tropical north atlantic oxygen minimum zone. *Biogeosciences Discussions*, **9**, 14291–14325 (2012).

Funk, A., P. Brandt and T. Fischer: Eddy diffusivities estimated from observations in the Labrador Sea. *Journal of Geophysical Research - Oceans*, **114** (2009).

Garcia, H. and L. Gordon: Oxygen solubility in seawater: Better fitting equations. *Limnology and Oceanography*, **37**, 1307–1312 (1992).

Garcia, H. E., R. A. Locarnini, T. P. Boyer, J. I. Antonov, O. K. Baranova, M. M. Zweng and D. R. Johnson (2010): *World Ocean Atlas 2009, Volume 3: Dissolved Oxygen, Apparent Oxygen Utilization, and Oxygen Saturation*. Tech. rep., S. Levitus, Ed. NOAA Atlas NESDIS 70, U.S. Government Printing Office, Washington, D.C., 344 pp.

Garrett, C. (2001): Stirring and mixing: What are the rate controlling processes? In *Proc. Aha Hulikoa Winter Workshop*, ed. by P. Müller and D. Henderson, University of Hawaii at Manoa.

Garzoli, S. and E. Katz: The Forced Annual Reversal of the Atlantic North Equatorial Countercurrent. *Journal of Physical Oceanography*, **13**, 2082–2090 (1983).

Garzoli, S. and P. Richardson: Low-Frequency Meandering of the Atlantic North Equatorial Countercurrent. *Journal of Geophysical Research - Oceans*, **94**, 2079–2090 (1989).

Gent, P. and J. McWilliams: Isopycnal Mixing in Ocean Circulation Models. *Journal of Physical Oceanography*, **20**, 150–155 (1990).

Gouretski, V. V. and K. P. Koltermann (2004): *WOCE Global Hydrographic Climatology*. Tech. Rep. 35, Bundesamt fr Seeschifffahrt und Hydrographie, Hamburg, Germany.

Grasshoff, K., K. Kremling and M. Ehrhardt (1999): *Methods of Seawater Analysis*. 3 edn., WILEY-VCH Verlag.

Hahn, J., P. Brandt, R. J. Greatbatch, G. Krahmann and A. Körtzinger (2013): Oxygen Variance and Meridional Oxygen Supply in the Tropical North East Atlantic Oxygen Minimum Zone. *submitted to Climate Dynamics*.

Hummels, R. M. (2012): *On the variability of turbulent mixing within the upper layers of the Atlantic Cold Tongue region*. Ph.D. thesis.

Jakobi, N., H. v. Neuhoff and B. Springer (2011): *25 Jahre FS Meteor*. Hauschild.

Kamenkovich, I., P. Berloff and J. Pedlosky: Anisotropic Material Transport by Eddies and Eddy-Driven Currents in a Model of the North Atlantic. *Journal of Physical Oceanography*, **39**, 3162–3175 (2009).

Karstensen, J., B. Fiedler, P. Brandt, R. Zantopp, J. Hahn, F. Schütte, A. Körtzinger, G. Fischer, M. Visbeck, O. Melicio and D. R. Wallace (2013): Dead-zone eddies in the tropical eastern north atlantic ocean. *under revision in Nature*.

Karstensen, J., L. Stramma and M. Visbeck: Oxygen minimum zones in the eastern tropical Atlantic and Pacific oceans. *Progress in Oceanography*, **77**, 331–350 (2008).

Keeling, R. F., A. Körtzinger and N. Gruber: Ocean Deoxygenation in a Warming World.

Annual Review of Marine Science, **2**, 199–229 (2010).

Kirchner, K., M. Rhein, S. Huettl-Kabus and C. W. Boening: On the spreading of South Atlantic Water into the Northern Hemisphere. *Journal of Geophysical Research - Oceans*, **114** (2009).

Körtzinger, A., J. Schimanski and U. Send: High quality oxygen measurements from profiling floats: A promising new technique. *Journal of Atmospheric and Oceanic Technology*, **22**, 302–308 (2005).

Lilly, J., P. Rhines, F. Schott, K. Lavender, J. Lazier, U. Send and E. D'Asaro: Observations of the Labrador Sea eddy field. *Progress in Oceanography*, **59**, 75–176 (2003).

Locarnini, R. A., A. V. Mishonov, J. I. Antonov, T. P. Boyer, H. E. Garcia, O. K. Baranova, M. M. Zweng and D. R. Johnson (2010): *World Ocean Atlas 2009, Volume 1: Temperature*. Tech. rep., S. Levitus, Ed. NOAA Atlas NESDIS 68, U.S. Government Printing Office, Washington, D.C., 184 pp.

Luyten, J., J. Pedlosky and H. Stommel: The Ventilated Thermocline. *Journal of Physical Oceanography*, **13**, 292–309 (1983).

Marshall, J. and G. Shutts: A Note on Rotational and Divergent Eddy Fluxes. *Journal of Physical Oceanography*, **11**, 1677–1680 (1981).

Matear, R. and A. Hirst: Long-term changes in dissolved oxygen concentrations in the ocean caused by protracted global warming. *Global Biogeochemical Cycles*, **17** (2003).

McDougall, T.: Neutral Surfaces. *Journal of Physical Oceanography*, **17**, 1950–1964 (1987).

Meissner, K., E. Galbraith and C. Volker: Denitrification under glacial and interglacial conditions: A physical approach. *Paleoceanography*, **20**, PA3001 (2005).

Miloshevich, L., A. Paukkunen, H. Vomel and S. Oltmans: Development and validation of a time-lag correction for Vaisala radiosonde humidity measurements. *Journal of Atmospheric and Oceanic Technology*, **21**, 1305–1327 (2004).

Müller, T. and G. Siedler: Multi-year current time series in the eastern North Atlantic Ocean. *Journal of Marine Research*, **50**, 63–98 (1992).

Osborn, T. R. and C. S. Cox: Oceanic fine structure. *Geophysical Fluid Dynamics*, **3**, 321–345 (1972).

Oschlies, A., K. G. Schulz, U. Riebesell and A. Schmittner: Simulated 21st century's increase in oceanic suboxia by CO_2 - enhanced biotic carbon export. *Global Biogeochemical Cycles*, **22** (2008).

Schott, F., M. Dengler, P. Brandt, K. Affler, J. Fischer, B. Bourles, Y. Gouriou, R. Molinari and M. Rhein: The zonal currents and transports at 35 degrees W in the tropical Atlantic. *Geophysical Research Letters*, **30** (2003).

Schott, F., J. Fischer and L. Stramma: Transports and pathways of the upper-layer circulation in the western tropical Atlantic. *Journal of Physical Oceanography*, **28**, 1904–1928 (1998).

Schott, F. A., J. P. McCreary Jr. and G. C. Johnson (2004): *Shallow Overturning Circulations of the Tropical-Subtropical Oceans*. Geophysical Monograph Series 147, American Geophysical Union, Washington, D. C.

Sinaasappel, M. and C. Ince: Calibration of Pd-porphyrin phosphorescence for oxygen concentration measurements in vivo. *Journal of Applied Physiology*, **81**, 2297–2303 (1996).

Smith, K. S. and R. Ferrari: The Production and Dissipation of Compensated Thermohaline Variance by Mesoscale Stirring. *Journal of Physical Oceanography*, **39**, 2477–2501 (2009).

Stramma, L., P. Brandt, J. Schafstall, F. Schott, J. Fischer and A. Körtzinger: Oxygen minimum zone in the North Atlantic south and east of the Cape Verde Islands. *Journal of Geophysical Research - Oceans*, **113**, C04014 (2008a).

Stramma, L., S. Huttl and J. Schafstall: Water masses and currents in the upper tropical northeast Atlantic off northwest Africa. *Journal of Geophysical Research - Oceans*, **110**, C12006 (2005).

Stramma, L., G. C. Johnson, J. Sprintall and V. Mohrholz: Expanding oxygen-minimum zones in the tropical oceans. *Science*, **320**, 655–658 (2008b).

Stramma, L., A. Oschlies and S. Schmidtko: Mismatch between observed and modeled trends in dissolved upper-ocean oxygen over the last 50 yr. *Biogeosciences*, **9**, 4045–4057 (2012).

Stramma, L. and F. Schott: The mean flow field of the tropical Atlantic Ocean. *Deep-Sea Research Part II - Topical Studies in Oceanography*, **46**, 279–303 (1999).

Stramma, L., M. Visbeck, P. Brandt, T. Tanhua and D. Wallace: Deoxygenation in the oxygen minimum zone of the eastern tropical North Atlantic. *Geophysical Research Letters*, **36** (2009).

Sverdrup, H. U.: On the explanation of the oxygen minima and maxima in the oceans. *J. Cons. int. Explor. Mer*, **13**, 163–172 (1938).

Tengberg, A., J. Hovdenes, H. Andersson, O. Brocandel, R. Diaz, D. Hebert, T. Arnerich, C. Huber, A. Körtzinger, A. Khripounoff, F. Rey, C. Ronning, J. Schimanski, S. Sommer and A. Stangelmayer: Evaluation of a lifetime-based optode to measure oxygen in aquatic systems. *Limnology and Oceanography - Methods*, **4**, 7–17 (2006).

Uchida, H., T. Kawano, I. Kaneko and M. Fukasawa: In Situ Calibration of Optode-Based Oxygen Sensors. *Journal of Atmospheric and Oceanic Technology*, **25**, 2271–2281 (2008).

Urbano, D., M. Jochum and I. da Silveira: Rediscovering the second core of the Atlantic NECC. *Ocean Modelling*, **12**, 1–15 (2006).

von Schuckmann, K., P. Brandt and C. Eden: Generation of tropical instability waves in the Atlantic Ocean. *Journal of Geophysical Research - Oceans*, **113** (2008).

Wattenberg, H. (1939): *Wissenschaftliche Ergebnisse der Deutschen Atlantischen Expedition auf dem Forschungs- und Vermessungsschiff 'Meteor' 1925-1927 - Band IX: Die Verteilung des Sauerstoffs im Atlantischen Ozean*. Verlag von Walter de Gruyter & Co.

Winkler, L. W.: Determination of in water dissolved oxygen (in german language). *Berichte der deutschen chemischen Gesellschaft*, **21**, 2843–2854 (1888).

Wunsch, C.: Where do ocean eddy heat fluxes matter? *Journal of Geophysical Research - Oceans*, **104**, 13235–13249 (1999).

Wüst, G.: Die tiefenzirkulation im raume des atlantischen ozeans. *Naturwissenschaften*, **24**, 133–141 (1936).

Wyrtki, K.: The oxygen minima in relation to ocean circulation. *Deep-Sea Research*, **9**, 11–23 (1962).

Zhang, D., M. McPhaden and W. Johns: Observational evidence for flow between the subtropical and tropical Atlantic: The Atlantic subtropical cells. *Journal of Physical Oceanography*, **33**, 1783–1797 (2003).

List of Figures

List of Tables

Acknowledgments

I would like to thank Prof. Dr. Peter Brandt for his dedicated and continuous supervision, for all the helpful discussions and for his patience during all phases of this work. His comprehensive expertise was a basis for the realization of this work.

I would like to thank Prof. Dr. Richard J. Greatbatch for the discussions and his comprehensive expertise in Theoretical Oceanography that helped to illuminate and consider new aspects in this study.

I thank Prof. Dr. Arne Körtzinger and Henry Bittig for their support and their expertise, particularly in optode oxygen sensors. Henry Bittig substantially contributed to the development of the in situ calibration procedure of optodes.

Drs. Marcus Dengler, Tim Fischer, Johannes Karstensen and Gerd Krahmann supported me with helpful discussions. Their analytic comprehension helped to improve this work.

I thank Dr. Gerd Krahmann for the sophisticated processing of shipboard CTD/O_2 data, Sven-Helge Didwischus for processing velocity data from shipboard ADCPs as well as Dr. Andreas Funk and Rainer Zantopp for partly processing the mooring data.

Special thanks go to all technicians of the GEOMAR research department Physical Oceanography. They conducted the mooring work and supervised the sensor systems with high expertise. In particular, I would like to thank Andreas Pinck for the development and maintenance of the optode oxygen loggers which performed with high reliability.

This work was supported by the German Science Foundation as part of the collaborative research centre *SFB754 "Climate-Biogeochemistry Interactions in the Tropical Ocean"*.

Optode oxygen loggers were partly deployed in the framework of the *PIRATA* project.

I would like to thank Tobias Hahn, Dr. Rebecca Hummels, Henry Bittig and Rainer Zantopp for their dedicated proofreading of this work.

Special thanks go to B11 - here I feel homelike.

Ein großer Dank gilt auch meiner Familie: meinen Eltern Michael und Christina Hahn, ohne deren Unterstützung ich nie so weit gekommen wäre; meinem Bruder Tobias Hahn für seine Unterstützung und vor allem dafür, dass er ein Stück weit Heimat mit nach Kiel gebracht hat; meiner Schwester Elisabeth Hahn für ihre mentale Unterstützung und ihr Verständnis für die letzten Monate. Insbesondere sende ich *S*chöne *G*rüße nach Halle/Saale.

Ich möchte einen besonderen Dank an Maria Fischer aussprechen. Sie hat stets zu mir gehalten, sehr viel Verständnis aufgebracht und mich in jeder (Lebens-) Lage unterstützt.

Affirmation / Eidesstattliche Erklärung

Hiermit erkläre ich an Eides statt, dass ich die vorliegende Arbeit unter Einhaltung der Regeln guter wissenschaftlicher Praxis der *Deutschen Forschungsgemeinschaft* selbständig erarbeitet und verfasst und keine anderen als die angegebenen Quellen und Hilfsmittel verwendet habe.

Ich versichere, dass diese Arbeit in der vorgelegten oder einer ähnlichen Fassung noch nicht an anderer Stelle zur Erlangung des Doktorgrades eingereicht worden ist.

Kiel, April 2013

(Johannes Hahn)